COMPRESSIBLE FLOWS OF DENSE GASES IN BOUNDARY LAYERS

by

Sarah Turner Whitlock

Thesis submitted to the Faculty of the

Virginia Polytechnic Institute and State University

in partial fulfillment of the requirements for the degree of

Master of Science

in

Engineering Mechanics

APPROVED:

Mark S. Cramer, Chairman

Dean T. Mook

Saad A. Ragab

August 1992

Blacksburg, Virginia

COMPRESSIBLE FLOWS OF DENSE GASES IN BOUNDARY LAYERS

by

Sarah Turner Whitlock

Mark S. Cramer, Chairman

Engineering Mechanics

(ABSTRACT)

The equations and numerics necessary for the analysis of dense-gas boundary-layer flows over arbitrarily shaped two-dimensional bodies are developed. The governing equations are derived from the Navier-Stokes-Fourier equations for a general fluid. A numerical method based on the second-order Davis-coupled scheme is employed to solve for mean flows over flat plates. Flows of nitrogen, sulfur hexafluoride, and toluene over adiabatic walls are examined; in addition, flows of nitrogen over heated and cooled walls are studied. Results indicate a breakdown of the standard correlations for the recovery factor and the Nusselt number due primarily to the substantial variations of the Prandtl number and the Chapman-Rubesin parameter throughout the boundary layer. The stability equations for two-dimensional inviscid disturbances in a general fluid are derived. The temporal stability of the mean flows of nitrogen is subsequently examined using the generalized inflection-point criterion extracted from these equations. Results reveal significant variations from standard ideal-gas predictions including the existence of flows for which neither heating nor cooling of the wall has a stabilizing effect.

Acknowledgements

Throughout the course of this endeavor, I have relied on a number of people without whose help I am doubtful this project would have reached fruition. I wish to express my gratitude to Dr. Mark S. Cramer for sharing his knowledge of a wide array of subjects, not all pertaining to fluid mechanics, in his capacity as my advisor. I am grateful to Dr. Dean T. Mook and Dr. Saad A. Ragab for their willingness to serve on my committee. The computing facilities and the guidance on the use of SUPORE provided by Dr. Layne T. Watson are also much appreciated. Finally, many thanks to my two best friends, Melissa and Marc, for their love and support without which both my life and this project would be incomplete.

This research was supported by the National Science Foundation under Grant No. CTS-8913198.

Table of Contents

List of Illustrations

List of Tables

Chapter 1

Introduction

In 1904 Prandtl showed that high-Reynolds-number flows over solid bodies may be divided into two regions: the boundary layer, a very thin layer close to the body where frictional effects are important, and the inviscid outer flow, the region outside this layer where frictional effects are negligible. Since then the significance and behavior of the boundary layer has been studied in considerable detail. It is recognized that the boundary layer serves as the transition region between the inviscid outer flow and the zero-velocity flow at the surface of the body. From a more practical point of view, the boundary layer is recognized as the source of skin friction, heat transfer, turbulence, and separation in general fluid flows.

Due to their widespread practical significance, boundary-layer flows of gases have been studied extensively over the past ninety years. Typically, these studies are restricted to low-pressure, or ideal, gases in which an ideal-gas equation of state is adequate for describing the variation of pressure with density and temperature. Furthermore, it is commonly assumed that the viscosity, thermal conductivity, specific heat, and hence the Prandtl number are functions of temperature alone. Frequently, however, the Prandtl number and the specific heat are taken to be constant.

Typical examples of viscosity and thermal-conductivity models are the well-known Sutherland and power-law models; see for example White (1974).

In contrast to the previously mentioned research on low-pressure gases, the present study encompasses boundary-layer flows throughout the entire single-phase vapor region for several fluids. The investigation of such flows has potential applications in several areas. For example, the experiments conducted in heavy-gas wind tunnels employ various fluids with thermodynamic properties different from air in order to achieve the high-Reynolds-number flows occurring in aerodynamic applications. At present, it is unclear whether the benefit of an increased Reynolds number will be offset by the error caused by the discrepancy between the thermodynamic properties for the test fluid and those for air. A second example involves Rankine power-cycle systems, which frequently operate in the dense-gas region. The influence of the thermodynamic properties of the fluid in this region can have a significant impact on design and efficiency considerations for these systems. Because the effects of variable thermodynamic characteristics and the attributes of dense-gas flows are not thoroughly understood, it is hoped that this work will be a useful contribution to boundary-layer literature.

The models employed in the low-pressure-limit analysis of boundary-layer flows are not necessarily valid in the entire single-phase vapor region. The breakdown of these models is most dramatic in the neighborhood of the thermodynamic critical point, which is that thermodynamic state at which a saturated vapor and a saturated liquid can coexist; the values of pressure, specific volume, and temperature at this point are consequently termed critical values. An example of this breakdown appears in Figure 1.1, which contains a comparison of the ideal-gas model to the accepted data for nitrogen adapted from Van Wylen and Sonntag (1985). An examination of the figure reveals that the ideal-gas model is least accurate in the general vicinity of the thermodynamic critical point.

Like the equation of state, the low-pressure models for viscosity and thermal conductivity are also not necessarily adequate throughout the single-phase vapor region. As an example, the variations of these transport properties with temperature and pressure are shown in Figures 1.2 and 1.3. In these figures, the reduced values of viscosity and thermal conductivity for an arbitrary fluid

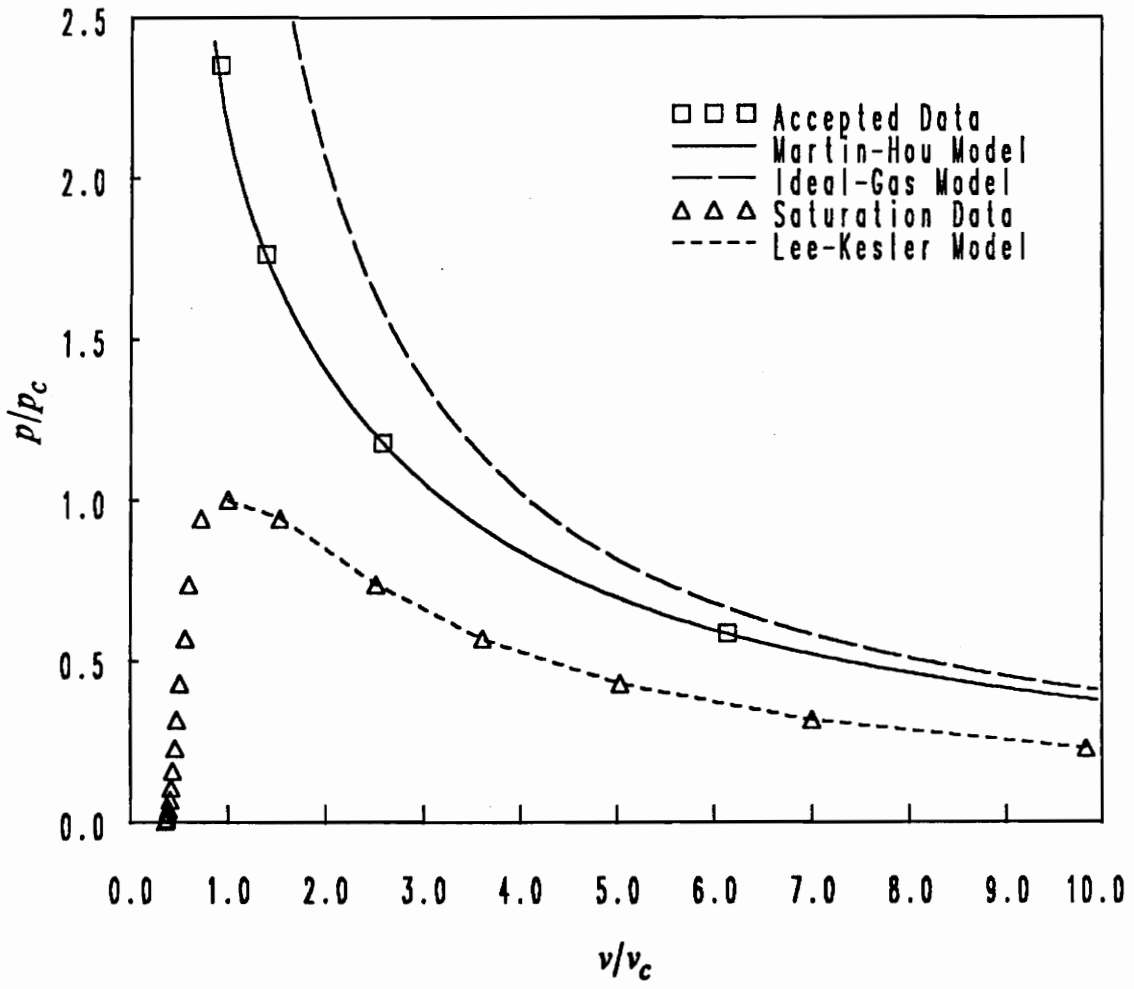

Figure 1.1. Comparison of fluid models to actual nitrogen data: The ideal-gas and Martin-Hou equations of state are compared to nitrogen data for pressures and volumes throughout the single-phase vapor region at a temperature of approximately 1.2^*T_c. The Lee-Kesler approximation to the saturation curve is plotted with actual saturation data.

are illustrated. The term *reduced* refers to values which have been scaled to the corresponding critical values. Because the dependence on pressure, and thus on density, is nontrivial, the temperature-dependent models used in the low-pressure limit are clearly inaccurate over most of the single-phase vapor region. In addition, the Prandtl number and the specific heat are also dependent on density as well as temperature, meaning that the low-pressure models for these quantities may also be inaccurate.

As noted by Sengers et al. (1970) and Hall (1971), it is well known that the specific heat and thermal conductivity physically tend to infinity as the thermodynamic critical point is approached. Such singularities, frequently referred to as critical-point singularities or anomalies, are important only in a small region in the immediate neighborhood of the thermodynamic critical point. For the most part, the pressures and temperatures encountered in the present study will be sufficiently far from the critical values. For this reason and in order to simplify the analysis in this first look at dense-gas boundary layers, the critical-point singularities will be ignored here.

Three specific fluids are investigated in this research effort: nitrogen, sulfur hexafluoride, and toluene. Nitrogen is selected because of its well-established physical properties and its application as a test gas in cryogenic wind tunnels. Sulfur hexafluoride is chosen due to the recent interest in its application as a test gas for heavy-gas wind tunnels as discussed by Anderson (1990, 1991a,b). Toluene has been used frequently as a Rankine-cycle working fluid as noted by Miller (1974), Curran (1981), and Manco and Nervegna (1985). Furthermore, the three fluids were chosen to illustrate the effect of increasing specific heat on boundary-layer flows: from nitrogen (smallest specific heat) through toluene (largest specific heat).

Throughout this analysis, only steady, two-dimensional, compressible, laminar, boundary-layer flows of single-phase, Navier-Stokes-Fourier gases in thermodynamic equilibrium are considered. In each case, the temperature is taken to be 1.01 times the critical temperature. To illustrate the effects of increasing pressure, and hence density, on the boundary layer, three values of the reduced specific volume are used throughout. The first state is defined by a reduced specific volume chosen to produce a pressure of one atmosphere and is thus called the *one-atmosphere* case. The second state corresponds to a reduced specific volume of 2.0 and is called

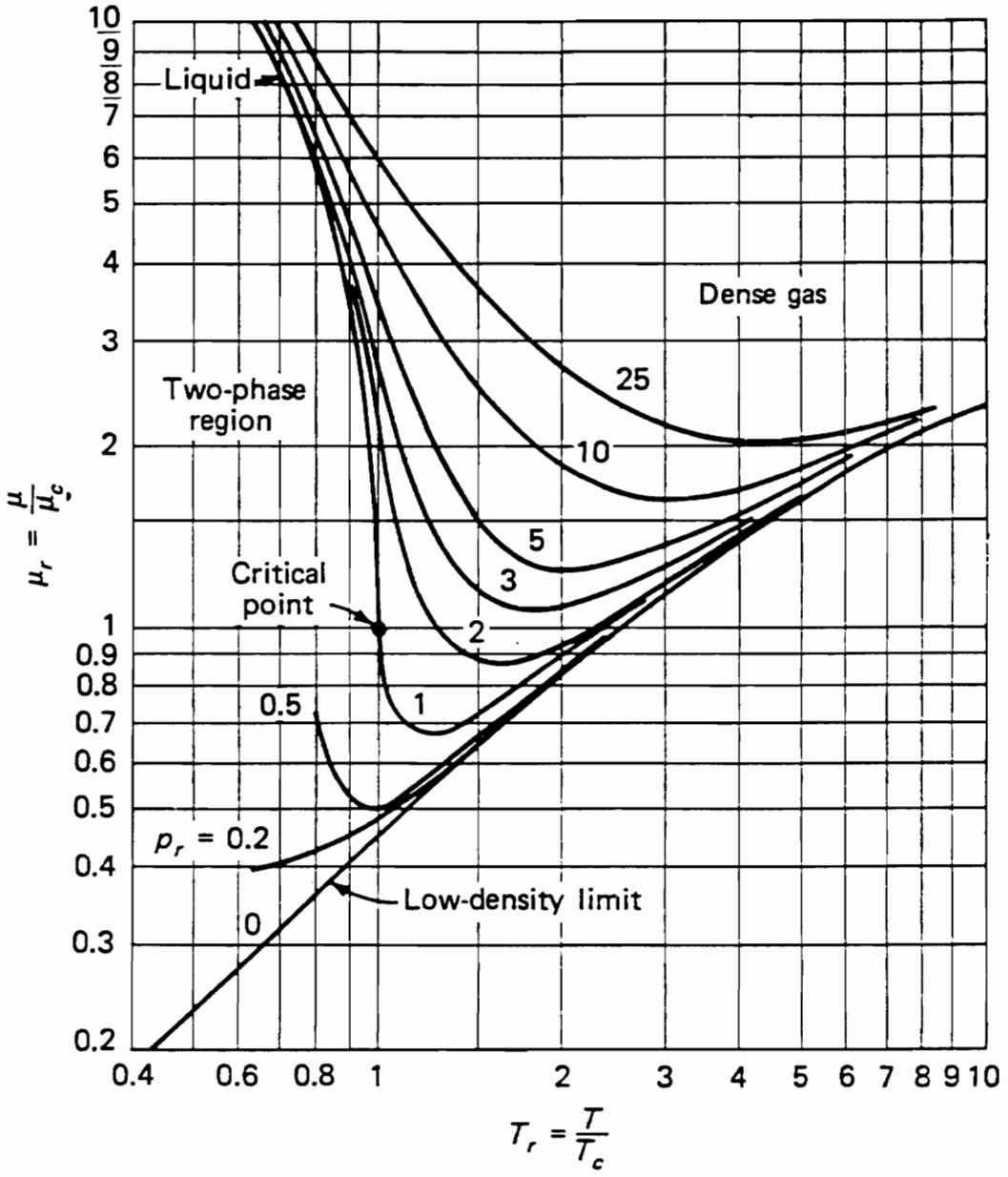

Figure 1.2. Plot of reduced viscosity vs. reduced temperature for several values of the reduced pressure: The data shown is reprinted from White (1974) using data adapted from Uyehara and Watson (1944).

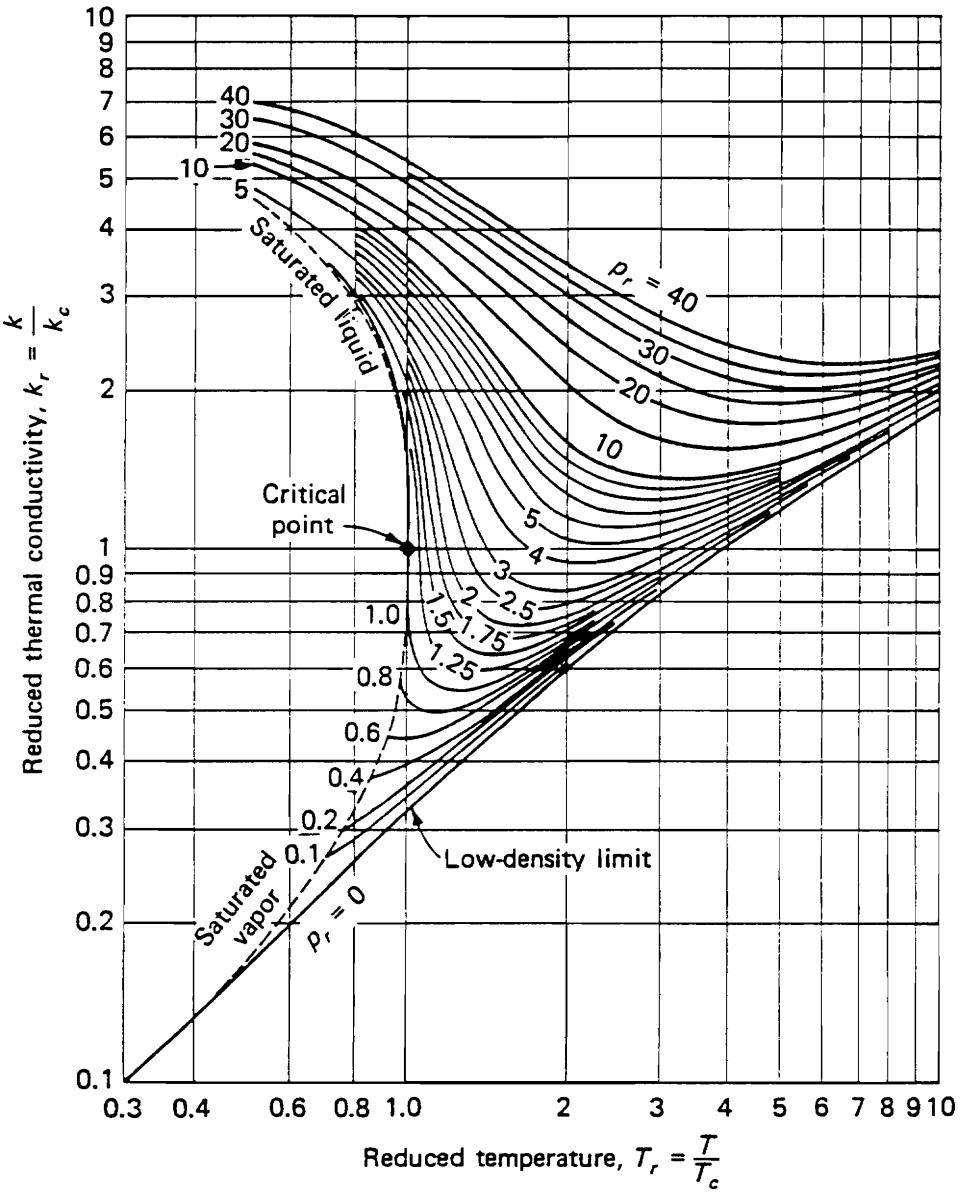

Figure 1.3. **Plot of reduced thermal conductivity vs. reduced temperature for several values of the reduced pressure:** The data shown is reprinted from White (1974) using data adapted from Owens and Thodos (1957).

the *dense-gas* case. The third state is defined by a volume equal to 0.8 times the critical volume and is consequently termed the *near-critical* case. The modifier *dense-gas* is used here to describe a particular thermodynamic state; in other contexts it denotes all single-phase vapors exclusive of those in the low-pressure region. For each fluid and each state, the mean flow is determined numerically and the inviscid stability is investigated using a temporal analysis.

The following chapters are devoted to the development of pertinent theory and presentation of results. Chapter 2 consists of a derivation of the boundary-layer equations for the flows of general fluids over arbitrarily shaped two-dimensional bodies. In Chapter 3, the specific gas models are described in detail. The equations developed in Chapters 2 and 3 are then solved numerically for flow over a flat plate using the numerical scheme outlined in Chapter 4. The solutions for the mean flows are presented in Chapters 5 and 6; the former contains adiabatic-wall results while the latter focuses on heated- and cooled-wall flows. The theoretical development for the stability of the mean flows appears in Chapter 7 with the corresponding results presented in Chapter 8. A brief analysis of the results and suggestions for related research conclude the study in Chapter 9.

Chapter 2

Mean-Flow Formulation

Introduction

As discussed in the introduction, the fluids to be investigated are single-phase, Navier-Stokes fluids in a state of thermodynamic equilibrium. The new features of this analysis are the thermodynamic conditions under which these ordinary fluids are to be studied. Specifically, the fluids are subject to freestream pressure and temperature conditions spanning the entire single-phase vapor region. The governing equations appropriate for this study are, nevertheless, virtually identical to the familiar perfect-gas expressions.

Boundary-Layer Equations for a General Fluid

The starting point for analyzing boundary layers is the Navier-Stokes-Fourier equations for unsteady, two-dimensional, compressible, laminar flow. After neglecting body forces, the equations can be shown to be

$$\frac{\partial \bar{\rho}}{\partial \bar{t}} + \frac{\partial(\bar{\rho}\bar{u})}{\partial \bar{x}} + \frac{\partial(\bar{\rho}\bar{v})}{\partial \bar{y}} = 0, \tag{2.1}$$

$$\bar{\rho}\left(\frac{\partial \bar{u}}{\partial \bar{t}} + \bar{u}\frac{\partial \bar{u}}{\partial \bar{x}} + \bar{v}\frac{\partial \bar{u}}{\partial \bar{y}} \right) = -\frac{\partial \bar{p}}{\partial \bar{x}} + \frac{\partial}{\partial \bar{x}}\left[\bar{\lambda}\left(\frac{\partial \bar{u}}{\partial \bar{x}} + \frac{\partial \bar{v}}{\partial \bar{y}} \right) + 2\bar{\mu}\frac{\partial \bar{u}}{\partial \bar{x}} \right] + \frac{\partial}{\partial \bar{y}}\left[\bar{\mu}\left(\frac{\partial \bar{u}}{\partial \bar{y}} + \frac{\partial \bar{v}}{\partial \bar{x}} \right) \right],$$

(2.2)

$$\bar{\rho}\left(\frac{\partial \bar{v}}{\partial \bar{t}} + \bar{u}\frac{\partial \bar{v}}{\partial \bar{x}} + \bar{v}\frac{\partial \bar{v}}{\partial \bar{y}} \right) = -\frac{\partial \bar{p}}{\partial \bar{y}} + \frac{\partial}{\partial \bar{x}}\left[\bar{\mu}\left(\frac{\partial \bar{u}}{\partial \bar{y}} + \frac{\partial \bar{v}}{\partial \bar{x}} \right) \right] + \frac{\partial}{\partial \bar{y}}\left[\bar{\lambda}\left(\frac{\partial \bar{u}}{\partial \bar{x}} + \frac{\partial \bar{v}}{\partial \bar{y}} \right) + 2\bar{\mu}\frac{\partial \bar{v}}{\partial \bar{y}} \right],$$

(2.3)

$$\bar{\rho}\bar{c}_p\left(\frac{\partial \bar{T}}{\partial \bar{t}} + \bar{u}\frac{\partial \bar{T}}{\partial \bar{x}} + \bar{v}\frac{\partial \bar{T}}{\partial \bar{y}} \right) = \bar{\beta}\bar{T}\left(\frac{\partial \bar{p}}{\partial \bar{t}} + \bar{u}\frac{\partial \bar{p}}{\partial \bar{x}} + \bar{v}\frac{\partial \bar{p}}{\partial \bar{y}} \right)$$

$$+ 2\bar{\mu}\left[\left(\frac{\partial \bar{u}}{\partial \bar{x}} \right)^2 + \left(\frac{\partial \bar{v}}{\partial \bar{y}} \right)^2 + \frac{1}{2}\left(\frac{\partial \bar{u}}{\partial \bar{y}} + \frac{\partial \bar{v}}{\partial \bar{x}} \right)^2 \right]$$

$$+ \bar{\lambda}\left(\frac{\partial \bar{u}}{\partial \bar{x}} + \frac{\partial \bar{v}}{\partial \bar{y}} \right)^2 + \frac{\partial}{\partial \bar{x}}\left(\bar{k}\frac{\partial \bar{T}}{\partial \bar{x}} \right) + \frac{\partial}{\partial \bar{y}}\left(\bar{k}\frac{\partial \bar{T}}{\partial \bar{y}} \right), \tag{2.4}$$

where the coefficient of thermal expansion, $\overline{\beta}$, is defined by

$$\overline{\beta} \equiv -\frac{1}{\overline{\rho}}\left(\frac{\partial \overline{\rho}}{\partial \overline{T}}\right)_{\overline{p}}. \tag{2.5}$$

In the above equations, the symbols $\overline{x}$ and $\overline{y}$ are coordinates parallel and normal to the wall, respectively, with $\overline{u}$ and $\overline{\mathrm{v}}$ the corresponding velocity components. The density is represented by $\overline{\rho}$, the pressure by $\overline{p}$, the temperature by $\overline{T}$, and the time by $\overline{t}$. Finally, $\overline{\mu} = \overline{\mu}(\overline{\rho}, \overline{T})$ is the coefficient of shear viscosity, $\overline{\lambda} = \overline{\lambda}(\overline{\rho}, \overline{T})$ is the second coefficient of viscosity, $\overline{c}_p = \overline{c}_p(\overline{\rho}, \overline{T})$ is the coefficient of specific heat at constant pressure, and $\overline{k} = \overline{k}(\overline{\rho}, \overline{T})$ is the coefficient of thermal conductivity. In all cases, an overbar designates a dimensional quantity. Equations (2.1) - (2.4) are recognized as the expressions for the conservation of mass, momentum, and energy governing the four field variables $\overline{u}$, $\overline{\mathrm{v}}$, $\overline{\rho}$, and $\overline{T}$.

The first-order, dimensional, boundary-layer equations for steady flow may be shown to be

$$\frac{\partial(\overline{\rho}\overline{u})}{\partial \overline{x}} + \frac{\partial(\overline{\rho}\overline{\mathrm{v}})}{\partial \overline{y}} = 0, \tag{2.6}$$

$$\overline{\rho}\left(\overline{u}\frac{\partial \overline{u}}{\partial \overline{x}} + \overline{\mathrm{v}}\frac{\partial \overline{u}}{\partial \overline{y}}\right) = -\frac{\partial \overline{p}}{\partial \overline{x}} + \frac{\partial}{\partial \overline{y}}\left(\overline{\mu}\frac{\partial \overline{u}}{\partial \overline{y}}\right), \tag{2.7}$$

$$\overline{\rho}\overline{c}_p\left(\overline{u}\frac{\partial \overline{T}}{\partial \overline{x}} + \overline{\mathrm{v}}\frac{\partial \overline{T}}{\partial \overline{y}}\right) = \overline{\beta}\overline{T}\overline{u}\frac{\partial \overline{p}}{\partial \overline{x}} + \overline{\mu}\left(\frac{\partial \overline{u}}{\partial \overline{y}}\right)^2 + \frac{\partial}{\partial \overline{y}}\left(\overline{k}\frac{\partial \overline{T}}{\partial \overline{y}}\right). \tag{2.8}$$

The boundary-layer approximation to Equation (2.3) requires

$$\frac{\partial \bar{p}}{\partial \bar{y}} \simeq 0. \tag{2.9}$$

As a result, the pressure is taken to be constant across the boundary layer. Hence, the pressure may be regarded as a function of $\bar{x}$ alone, meaning that the partial derivatives of $\bar{p}$ in Equations (2.7) - (2.8) may be replaced by total derivatives. Equations (2.6) - (2.8) are recognized as the expressions for the conservation of mass, momentum, and energy.

A change of variables is introduced in order to account for the growth of the boundary layer with $\bar{x}$. As a result, it is possible to minimize the number of points needed to resolve the flow throughout the thickness of the boundary layer. The new variables are based on the Levy-Lees transforms (1956) and are defined as

$$\xi(\bar{x}) = K\int_0^{\bar{x}} \bar{\rho}_e \bar{\mu}_e \bar{u}_e d\bar{x}' \tag{2.10}$$

and

$$\eta(\bar{x}, \bar{y}) = \bar{u}_e\sqrt{\frac{K}{2\xi}}\int_0^{\bar{y}} \bar{\rho}\, d\bar{y}' \tag{2.11}$$

where the scaling constant K has been chosen to be

$$K = \left(\bar{\rho}_\infty \bar{\mu}_\infty \bar{u}_\infty \bar{L}\right)^{-1}. \tag{2.12}$$

The subscripts e and ∞ denote conditions at the outer edge of the boundary layer and in the undisturbed freestream, respectively, and $\bar{L}$ denotes any convenient length scale characteristic of the length of the body.

With the substitution of the definitions of ξ and η into Equations (2.6) - (2.8), it can be shown that the boundary-layer equations become

$$2\xi \frac{\partial F}{\partial \xi} + \frac{\partial V}{\partial \eta} + F = 0, \tag{2.13}$$

$$2\xi F \frac{\partial F}{\partial \xi} + V \frac{\partial F}{\partial \eta} + \beta_p \left(F^2 - \frac{\rho_e}{\rho} \right) - \frac{\partial}{\partial \eta} \left(\ell \frac{\partial F}{\partial \eta} \right) = 0, \tag{2.14}$$

$$2\xi F \frac{\partial \theta}{\partial \xi} + V \frac{\partial \theta}{\partial \eta} - \alpha \ell \frac{c_{pe}}{c_p} \left(\frac{\partial F}{\partial \eta} \right)^2 - \frac{1}{c_p} \frac{\partial}{\partial \eta} \left(\frac{c_p \ell}{Pr} \frac{\partial \theta}{\partial \eta} \right) + \mathscr{R} = 0. \tag{2.15}$$

In the above expressions, the non-dimensional velocity and temperature parameters are

$$F = \frac{u}{u_e}, \quad V = \frac{2\xi}{\rho_e \mu_e u_e} \left(\rho_\infty \mu_\infty F \frac{\partial \eta}{\partial x} + \sqrt{\frac{Re_\infty}{2\xi}} \rho v \mu_\infty \right), \quad \theta = \frac{T}{T_e} \tag{2.16}$$

where

$$x = \frac{\bar{x}}{\bar{L}}. \tag{2.17}$$

Throughout, all densities, pressures, and temperatures are scaled relative to their thermodynamic critical-point values:

$$\rho = \frac{\bar{\rho}}{\bar{\rho}_c}, \quad p = \frac{\bar{p}}{\bar{p}_c}, \quad T = \frac{\bar{T}}{\bar{T}_c} \tag{2.18}$$

where the subscript c denotes the thermodynamic critical-point value. All velocity components are scaled relative to the freestream:

$$u = \frac{\bar{u}}{\bar{u}_\infty}, \quad \mathrm{v} = \frac{\bar{\mathrm{v}}}{\bar{u}_\infty}. \tag{2.19}$$

The freestream Mach number, sound speed, and Reynolds number are respectively defined as

$$M_\infty = \frac{\bar{u}_\infty}{\bar{a}_\infty}, \quad a_\infty = \frac{\bar{a}_\infty}{\sqrt{\bar{R}\bar{T}_c}}, \quad Re_\infty = \frac{\bar{\rho}_\infty \bar{u}_\infty \bar{L}}{\bar{\mu}_\infty}. \tag{2.20}$$

The shear viscosity, thermal conductivity, and specific heat at constant pressure are normalized as follows:

$$\mu = \frac{\bar{\mu}}{\bar{\mu}_o}, \quad k = \frac{\bar{k}}{\bar{k}_o}, \quad c_p = \frac{\bar{c}_p}{\bar{c}_{vo}} \tag{2.21}$$

where $\bar{\mu}_o$, $\bar{k}_o$, and $\bar{c}_{vo}$ are the expressions for the low-pressure versions of the shear viscosity, thermal conductivity, and coefficient of specific heat at constant volume. These low-pressure quantities are evaluated at a reference temperature equal to the thermodynamic critical temperature and at a reference pressure of one atmosphere. The pressure gradient parameter, β_p, is defined as

$$\beta_p = -\frac{2\xi}{\rho_e u_e^2}\frac{dp}{d\xi}\frac{\bar{p}_c}{\bar{\rho}_c \bar{u}_\infty^2} \tag{2.22}$$

and may be reduced to the form

$$\beta_p = \frac{2\xi}{u_e}\frac{du_e}{d\xi} \tag{2.23}$$

with the aid of the Bernoulli equation applied to the isentropic, inviscid outer flow and the fact that the pressure is constant across the boundary layer. The Chapman-Rubesin parameter, the Prandtl number, and the Eckert number are defined as

$$\ell = \frac{\rho\mu}{\rho_e\mu_e}, \quad Pr = \frac{\bar{\mu}\bar{c}_p}{\bar{k}}, \quad \alpha = \frac{u_e^2}{c_{pe}T_e}, \tag{2.24}$$

and the non-dimensional coefficient of thermal expansion, β, is

$$\beta = -\frac{1}{\rho}\left(\frac{\partial\rho}{\partial T}\right)_p. \tag{2.25}$$

The term $\mathscr{R}$ seen in Equation (2.15) is defined as

$$\mathscr{R} = \tilde{\alpha}\alpha\beta_p T_e\beta_e\left(\frac{\beta}{\beta_e}\frac{c_{pe}\rho_e}{c_p\rho} - 1\right)\theta F, \tag{2.26}$$

where

$$\tilde{\alpha} = M_\infty^2 a_\infty^2 \delta_T, \quad \delta_T = \frac{\bar{R}}{\bar{c}_{vo}}. \tag{2.27}$$

The origin of $\mathscr{R}$ is the pressure-gradient term in Equation (2.8).

The expression for the non-dimensional skin friction, defined by

$$c_f = \frac{\bar{\mu}_w \left. \frac{\partial \bar{u}}{\partial \bar{y}} \right|_w}{\bar{\rho}_\infty \bar{u}_\infty^2}, \tag{2.28}$$

may be written in terms of Levy-Lees variables as

$$c_f = \left(\frac{\rho_w \mu_w}{\rho_\infty \mu_\infty} \right) \frac{u_e^2}{\sqrt{2Re_\xi}} \left. \frac{\partial F}{\partial \eta} \right|_w, \tag{2.29}$$

where the Reynolds number based on freestream properties and the scaled distance ξ is defined as

$$Re_\xi = \frac{\bar{\rho}_\infty \bar{u}_\infty \xi \bar{L}}{\bar{\mu}_\infty} \tag{2.30}$$

and the subscript w denotes evaluation at the wall. The recovery factor for adiabatic walls, given by

$$r = \frac{(\bar{T}_w - \bar{T}_\infty)}{\frac{1}{2} \frac{\bar{u}_\infty^2}{\bar{c}_{p\infty}}}, \tag{2.31}$$

transforms to

$$r = \frac{(T_w - T_\infty)}{\frac{1}{2} \frac{M_\infty^2 a_\infty^2}{c_{p\infty}} \delta_T} \tag{2.32}$$

in Levy-Lees coordinates. Finally, the Nusselt number, defined by

$$N_x = \frac{-\bar{k}_w \left.\frac{\partial \bar{T}}{\partial \bar{y}}\right|_w \bar{x}}{\bar{k}_\infty (\bar{T}_w - \bar{T}_{adb})} \tag{2.33}$$

where $\bar{T}_{adb}$ is the adiabatic-wall temperature, can be written in Levy-Lees coordinates as

$$N_x = \frac{-k_w \left.\frac{\partial \theta}{\partial \eta}\right|_w \left(\frac{\bar{x}}{\xi \bar{L}}\right)}{k_\infty (T_w - T_{adb})} \frac{\rho_w T_e u_e}{\rho_\infty} \sqrt{\frac{Re_\xi}{2}}. \tag{2.34}$$

The well-known perfect-gas versions of Equations (2.13) - (2.15) are recovered by noting that

$$\bar{p} \to \bar{\rho} \bar{R} \bar{T}, \quad \bar{\rho} \to 0, \quad \bar{\beta} \bar{T} \to 1, \quad \bar{c}_v \to constant \text{ , and } \bar{c}_p \to constant = \bar{R} + \bar{c}_v \tag{2.35}$$

in the perfect-gas limit. Here, $\bar{c}_v$ is the coefficient of specific heat at constant volume. As a result,

$$\mathscr{R} \to 0, \quad \bar{c}_p \to \bar{c}_{pe}, \quad \text{and} \quad \frac{\bar{\rho}_e}{\bar{\rho}} \to \theta \tag{2.36}$$

and Equations (2.13) - (2.15) can be reduced to

$$2\xi \frac{\partial F}{\partial \xi} + \frac{\partial V}{\partial \eta} + F = 0, \tag{2.37}$$

$$2\xi F \frac{\partial F}{\partial \xi} + V \frac{\partial F}{\partial \eta} + \beta_p (F^2 - \theta) - \frac{\partial}{\partial \eta} \left(\ell \frac{\partial F}{\partial \eta} \right) = 0, \tag{2.38}$$

$$2\xi F \frac{\partial \theta}{\partial \xi} + V \frac{\partial \theta}{\partial \eta} - \alpha \ell \left(\frac{\partial F}{\partial \eta} \right)^2 - \frac{\partial}{\partial \eta} \left(\frac{\ell}{Pr} \frac{\partial \theta}{\partial \eta} \right) = 0. \tag{2.39}$$

When the Prandtl number is constrained to be constant, Equations (2.37) - (2.39) are in complete agreement with those recorded by Fletcher (1988).

Boundary Conditions

The boundary-layer formulation is complete once the boundary conditions are specified. At the wall, the standard no-penetration and no-slip conditions are imposed. Mathematically, these conditions take the form

$$F = V = 0 \quad \text{on} \quad \eta = 0. \tag{2.40}$$

At the outer edge of the boundary layer, the asymptotic matching conditions are met by requiring that

$$F, \theta \rightarrow 1 \quad \text{as} \quad \eta \rightarrow \infty. \tag{2.41}$$

The remaining condition to be imposed is the thermal condition at the wall. Depending upon the physical thermal state at the wall, one of two thermal boundary conditions may be specified. The first is the wall-temperature condition:

$$\theta_w = \frac{T_w(\xi)}{T_e(\xi)} \quad \text{on} \quad \eta = 0 \tag{2.42}$$

where $T_w(\xi)$ is a specified wall-temperature variation. For the case of an isothermal wall, $T_w(\xi)$ is a constant. The second type of thermal boundary condition is the heat-flux condition:

$$\frac{\partial \theta}{\partial \eta} = -\dot{Q}_w(\xi) \quad \text{on} \quad \eta = 0 \tag{2.43}$$

where $\dot{Q}_w(\xi)$ is a scaled heat flux along the wall. The scaled heat flux is related to the dimensional heat flux through:

$$\dot{Q}_w = \bar{\dot{Q}}_w \frac{k_\infty \rho_\infty T_\infty}{k_w \rho_w T_e u_e} \sqrt{\frac{2}{Re_\xi}} \frac{\xi \bar{L}}{\bar{k}_\infty \bar{T}_\infty} \tag{2.44}$$

where

$$\bar{\dot{Q}}_w = -\bar{k}_w \left. \frac{\partial \bar{T}}{\partial \bar{y}} \right|_w \tag{2.45}$$

is the dimensional heat flux. In the case of an adiabatic wall, the heat flux is identically zero.

The transformed boundary-layer equations coupled with the specified boundary conditions comprise a well-posed system of nonlinear differential equations once the equation of state, ideal-gas specific-heat, shear-viscosity, and thermal-conductivity models are specified. The models employed in the computations are described in the next chapter.

Chapter 3

Gas Models

Introduction

The final pieces of information needed to solve the boundary-layer equations are the set of constitutive relationships for the fluid material properties: pressure, viscosity, thermal conductivity, and ideal-gas specific heat. The relationships employed here model the functional dependence of the variables on density and temperature throughout the entire pure-vapor phase space. The models described are also known to give reasonable approximations for both polar and non-polar gases. The standard thermodynamic identities for the sound speed, the specific heat at constant pressure, the specific heat at constant volume, and the coefficient of thermal expansion are also included.

Equation of State

The real-gas equation of state chosen for the present analysis is that due to Martin and Hou (1955). The equation takes the form

$$\bar{p} = \frac{\bar{R}\bar{T}}{\bar{v} - \bar{b}} + \sum_{i=1}^{4} \frac{\bar{A}_i + \bar{B}_i\bar{T} + \bar{C}_i e^{-5.475(\bar{T}/\bar{T}_c)}}{(\bar{v} - \bar{b})^i} \tag{3.1}$$

where $\bar{A}_i$, $\bar{B}_i$, $\bar{C}_i$, and $\bar{b}$ are constants which depend on the fluid to be modeled and $\bar{v}$ is the gas specific volume. One of the advantages of the Martin-Hou equation of state is that it requires a minimum of physical data in order to determine the constants $\bar{A}_i$, $\bar{B}_i$, $\bar{C}_i$, and $\bar{b}$. In particular, these constants can be computed from the formulas given by Martin and Hou once the molecular weight, $\bar{p}_c$, $\bar{T}_c$, $\bar{v}_c$, and $\bar{T}_b$ (boiling temperature) of the fluid of interest are specified. The equation is accurate over a wide range of pressures and temperatures, including those corresponding to perfect gases. Furthermore, it is valid for polar as well as non-polar substances. The primary limitation on Equation (3.1), given by Martin and Hou, is an upper density limit of 1.5 times the fluid critical density.

A comparison of the ideal-gas model and the Martin-Hou model to accepted data for nitrogen as adapted from Van Wylen and Sonntag (1985) is provided in Figure 1.1 for a reduced temperature of approximately 1.2. A comparison of the ideal-gas prediction to the accepted data reveals the inaccuracy of the ideal-gas model for densities near the critical value. In contrast, the agreement between the Martin-Hou equation and the accepted data is excellent over the full range of densities and pressures shown.

Viscosity and Thermal Conductivity

State-of-the-art models for shear viscosity and thermal conductivity as functions of density and temperature have been developed by Chung et al. (1984, 1988). These models are reasonably accurate for polar and non-polar substances throughout the single-phase vapor region. As with the Martin-Hou equation of state, the models may be used once $\overline{p}_c$, $\overline{T}_c$, $\overline{v}_c$, and $\overline{T}_b$ of the fluid under consideration are specified. In the case of a non-polar substance, the acentric factor, which can be computed either from $\overline{T}_b$ and $\overline{T}_c$ or from tabulated vapor-pressure data, is also required. A complete description of the model formulation can be found in the original articles by Chung et al. An evaluation of the accuracy of these models relative to other methods appears in Reid et al. (1987).

Ideal-Gas Specific Heat

The ideal-gas specific heat is approximated by the power-law formula

$$\overline{c}_{vo}(\overline{T}) = \overline{c}_{vo}(\overline{T}_{ref})\left(\frac{\overline{T}}{\overline{T}_{ref}}\right)^n \tag{3.2}$$

where n is a fluid-dependent parameter. The values of n and $\overline{c}_{vo}(\overline{T}_{ref})$ were computed from the data of Reid et al. (1987). The main advantage of Equation (3.2) over more accurate polynomial expressions is its simplicity and its relative accuracy over temperature ranges which are moderate compared to the variation of the specific heat itself.

Physical Properties

Relevant properties of nitrogen, sulfur hexafluoride, and toluene obtained from Reid et al. (1987) are provided in Table 3.1.

Thermodynamic Identities

Standard thermodynamic relations are now employed to yield values for the sound speed, the coefficient of specific heat at constant pressure, the coefficient of specific heat at constant volume, and the coefficient of thermal expansion. The thermodynamic sound speed is defined as

$$\bar{a} = \left(\left. \frac{\partial \bar{p}}{\partial \bar{\rho}} \right|_{\bar{s}} \right)^{1/2} \tag{3.3}$$

where

$$\left. \frac{\partial \bar{p}}{\partial \bar{\rho}} \right|_{\bar{s}} = \gamma \left. \frac{\partial \bar{p}}{\partial \bar{\rho}} \right|_{\bar{T}} \tag{3.4}$$

and $\bar{s}$ is the entropy. The ratio of specific heats, γ, is

$$\gamma = \frac{\bar{c}_p}{\bar{c}_v} \tag{3.5}$$

Table 3.1. Properties for various fluids adapted from Reid et al.(1987).

	Nitrogen	Sulfur Hexafluoride	Toluene
Molecular Weight	28.01	146.05	92.14
$\bar{p}_c$ (atm)	33.9	37.6	41.0
$\overline{T}_c$ (K)	126.2	318.7	591.8
$\bar{v}_c$ (cm^3/mole)	89.8	198.8	316.0
$\overline{T}_b$ (K)	77.4	209.6	383.8
Acentric Factor	0.04	0.29	0.26
$\bar{c}_{v\infty}(\overline{T}_c)/\overline{R}$	2.59	11.25	22.12
n	0.00	0.66	0.78

where the coefficient of specific heat at constant pressure is computed from

$$\bar{c}_p = \bar{c}_v + \frac{\bar{\beta}\bar{T}}{\bar{\rho}} \left.\frac{\partial \bar{p}}{\partial \bar{T}}\right|_{\bar{\rho}}, \tag{3.6}$$

and the coefficient of specific heat at constant volume can be computed from the ideal-gas specific heat and the equation of state according to the formula:

$$\bar{c}_v = \bar{c}_{vo} - \bar{T}\int_0^{\bar{\rho}} \left.\frac{\partial^2 \bar{p}}{\partial \bar{T}^2}\right|_{\bar{\rho}} \frac{d\bar{\rho}}{\bar{\rho}^2}. \tag{3.7}$$

The coefficient of thermal expansion, $\bar{\beta}$, defined in Equation (2.5), can be related to partial derivatives of the pressure through the use of standard thermodynamic identities and Equation (3.4) as follows:

$$\bar{\beta} = -\frac{1}{\bar{\rho}}\left[-\frac{\left.\frac{\partial \bar{p}}{\partial \bar{T}}\right|_{\bar{\rho}}}{\left.\frac{\partial \bar{p}}{\partial \bar{\rho}}\right|_{\bar{T}}}\right] = \frac{\gamma}{\bar{\rho}\bar{a}^2} \left.\frac{\partial \bar{p}}{\partial \bar{T}}\right|_{\bar{\rho}}. \tag{3.8}$$

The system of nonlinear boundary-layer equations, with the addition of boundary conditions and constitutive relations, is now solvable. The numerical procedure utilized to solve the system is presented in the next chapter.

Chapter 4

Numerical Scheme

Because in the most general case no analytic solution exists for the nonlinear system of boundary-layer equations, it is necessary to generate a solution numerically. The first step in any such endeavor is the discretization of the physical domain into a computational space known as a grid. The governing equations are then written in discrete form and solved at specified points in the flow known as grid points. The details of the discretization procedure are omitted here because the concepts of finite-difference methodology are well documented for perfect-gas boundary-layer flows. Only minor modifications of existing finite-difference schemes applied to perfect-gas flows are needed for the application to the more general case considered here. The interested reader is referred to the work by Blottner (1974), who carefully outlines the second-order Davis-coupled version of the Crank-Nicolson scheme on which the present analysis is based.

Once the boundary-layer equations are written in discrete form, an iterative procedure is invoked to solve the equations. Iterations are performed at fixed ξ-locations beginning with the first. At a fixed ξ-location, initial guesses for all the flow variables are specified. These guesses are termed *old* values and are used to solve the mass and momentum equations, uncoupled from the energy equation, to yield new values of F and V. The resulting values of F and V, along with the

remaining old variables, are used to solve the energy equation for θ. The revised value for θ is then used to calculate a new density consistent with the constant boundary-layer pressure. Once the updated values of ρ and θ are known, new values for μ, k, c_p, and β are computed through the use of the appropriate thermodynamic formulas. This procedure is then repeated, with the new variables used in place of the previous old quantities, until the flow variables meet a specified convergence criterion.

When the solution is converged at a particular ξ-location, the entire procedure is repeated at the next ξ-location. The values of the flow variables from the converged ξ-location are used as the initial guesses in the next iteration sequence. The iteration procedure is performed at each successive ξ-location until the end of the body is reached.

The algorithm used to implement the iteration scheme is outlined below:

1. Set initial profiles for all variables -- first ξ-location

2. Update F and V by solving mass and momentum equations

3. Update θ by solving energy equation using F and V from Step 2

4. Update ρ using θ from Step 3

5. Update μ, k, c_p, and β using θ and ρ from Steps 3 and 4

6. Go to Step 2 unless solution is converged

7. Proceed to next ξ-location using converged solution from Steps 2, 3, 4, and 5 as initial guess on variables

8. Go to Step 2 unless end of body is reached

9. Stop

The initial guess for F at the first ξ-location is as follows:

$$F = 0 \quad \text{on} \quad \eta = 0 \tag{4.1}$$

and

$$F = 1 \quad \text{for} \quad 0 < \eta \leq \eta_{\max} \tag{4.2}$$

where $\eta_{\max}$ is the value of η at the edge of the boundary layer. The initial profile for V is

$$V = -\eta \quad \text{for} \quad 0 \leq \eta \leq \eta_{\max}. \tag{4.3}$$

The initial distribution for θ depends on the thermal condition specified at the wall. If the temperature condition of Equation (2.42) is used, the condition

$$\theta = \frac{T_w(\xi)}{T_e(\xi)} \quad \text{on} \quad \eta = 0 \tag{4.4}$$

is employed and the remaining θ profile is taken to be linearly increasing or decreasing from $T_w(\xi)/T_e(\xi)$ to unity at $\eta = \eta_{\max}$. For an adiabatic wall, the initial wall temperature, $T_w(\xi)$, is approximated by the perfect-gas recovery factor:

$$r = b(Pr_e), \tag{4.5}$$

where it is shown by Eckert and Drewitz (1940), Emmons and Brainerd (1941, 1942), and Meksyn (1960) that

$$b(Pr_e) = \begin{cases} \sqrt{Pr_e} & \text{for} \quad Pr_e \simeq 1 \\ 1.9 Pr_e^{1/3} & \text{for} \quad Pr_e \to \infty \end{cases} \tag{4.6}$$

and Pr_e is the outer-edge Prandtl number. Then the adiabatic wall temperature distribution is taken to be

$$\theta = \frac{T_w(\xi)}{T_e(\xi)} \quad \text{for} \quad 0 \le \eta \le 0.10(\eta_{max}), \tag{4.7}$$

$$\theta = 1 \quad \text{for} \quad 0.90\eta_{max} \le \eta \le \eta_{max}, \tag{4.8}$$

and a linearly decreasing function from $\eta = 0.10(\eta_{max})$ to $\eta = 0.90(\eta_{max})$. The initial distribution for ρ is determined from the appropriate equation of state once the initial temperature profile is known. Initial profiles for μ, k, c_p, and β are computed with the use of initial ρ and θ values in the relevant equations in Chapter 3.

The only substantive difference between the procedure employed in the perfect-gas theory and that used here is the treatment of Step 4. In the case of a perfect gas, the density may be determined explicitly from the equation of state once the temperature is computed in Step 3. In contrast, the Martin-Hou equation of state used in the present calculations is so complicated that an implicit solution for the density is required. Thus, a density value is found by iterating on the equation of state at the temperature provided from Step 3 and at a pressure equal to the outer-edge pressure. The Newton-Raphson root-finding technique is used to accomplish this goal. The old density distribution is used as the initial guess required by the Newton-Raphson iterator.

The criterion specified for the convergence of the flow variables at a fixed ξ-location involves an inspection of the evolution of the temperature solution. At each iteration, the magnitude of the differences in value between the new and old θ at every η-location is recorded. When the maximum difference between values of the old and new θ is less than a specified value, which is typically on

the order of 10^{-12}, the temperature solution is considered converged. Because all of the material properties which influence the development of the boundary-layer flow are functions of temperature and density, and the density is directly dependent on the temperature through the equation of state, all of the flow variables are considered converged once the temperature solution is converged.

After a converged solution is obtained, all points in the flowfield are checked to see if any part of the flow is inside the two-phase region. The Lee-Kesler formula (1975) for the saturated-vapor line is used in this check. If it is found that any part of the computed flow lies within the two-phase region, the solution is deemed inappropriate and discarded. As can be seen from Figure 1.1, which shows the Lee-Kesler approximation to the saturation line relative to actual experimental data, the formula used is a conservative estimate of the location of the saturation line. The general accuracy of the Lee-Kesler saturation formula has been compared to others in Reid et al. (1987).

All mean-flow calculations were performed using an IBM 3090 mainframe computer. The cases run correspond to the flow of various fluids over a flat plate in the range of freestream Mach numbers from 0.01 to 3.0. For these cases, a uniform grid consisting of 201 points in the η-direction is used. A grid of 11 points in the ξ-direction is used to confirm that the computed flow is self-similar as would be expected for a flat-plate flow.

Chapter 5

Mean-Flow Results: Adiabatic Walls

Introduction

Results for the boundary-layer flows of nitrogen, sulfur hexafluoride, and toluene are presented in this chapter. Only flows over flat plates with an adiabatic wall condition are considered. For this geometry, the outer-edge conditions are identical to the freestream conditions, and there is no variation of fluid parameters in the ξ-direction, meaning that the flow is self-similar.

The first set of adiabatic-wall results presented corresponds to the flow of nitrogen over a flat plate. The effects of freestream density on boundary-layer flows will be demonstrated first by considering the changes in the local-flow variables due to density effects and then by illustrating the impact of these changes on the global parameters. In the context of this discussion, the local-flow variables are taken to be F, V, θ, ρ, μ, k, c_p, and Pr and the global parameters are taken to be ρ_w/ρ_e, ℓ_w, c_f, Pr_w/Pr_e, and r. A freestream Mach number of 2.0 is arbitrarily chosen for the display of the distributions of the local-flow variables through the thickness of the boundary layer. The results corresponding to this Mach number are expected to be roughly representative of the

behavior of the full range of Mach numbers. Otherwise, no special significance is attached to this specific freestream Mach number.

Each of the adiabatic-wall plots shown will consist of four curves: three curves which represent the results of calculations with the dense-gas constitutive relations from Chapter 3 for the freestream thermodynamic states described in Chapter 1 and one curve which represents the results of calculations with ideal-gas relations -- the volume chosen for the latter is identical to that used for the one-atmosphere case. The ideal-gas case is provided merely to demonstrate that the Martin-Hou equation of state and the dense-gas constitutive relations of Chapter 3 recover the ideal-gas solution in the low-pressure limit. Each of the figures shown demonstrates the effects of density on the respective boundary-layer flows. The results generated with ideal-gas formulas will be referred to as *ideal-gas* cases. The real-gas calculations of the freestream reduced volumes of 0.8 and 2.0 will be designated *near-critical* and *dense-gas* cases, respectively. Finally, the real-gas results for freestream flows at one atmosphere will be called *one-atmosphere* cases.

The second set of adiabatic-wall results shown will be a comparison of the flows of nitrogen, sulfur hexafluoride, and toluene over a flat plate. Profiles of the local-flow variables through the thickness of the boundary layer at a freestream Mach number of 2.0 will be presented along with the variations of the global parameters with Mach number. As with the display of adiabatic-wall results for nitrogen, the flows at a freestream Mach number of 2.0 are expected to be typical of the behavior of the boundary-layer flows in question. All of the figures will consist of three curves, each representing a different fluid, at a specific freestream volume. Results for freestream volumes corresponding to the one-atmosphere, dense-gas, and near-critical cases will be presented. Each of the plots shown illustrates the effect of increasing specific heat on boundary-layer flows.

Nitrogen: Local-Flow Variables

The effects of freestream density on the velocity distributions in a boundary-layer flow are depicted in Figures 5.1 and 5.2. The near-critical and dense-gas momentum boundary layers appear to be thinner than the one-atmosphere case, with the near-critical flow being the thinnest. The near-critical and dense-gas horizontal velocity profiles are also more full than their one-atmosphere counterparts and, as a result, exhibit larger horizontal velocity gradients at the wall. These fuller profiles appear to suggest a correspondingly higher skin friction at the wall for the near-critical and dense-gas flows relative to the one-atmosphere case. Results to be presented subsequently, however, contradict the higher skin-friction prediction. This contradiction is, in part, due to the fact that the larger horizontal velocity gradients observed in the $F-\eta$ plane do not necessarily translate into larger velocity gradients in the $\bar{u}-\bar{y}$ plane.

An added peculiarity of the near-critical flow is the existence of a rapid change in the slope of the velocity profiles at an η-location of approximately 0.7. This η-location corresponds to the place where the boundary-layer flow conditions are closest to the thermodynamic critical point. The rapid variations of physical properties characteristic of the near-critical region is expected to be the cause of the rapid change in slope of the near-critical velocity profiles. Numerical studies which increase the maximum η-location and the number of points in the η-direction have been performed, confirming that the rapid changes of slope in the near-critical velocity profiles are of physical rather than numerical origin. Behavior similar to that shown here has also been observed by Simoneau and Williams (1969) in an examination of laminar Couette flow at conditions in the vicinity of the thermodynamic critical point.

The variation of θ with η, depicted in Figure 5.3, indicates the effect of changes in the freestream density on the thermal boundary layer. While the flows corresponding to each of the three freestream thermodynamic states behave in the same qualitative manner, the near-critical flow exhibits the smallest temperature increase. Furthermore, the region of heating in the near-critical boundary layer appears to be restricted to an area of the flow in the immediate vicinity of the wall.

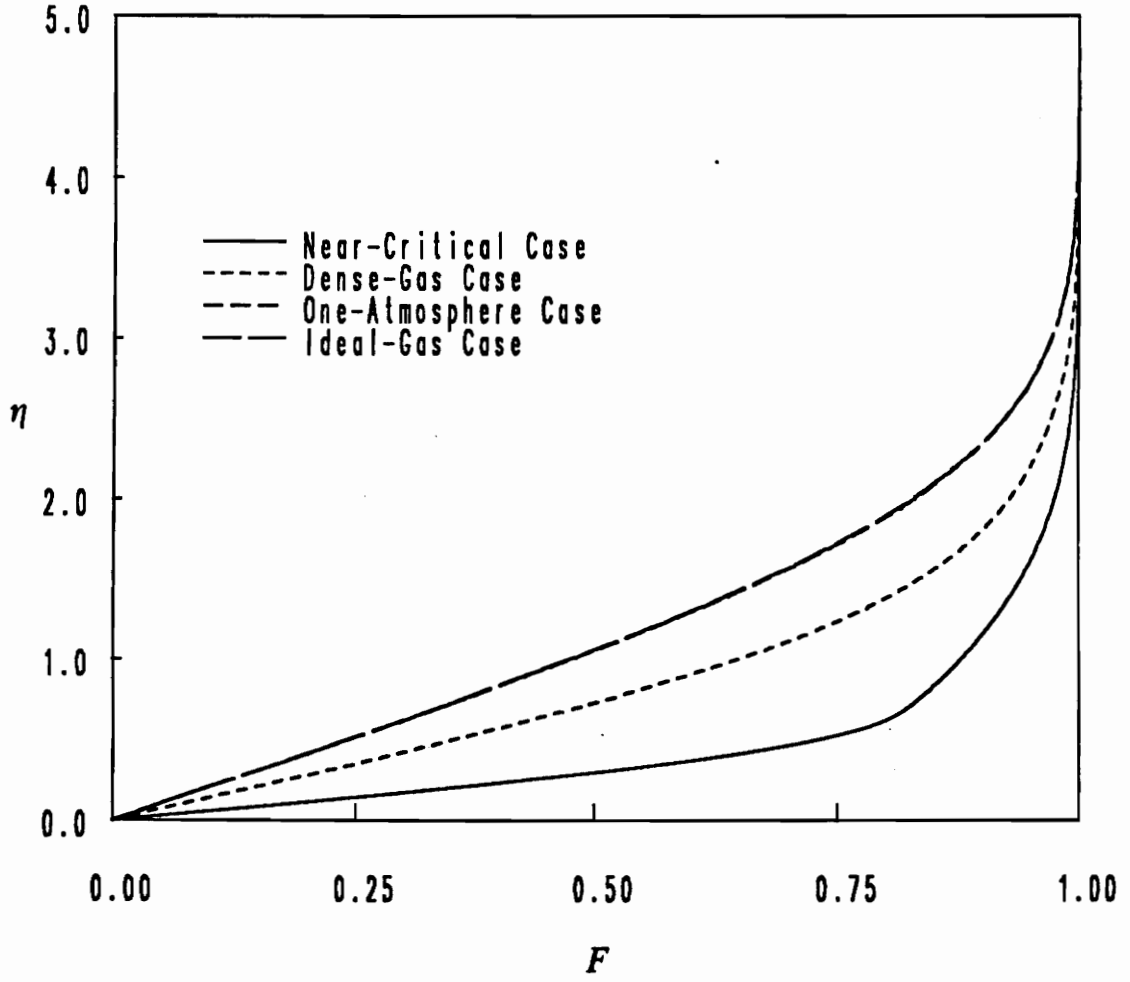

Figure 5.1. **Plot of F vs. η for nitrogen at various freestream densities:** Illustrated are the results for a freestream Mach number of 2.0 and a freestream temperature of $1.01*T_c$. The one-atmosphere case corresponds to a freestream volume of $115*v_c$.

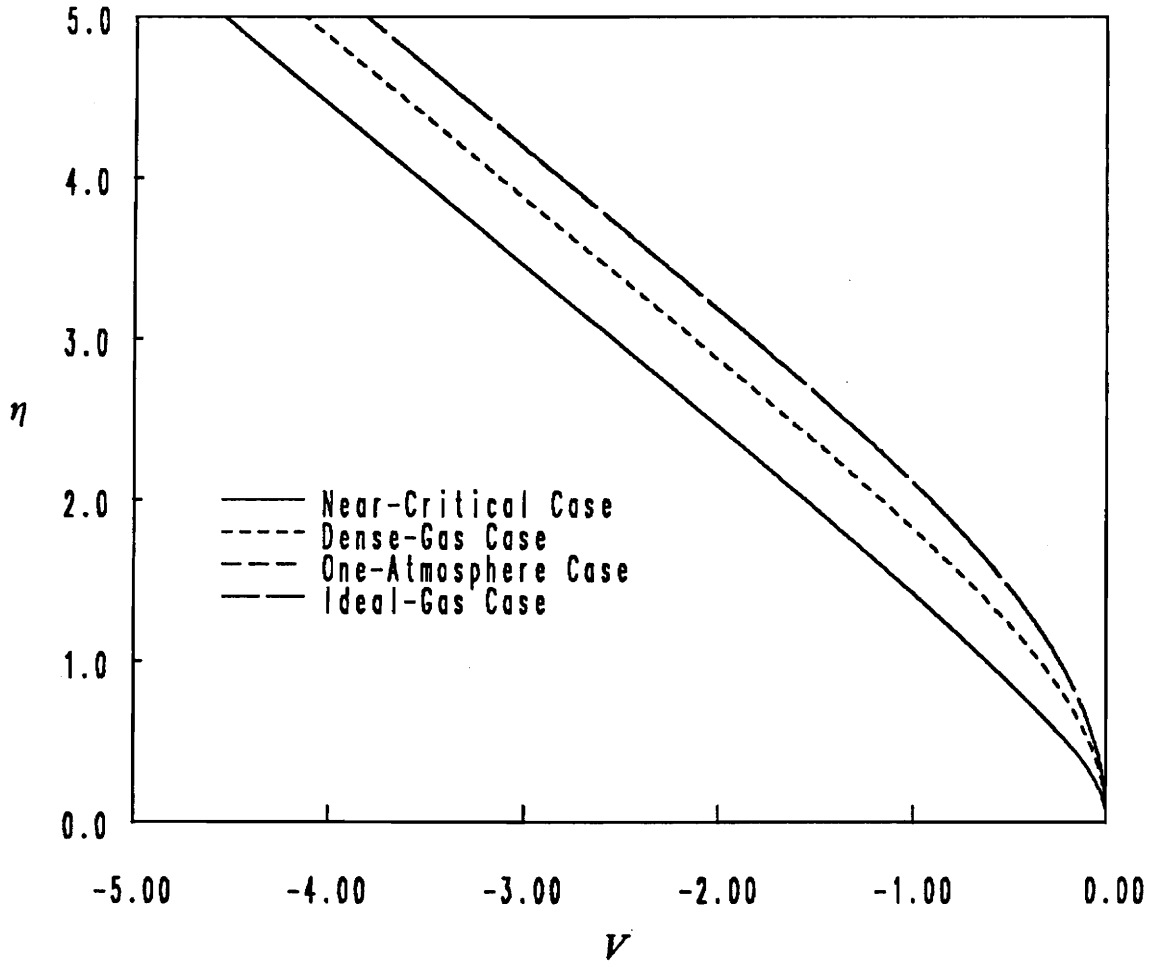

Figure 5.2. Plot of V vs. η for nitrogen at various freestream densities: Illustrated are the results for a freestream Mach number of 2.0 and a freestream temperature of $1.01*T_c$. The one-atmosphere case corresponds to a freestream volume of $115*v_c$.

The result is a near-critical thermal layer which is one-third the size of the dense-gas layer, which is itself roughly half the size of the one-atmosphere layer.

The explanation for the decrease in the wall temperature for flows with freestream densities approaching the thermodynamic critical point is found by an inspection of the specific heat. As the freestream conditions approach the critical point, the value of the specific heat increases dramatically. Consequently, the influence of the viscous-dissipation term in the energy equation,

$$\alpha \ell \frac{c_{pe}}{c_p} \left(\frac{\partial F}{\partial \eta} \right)^2 = \frac{u_e^2}{c_p T_e} \ell \left(\frac{\partial F}{\partial \eta} \right)^2, \tag{5.1}$$

decreases relative to the other terms in the equation. The result is a decrease in the wall temperature which leads to a trend toward isothermal flow as the freestream conditions approach the critical point.

The variation of the specific heat through the boundary layer for the various freestream thermodynamic states is illustrated in Figure 5.4. The one-atmosphere specific heat remains virtually constant throughout the boundary layer as expected. The dense-gas and near-critical specific-heat distributions, however, deviate substantially from their respective freestream values.

The freestream value of c_p for the dense-gas case is approximately 4.5 times the value of the one-atmosphere case. Thus, although the dense-gas specific heat decreases to roughly 25% of its freestream value at the wall, the overall value of c_p through the thickness of the dense-gas boundary layer is larger than the one-atmosphere specific heat. As mentioned above, the result is a decrease in the viscous dissipation and hence a decrease in the amount of temperature increase in the dense-gas flow relative to the one-atmosphere flow.

The freestream value of c_p for the near-critical case is approximately 20 times the value of the one-atmosphere case. Furthermore, the near-critical specific heat doubles its freestream value at an η-location of approximately 0.7 as the flow conditions approach the thermodynamic critical point. As a result, the average value of the specific heat is considerably larger than that of the one-atmosphere case, which, as discussed above, translates into a dramatic decrease in the influence

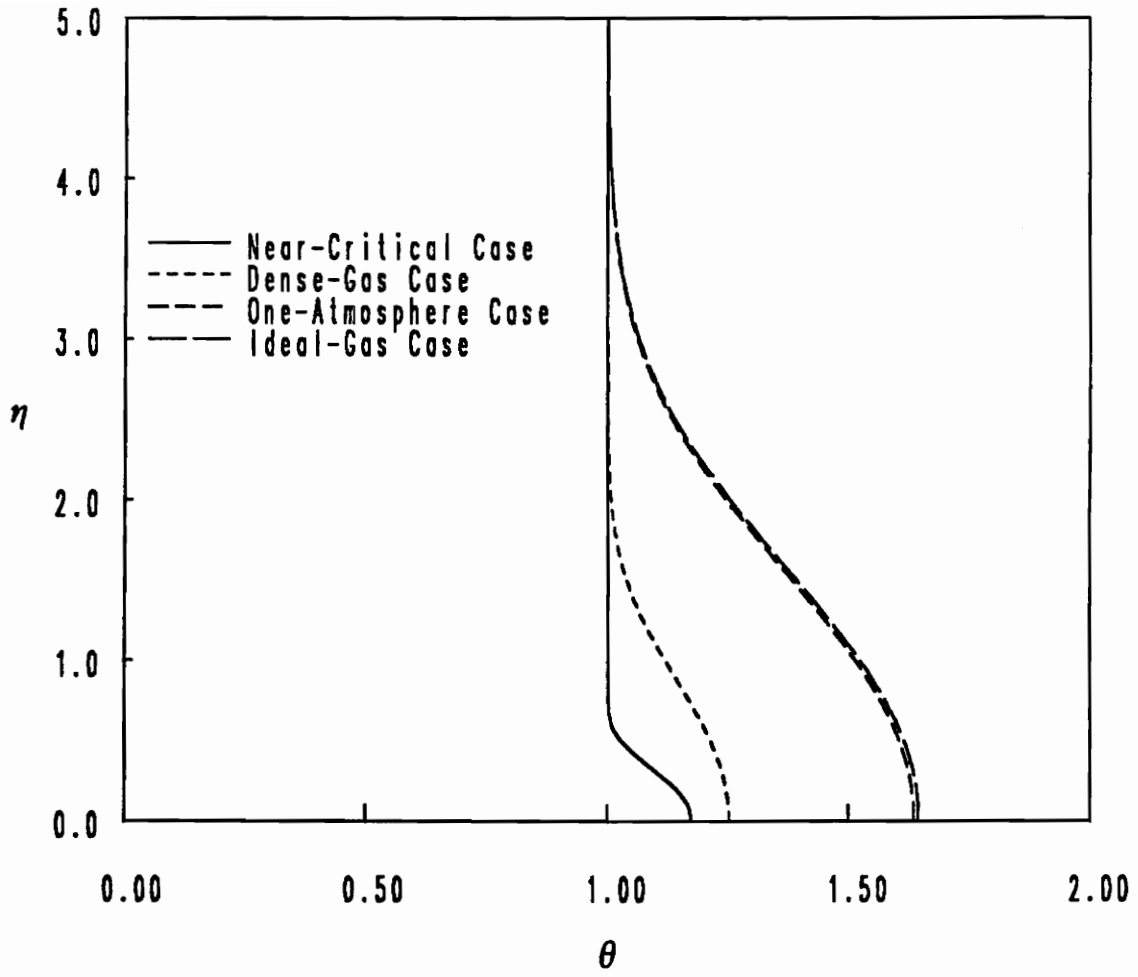

Figure 5.3. Plot of θ vs. η for nitrogen at various freestream densities: Illustrated are the results for a freestream Mach number of 2.0 and a freestream temperature of $1.01*T_c$. The one-atmosphere case corresponds to a freestream volume of $115*v_c$.

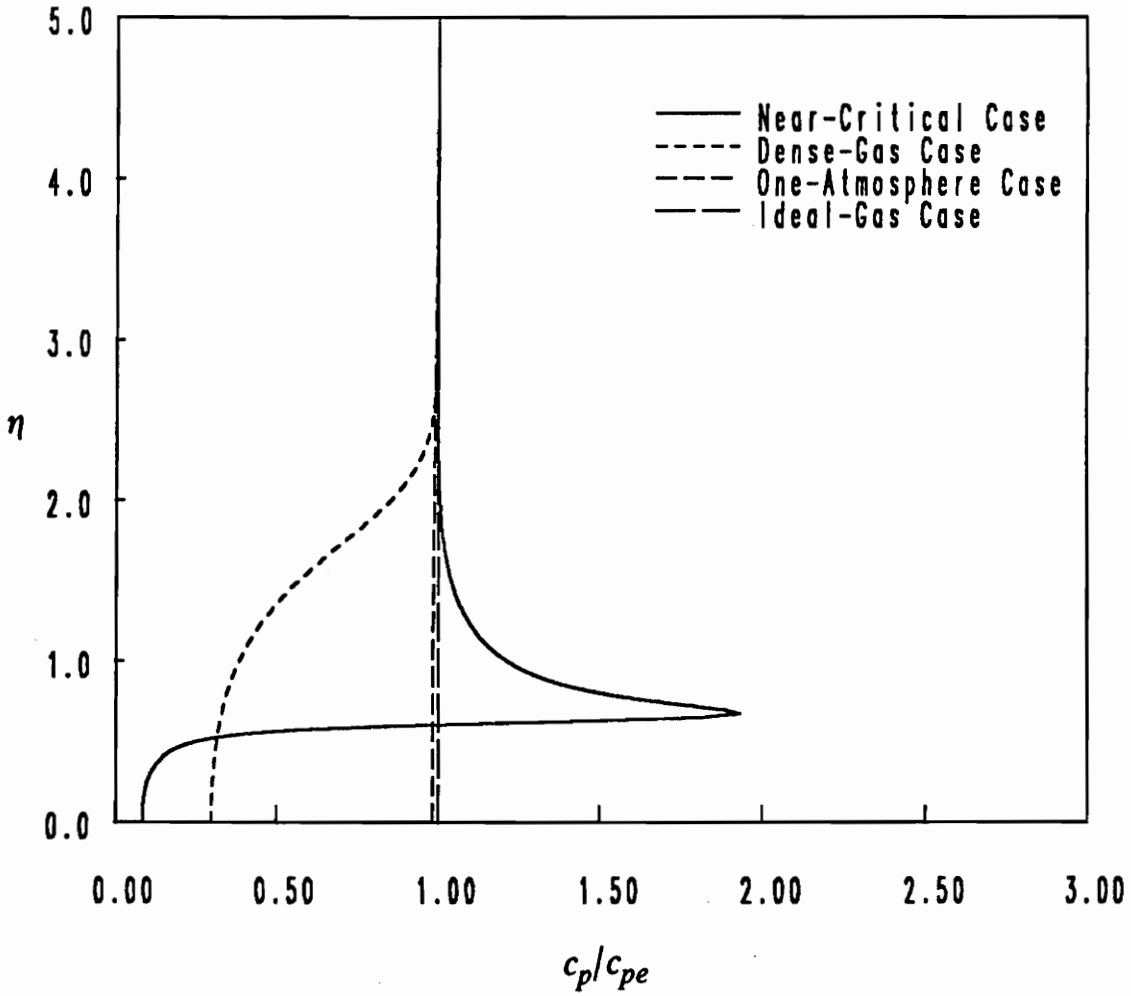

Figure 5.4. Plot of c_p/c_{pe} vs. η for nitrogen at various freestream densities: Illustrated are the results for a freestream Mach number of 2.0 and a freestream temperature of $1.01*T_c$. The one-atmosphere case corresponds to a freestream volume of $115*v_c$.

of viscous dissipation in the near-critical boundary-layer flow. Consequently, the near-critical flow exhibits only minimal temperature increase throughout the boundary layer.

The Prandtl number, which may be interpreted as the ratio of momentum to thermal diffusion, normally controls the relative size of the velocity and thermal boundary layers. Thus, an examination of Figure 5.8 can provide insight into the observed decrease in the relative size of the thermal boundary layer. For the case of the one-atmosphere flow, the Prandtl number is approximately 0.7. As a result, the velocity and thermal profiles are of roughly the same thickness. In the dense-gas case, however, the freestream Prandtl number is approximately 3 and, as a result, the dense-gas momentum layer is thicker than its thermal layer. The freestream Prandtl number for the near-critical flow is approximately 15 and the maximum Prandtl number in the near-critical flow is nearly twice the freestream value. Consequently, the near-critical momentum layer is substantially larger than the near-critical thermal layer as is evident from the velocity and temperature profiles shown in Figures 5.1 - 5.3.

In the dense-gas and near-critical cases, the Prandtl number approaches the one-atmosphere value in the vicinity of the wall. This behavior seems to suggest that the dense-gas and near-critical flows approach an ideal-gas region at the wall even though the variation of the viscosity in these cases suggests that the flow is virtually liquid-like. Similar results have been noted by Hendricks et al. (1962) and Tanaka et al. (1971) in which the presence of an ideal-gas wall layer was found to exist in flows exhibiting liquid-like freestreams.

The weak temperature variation of the near-critical boundary layer would seem to suggest very little density variation in the near-critical case, at least if ideal-gas intuition is employed. The variation of the density through the thickness of the boundary layer depicted in Figure 5.6, however, demonstrates that the near-critical flow actually exhibits the largest amount of density variation of the three cases in spite of exhibiting the least amount of temperature increase. As noted by Martin and Hou (1955), in the vicinity of the critical point, the isotherms are necessarily nearly horizontal. Consequently, small changes in temperature at constant pressure yield large variations in density for flows in this near-critical region.

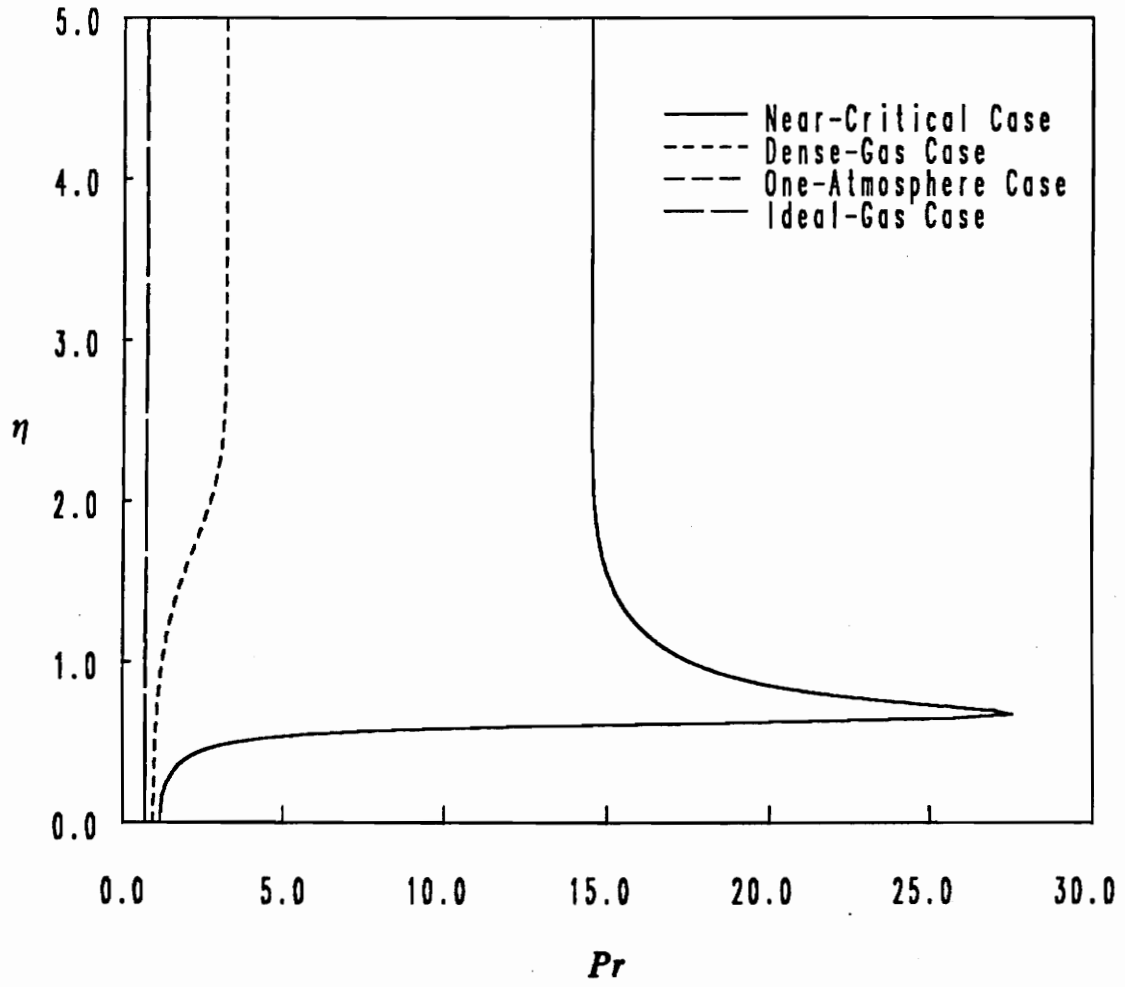

Figure 5.5. Plot of Pr vs. η for nitrogen at various freestream densities: Illustrated are the results for a freestream Mach number of 2.0 and a freestream temperature of $1.01*T_c$. The one-atmosphere case corresponds to a freestream volume of $115*v_c$.

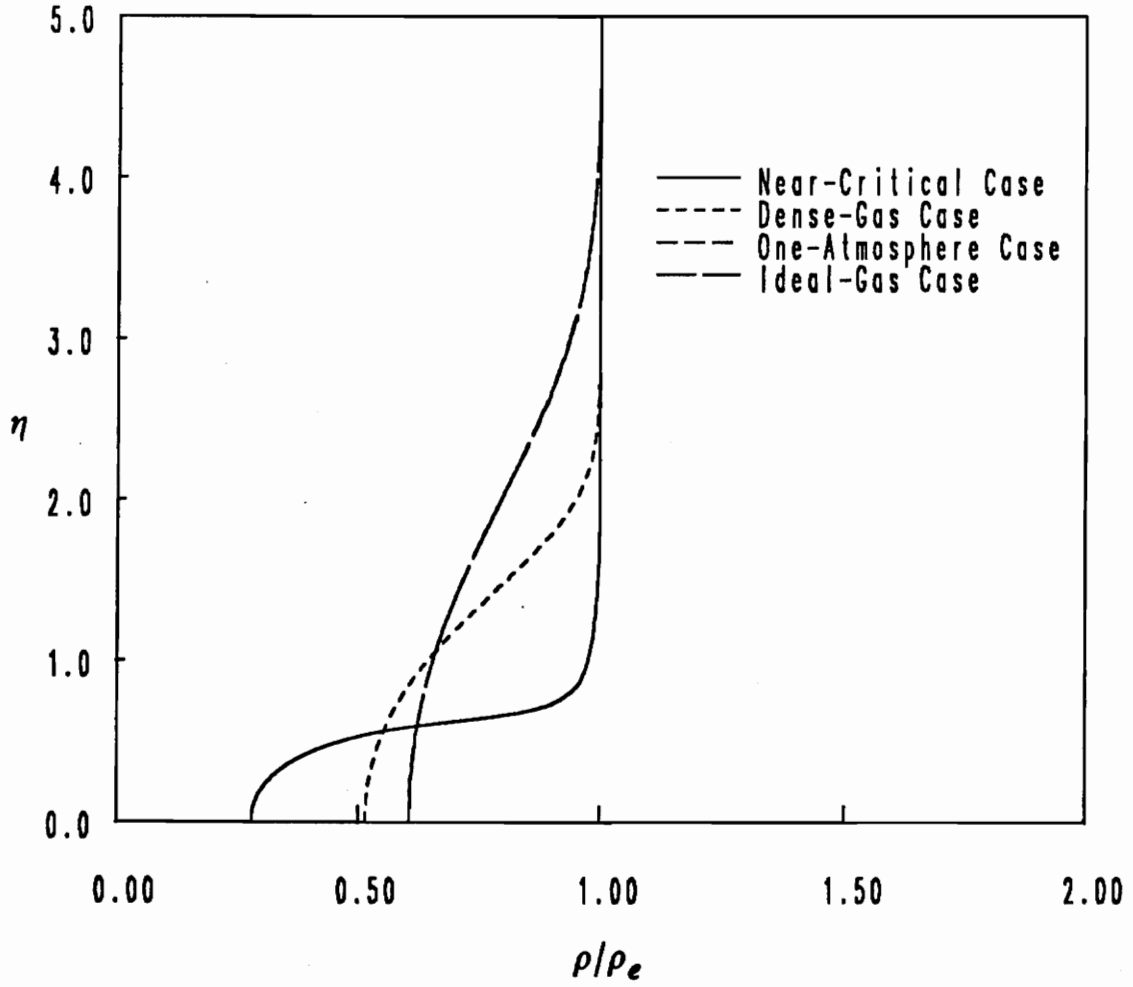

Figure 5.6. **Plot of ρ/ρ_e vs. η for nitrogen at various freestream densities:** Illustrated are the results for a freestream Mach number of 2.0 and a freestream temperature of $1.01*T_c$. The one-atmosphere case corresponds to a freestream volume of $115*v_c$.

The density variation for the dense-gas case shown in Figure 5.6 also exhibits, by ideal-gas standards, a disproportionate decrease in density relative to the temperature increase, although not as extreme as in the near-critical case. This non-ideal behavior, as with the near-critical case, is also due to the decrease in the magnitude of the slope of the isotherms in the dense-gas regime.

The variations of viscosity and thermal conductivity through the thickness of the boundary layer for the various freestream volumes are depicted in Figures 5.7 and 5.8. The reason for the dramatic differences in the variation of viscosity and thermal conductivity among the three cases is the freestream "starting point" of the viscosity and thermal conductivity in each case. The one-atmosphere flow has freestream conditions in the region in which increases in temperature produce increases in the values of the viscosity and thermal conductivity. The temperature increase of the flow associated with the adiabatic-wall case shown here yields the expected increases in the viscosity and thermal conductivity for the one-atmosphere case as depicted in Figures 5.7 and 5.8.

For the dense-gas case, the freestream pressure and temperature conditions place the freestream viscosity and thermal conductivity near the the local minimum of the viscosity and thermal-conductivity space seen in Figures 1.2 and 1.3. As a result, the flow-temperature increase gives rise to initial decreases in the viscosity and thermal conductivity followed by increases as the viscosity and thermal conductivity pass through the respective local minima. At smaller freestream Mach numbers, the temperature increase of the flow might not be sufficient to push the viscosity and thermal conductivity past their local minima. The resulting wall values for viscosity and thermal conductivity for such a case would then be considerably less than the respective freestream values. Likewise, for larger freestream Mach numbers, the temperature increase of the flow may be so large as to force the viscosity and thermal conductivity well into the region where temperature increases yield increases in the values of the two quantities. Consequently, the wall values for the viscosity and thermal conductivity would exceed their freestream values.

The local minima in the viscosity and thermal conductivity seen in Figures 5.7 and 5.8 are also present in the near-critical flow. The primary difference between the near-critical and the dense-gas cases is the larger changes in μ and k experienced by the near-critical fluid. This behavior is

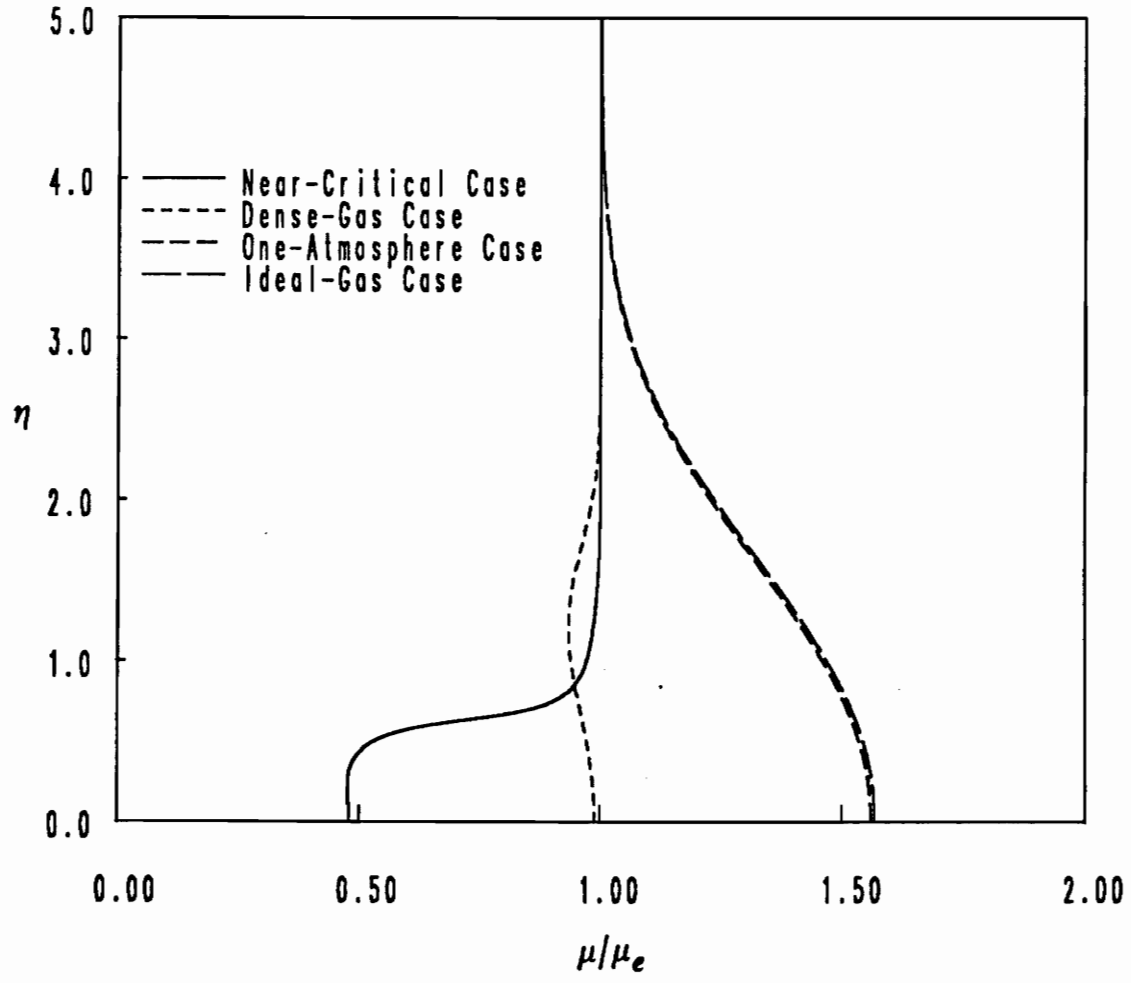

Figure 5.7. **Plot of μ/μ_e vs. η for nitrogen at various freestream densities:** Illustrated are the results for a freestream Mach number of 2.0 and a freestream temperature of $1.01*T_c$. The one-atmosphere case corresponds to a freestream volume of $115*v_c$.

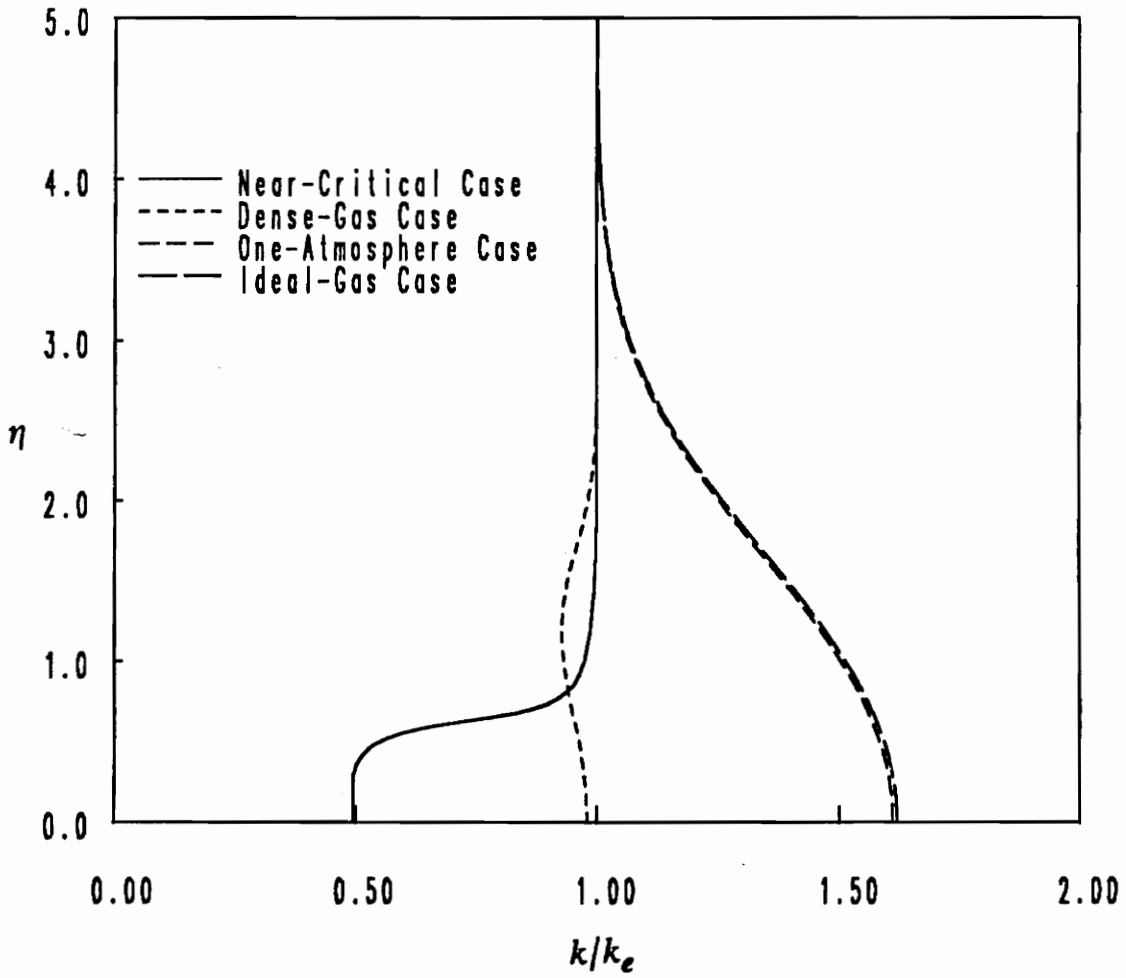

Figure 5.8. Plot of k/k_e vs. η for nitrogen at various freestream densities: Illustrated are the results for a freestream Mach number of 2.0 and a freestream temperature of $1.01*T_c$. The one-atmosphere case corresponds to a freestream volume of $115*v_c$.

consistent with the corresponding states results plotted in Figures 1.2 and 1.3 where it is seen that the local minima in μ and k are always most pronounced in the near-critical region.

Nitrogen: Global-Flow Variables

The preceding discussion of the local-flow variables suggests several trends in the behavior of boundary-layer flows as the freestream density is increased. Among these trends is a decrease in wall viscosity and density relative to the ideal-gas values as the freestream conditions approach the thermodynamic critical point. Variations with freestream Mach number of the ratio of wall density to outer-edge density and the value of ℓ at the wall, ℓ_w, shown in Figures 5.9 and 5.10, confirm this general trend.

A consequence of the decrease in the ℓ_w parameter for higher freestream-density flows is a decrease in the corresponding values of the skin-friction coefficient. Figure 5.11, which is a plot of the computed skin-friction coefficient relative to the Blasius value for a range of freestream Mach numbers, indicates that the near-critical and dense-gas boundary layers exhibit considerably smaller values of the skin-friction coefficient relative to that of the one-atmosphere case in spite of the fact that the gradients of F at the wall for the near-critical and dense-gas cases are larger than those of the one-atmosphere case.

The substantial decrease in the skin-friction coefficient has immediate consequences on the separation characteristics of the dense-gas and the near-critical boundary-layer flows. Some indication of the effect of the decrease in the skin-friction coefficient on boundary-layer separation may be obtained through the use of triple-deck theory summarized by Adamson and Messiter (1980) and Delery and Marvin (1986). According to the triple-deck scaling laws, the pressure rise necessary to induce separation is proportional to the square root of the skin friction coefficient. Thus, the lower the value of the skin-friction coefficient, the more likely a boundary layer is to

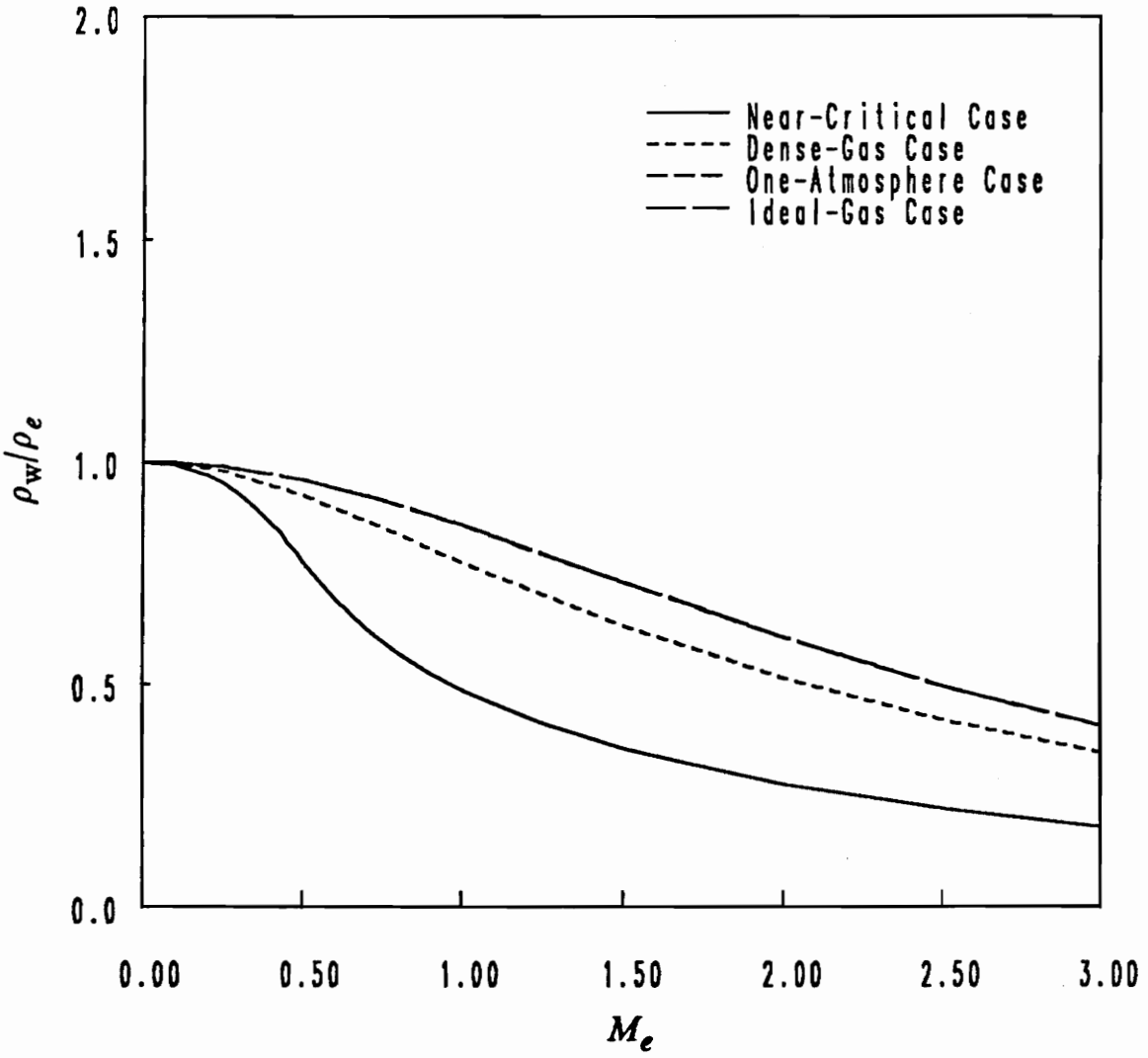

Figure 5.9. Plot of ρ_w/ρ_e vs. M_e for nitrogen at various freestream densities: Illustrated are the results for a freestream temperature of $1.01*T_c$. The one-atmosphere case corresponds to a freestream volume of $115*v_c$.

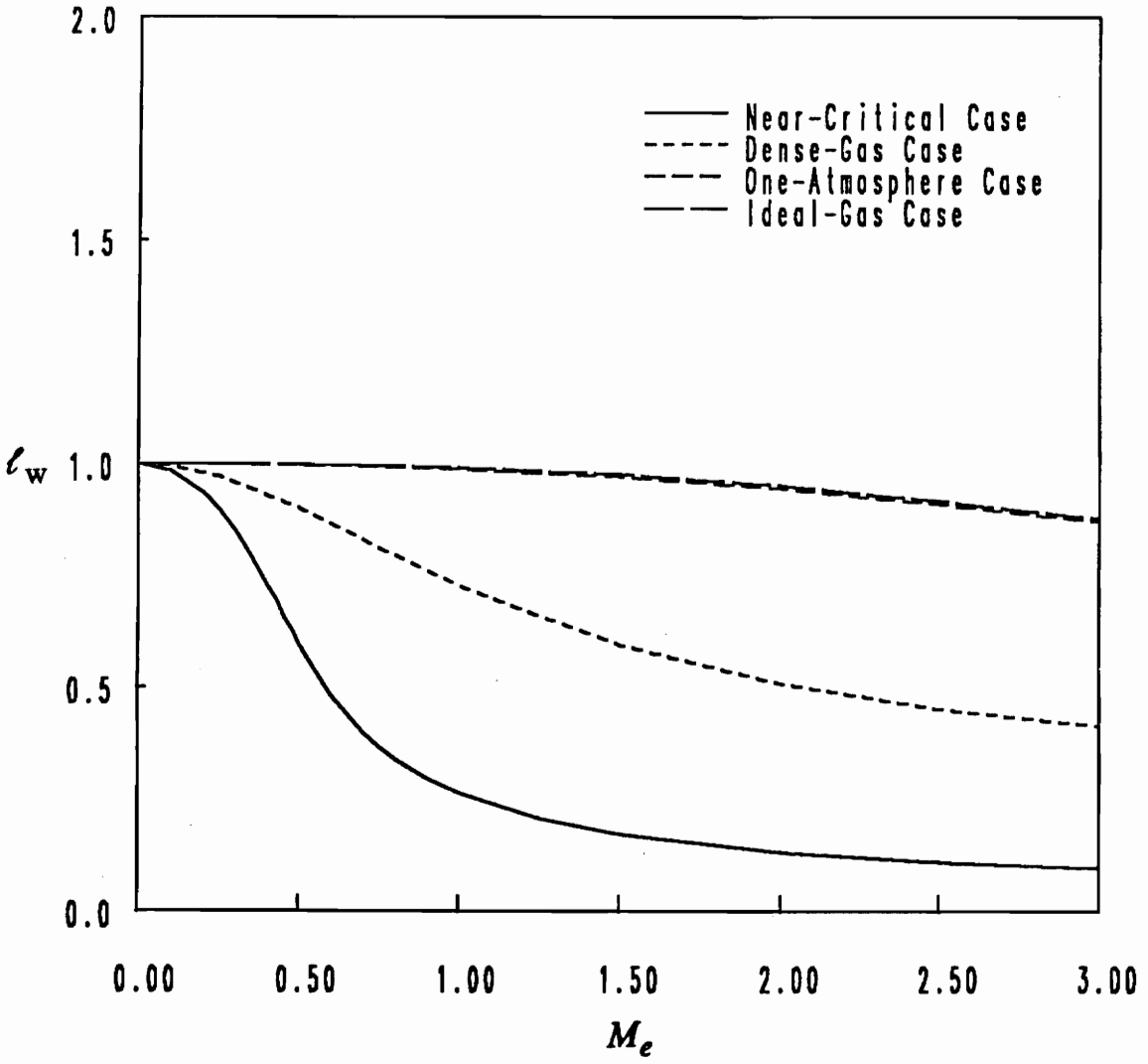

Figure 5.10. Plot of ℓ_w vs. M_e for nitrogen at various freestream densities: Illustrated are the results for a freestream temperature of $1.01*T_c$. The one-atmosphere case corresponds to a freestream volume of $115*v_c$.

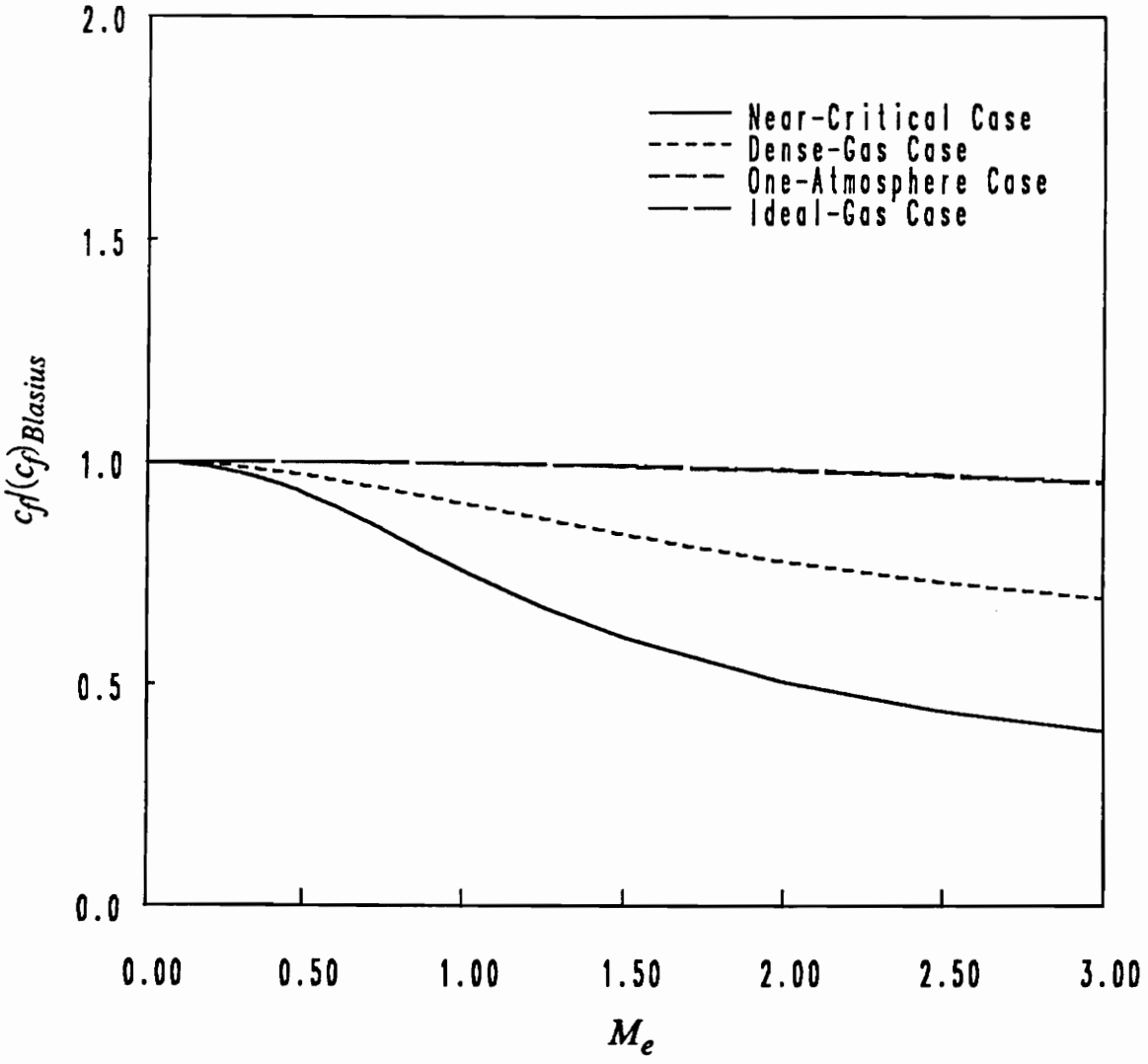

Figure 5.11. Plot of $c_f/(c_f)_{Blasius}$ vs. M_e for nitrogen at various freestream densities: Illustrated are the results for a freestream temperature of $1.01*T_c$. The one-atmosphere case corresponds to a freestream volume of $115*v_c$.

separate. The results presented here thus suggest that the dense-gas and near-critical boundary-layer flows are more susceptible to separation than flows at lower pressures.

Another trend in the behavior of boundary-layer flows is a potential for significant variation in the value of the Prandtl number as the freestream density is increased. Figure 5.12, which depicts the variation of the ratio of wall Prandtl number to outer-edge Prandtl number with freestream Mach number, provides some indication as to the extent of the Prandtl-number variation in the boundary-layer flows. The near-critical Prandtl number varies rapidly throughout the boundary layer over a wide range of freestream Mach numbers. The large local maximum in the Prandtl number seen if Figure 5.5 occurs at the wall at a freestream Mach number of approximately 0.45, causing the Prantdl-number ratio at the wall to exhibit a large local maximum at this freestream Mach number. The dense-gas Prandtl number decreases smoothly from the outer-edge value to the wall value over a wide range of freestream Mach numbers. Furthermore, this decrease is more pronounced as the Mach number increases. In contrast, the one-atmosphere Prandtl number is virtually constant throughout the boundary layer over a wide range of Mach numbers.

An inspection of Figure 5.12 suggests that the Prandtl-number ratio approaches a fixed limit as $M_e \rightarrow \infty$ for each freestream density. In each case, the limiting value of the actual Prandtl number at the wall is found to be the one-atmosphere value of approximately 0.7.

For flows in which the Prandtl number is approximately constant through the boundary layer and the ℓ_w parameter has a value of one, the adiabatic-wall recovery factor varies with the Prandtl number according to the function $b(Pr)$, which can be found in any standard text on boundary layers; see for example Schlichting (1979). For Prandtl numbers in the vicinity of one and for Prandtl numbers approaching infinity, $b(Pr)$ may be reasonably approximated by the expressions given in Equation (4.6). Consequently, the adiabatic-wall temperature may be found from a simple expression which is dependent on the freestream Mach number, the sound speed, the specific heat, and the Prandtl number.

A plot of the recovery factor scaled to the appropriate Prandtl-number expressions from Equation (4.6) versus Mach number is provided in Figure 5.13. For the one-atmosphere flow, in which the ℓ_w parameter is approximately one and the Prandtl number remains virtually constant

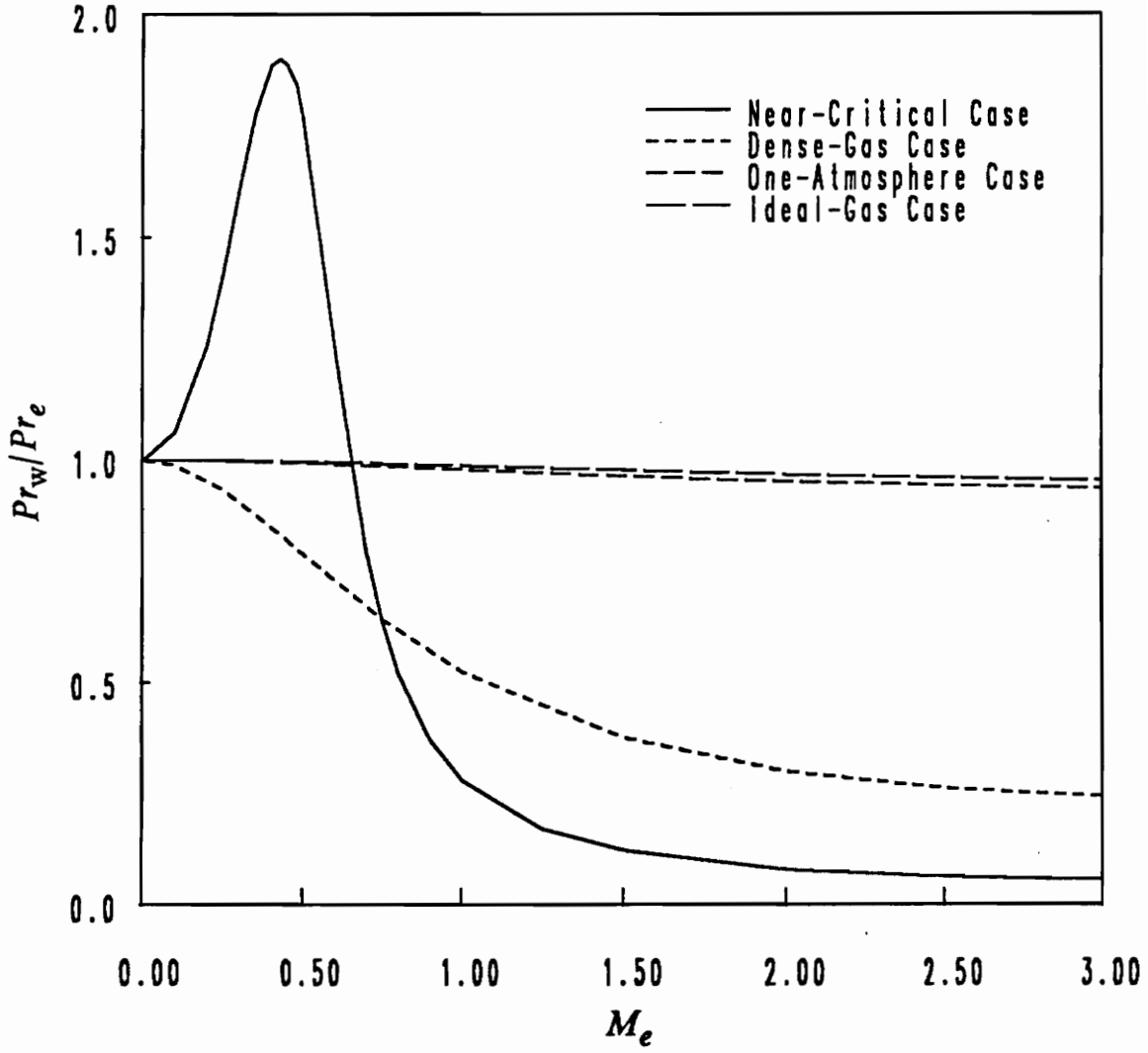

Figure 5.12. Plot of Pr_w/Pr_e vs. M_e for nitrogen at various freestream densities: Illustrated are the results for a freestream temperature of $1.01*T_c$. The one-atmosphere case corresponds to a freestream volume of $115*v_c$.

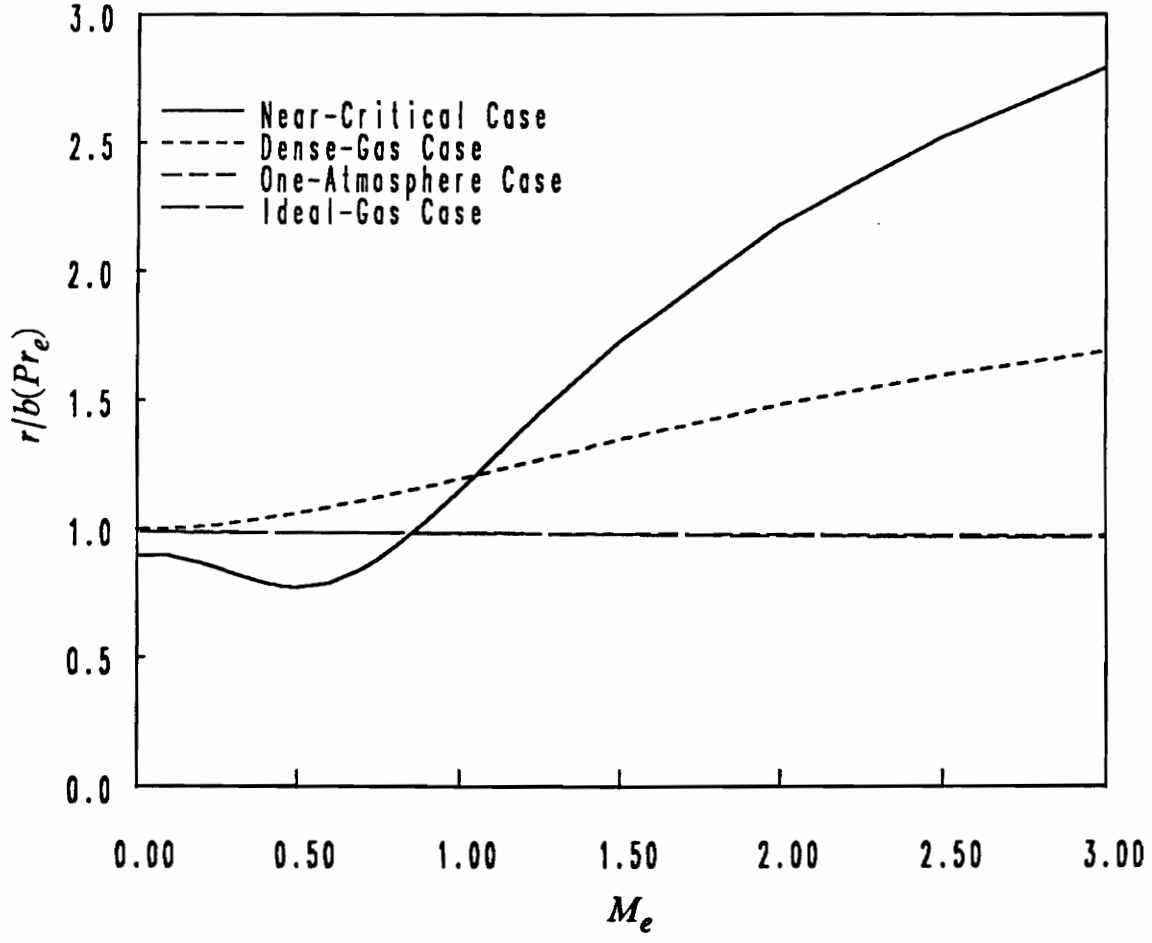

Figure 5.13. Plot of $r/b(Pr_e)$ vs. M_e for nitrogen at various freestream densities: Illustrated are the results for a freestream temperature of $1.01*T_c$. The one-atmosphere case corresponds to a freestream volume of $115*v_c$.

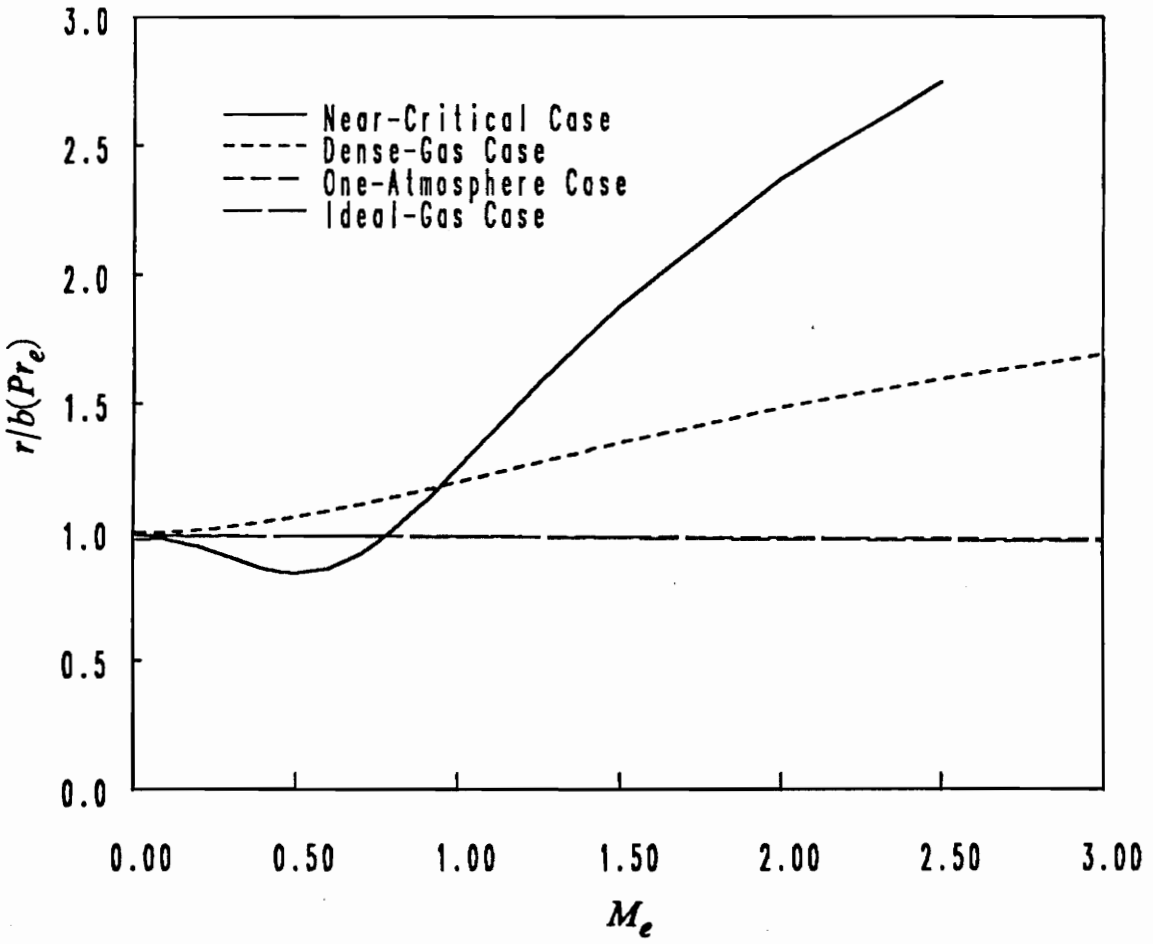

Figure 5.14. Plot of $r/b(Pr_e)$ vs. M_e for nitrogen using the actual $b(Pr_e)$ for the near-critical case: Illustrated are the results for a freestream temperature of $1.01*T_c$. The one-atmosphere case corresponds to a freestream volume of $115*v_c$.

throughout the boundary layer, the scaled value of the recovery factor maintains a value of approximately one for all freestream Mach numbers shown. In contrast, the scaled recovery factor corresponding to the dense-gas and near-critical cases is seen to deviate substantially from a value of one. The reason for the apparent breakdown of the recovery-factor relationship described above is the variation in the ℓ_w parameter and the Prandtl number found in the dense-gas and near-critical flows. However, in the incompressible limit where the Prandtl number is approximately constant and the ℓ_w parameter is roughly one, Equation (4.6) should be recovered.

An inspection of Figure 5.13 yields an apparent contradiction to the assertion that the near-critical flows recover the standard recovery-factor result in the incompressible limit. For in the $M_e \rightarrow 0$ limit, the near-critical scaled recovery factor does not have a value of one. The discrepancy is due to the small but intrinsic error in the approximations of Equation (4.6). If more accurate values of $b(Pr)$ are employed, for example those taken from Figure 12.10 of Schlichting (1979), it is observed that the $M_e \rightarrow 0$ limit is in better agreement with the theory. For the sake of illustration, the graphical results just mentioned have been used to rescale the recovery factor; the results have been plotted in Figure 5.14.

Comparison of Fluids: Local-Flow Variables

To illustrate the effect of increasing specific heat on the local-flow variables in boundary layers, results for the flows of nitrogen, sulfur hexafluoride, and toluene over a flat plate with an adiabatic wall have been computed. The results are for flows with freestream conditions corresponding to the one-atmosphere, dense-gas, and near-critical cases at a freestream Mach number of 2.0. For the one-atmosphere case, the outer-edge values of the specific heat for sulfur hexafluoride and toluene are approximately 3.4 and 6.4 times that of nitrogen. In the dense-gas flows, the sulfur-hexafluoride and toluene outer-edge specific-heats, c_{pe}, are approximately 1.7 and 2.6 times the corresponding nitrogen value. Finally, for the near-critical case, the specific-heat values at the outer edge of the

boundary layer for sulfur hexafluoride and toluene are approximately 1.3 and 1.7 times the outer-edge value for nitrogen.

The predominant effect of the increase in the specific heat on the boundary-layer flows is a decrease in the influence of the viscous dissipation. This decrease is responsible for a corresponding decrease in the temperature variation throughout the boundary layer. As the temperature variation is minimized, so is the variation through the boundary layer of all of the local flow variables. The ultimate result is a trend toward a quasi-Blasius boundary layer.

The distributions of horizontal velocity, vertical velocity, temperature, density, Prandtl number, and viscosity through the boundary layer are plotted in Figures 5.15 - 5.32. An examination of Figures 5.21 - 5.23 reveals temperature variations which approach those of an isothermal flow as the fluid specific heat increases. The corresponding velocity distributions are also seen to approach the quasi-Blasius solution as the specific heat is increased. The decrease in temperature variation is reflected in a corresponding lack of variation of the density which is consistent with the trend toward the Blasius solution. The decreases in variations of the density and temperature account for decreases in the variations of the Prandtl number and the viscosity as observed in Figures 5.27 - 5.32.

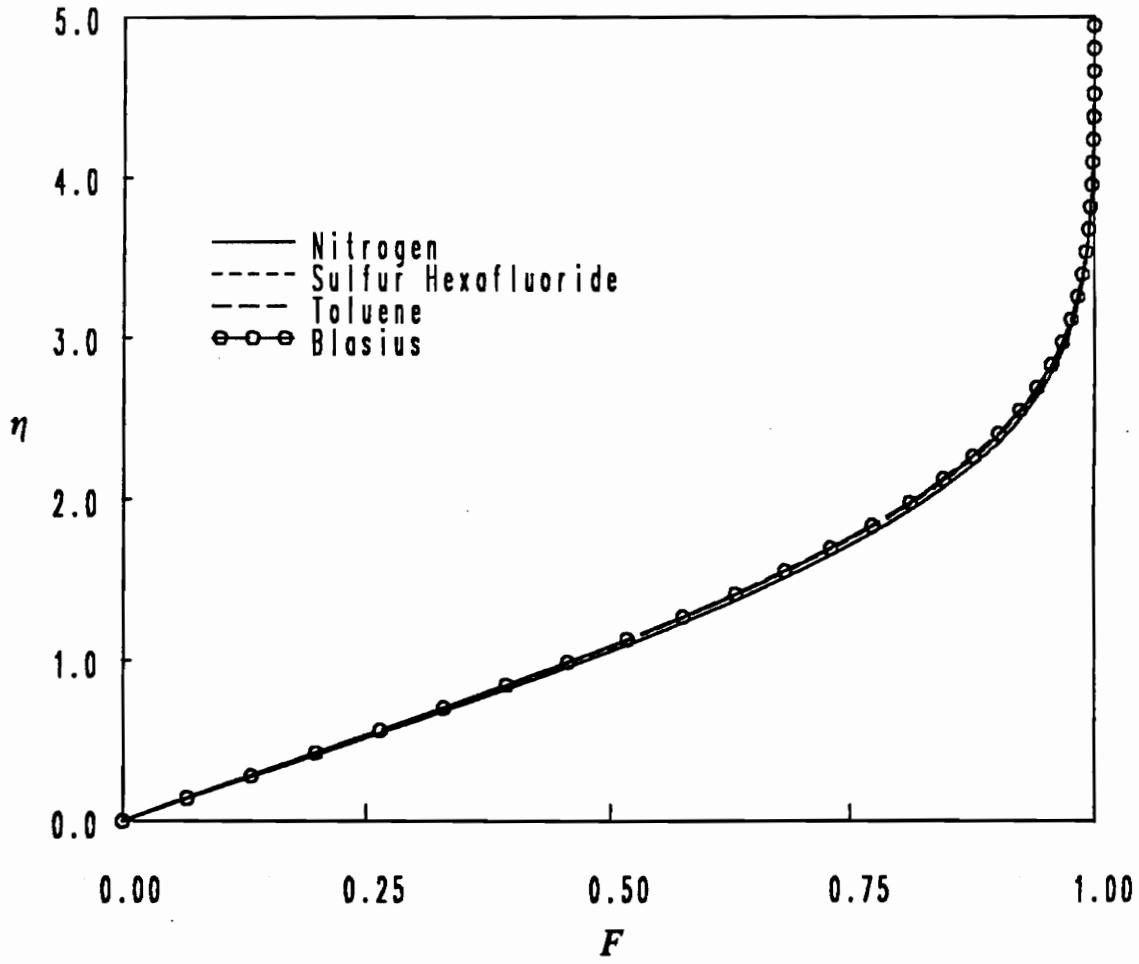

Figure 5.15. Plot of F vs. η for various fluids in a one-atmosphere flow: Illustrated are the results for a freestream Mach number of 2.0 and a freestream temperature of $1.01*T_c$. The freestream volumes for the one-atmosphere flows of nitrogen, sulfur hexafluoride, and toluene are $115*v_c$, $133*v_c$, and $156*v_c$, respectively.

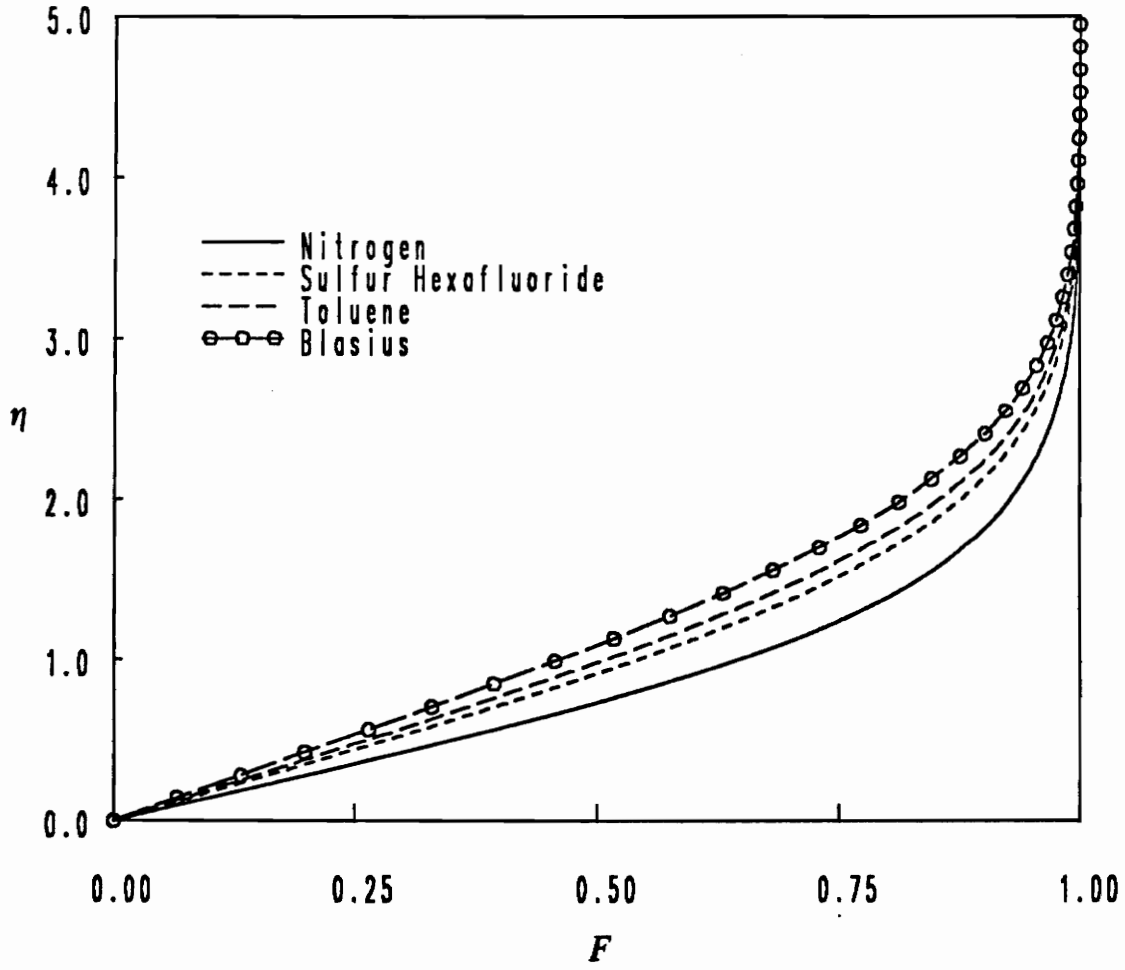

Figure 5.16. Plot of F vs. η for various fluids in a dense-gas flow: Illustrated are the results for a freestream Mach number of 2.0 and a freestream temperature of $1.01 * T_c$.

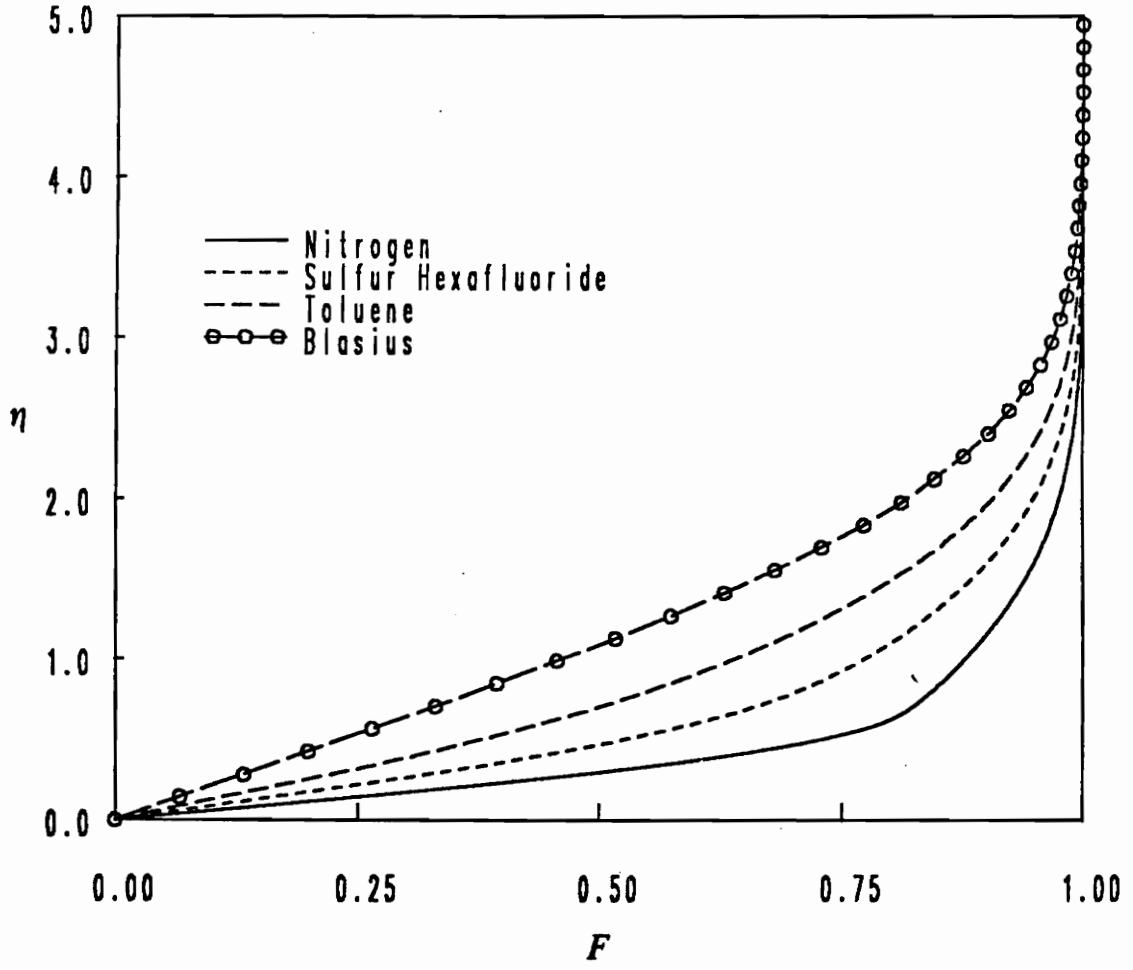

Figure 5.17. **Plot of F vs. η for various fluids in a near-critical flow:** Illustrated are the results for a freestream Mach number of 2.0 and a freestream temperature of $1.01^{*}T_c$.

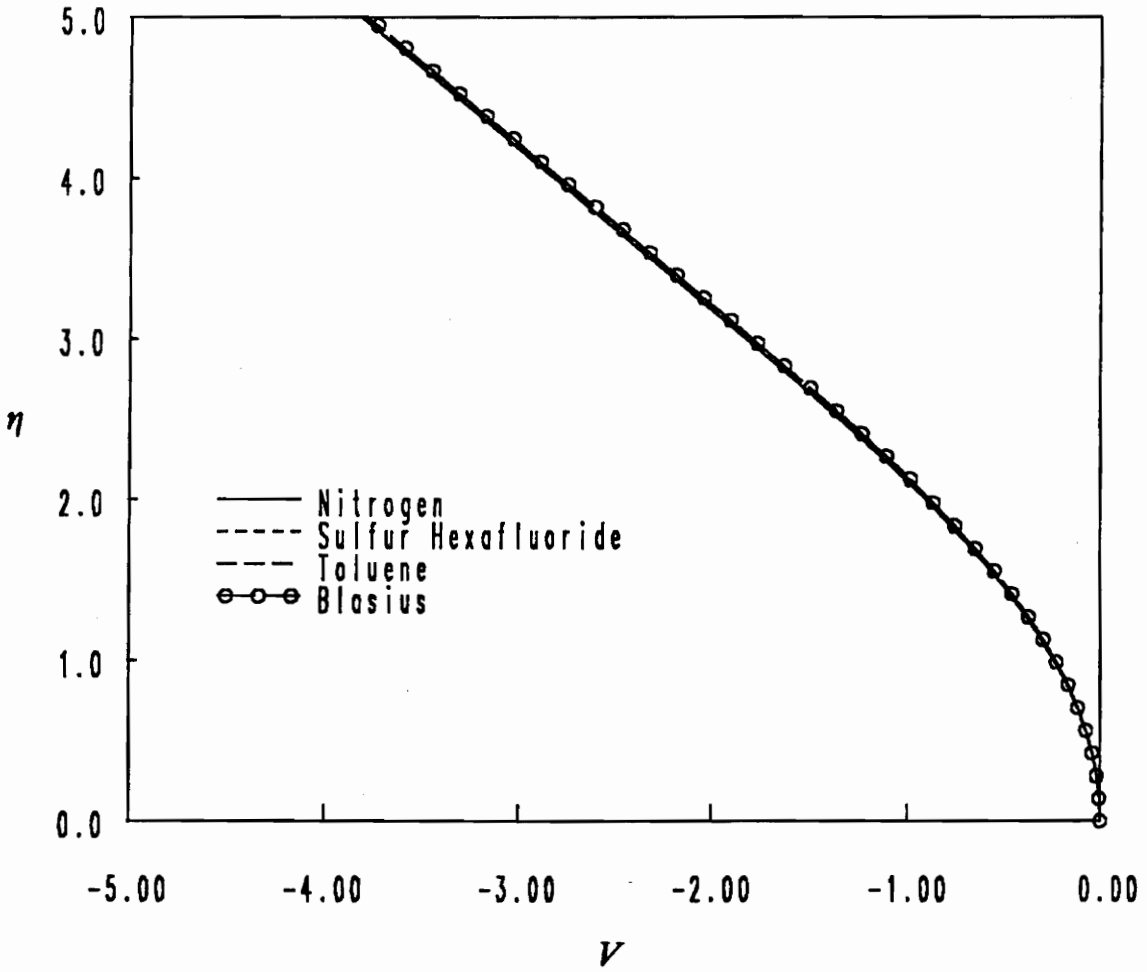

Figure 5.18. **Plot of V vs. η for various fluids in a one-atmosphere flow:** Illustrated are the results for a freestream Mach number of 2.0 and a freestream temperature of $1.01*T_c$. The freestream volumes for the one-atmosphere flows of nitrogen, sulfur hexafluoride, and toluene are $115*v_c$, $133*v_c$, and $156*v_c$, respectively.

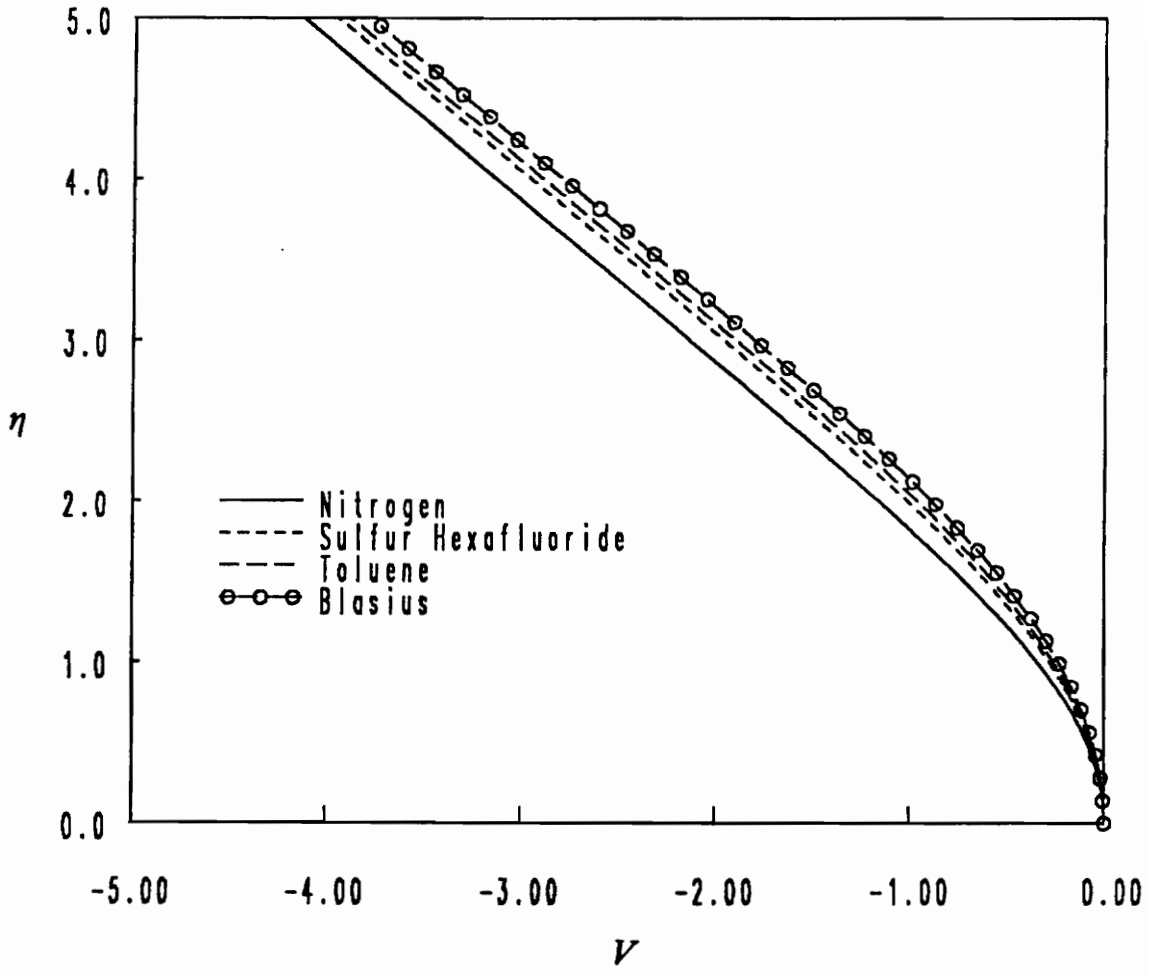

Figure 5.19. Plot of V vs. η for various fluids in a dense-gas flow: Illustrated are the results for a freestream Mach number of 2.0 and a freestream temperature of $1.01 * T_c$.

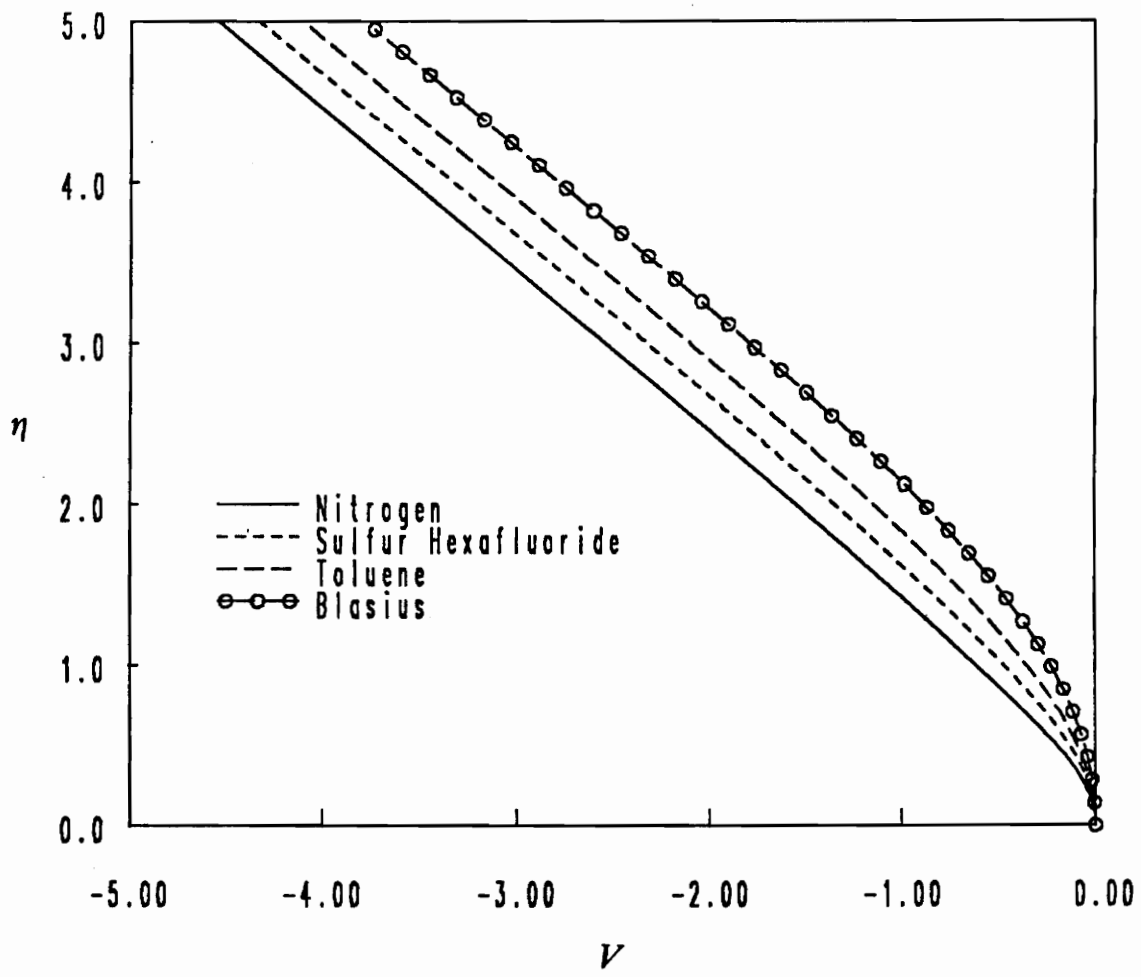

Figure 5.20. Plot of V vs. η for various fluids in a near-critical flow: Illustrated are the results for a freestream Mach number of 2.0 and a freestream temperature of $1.01 * T_c$.

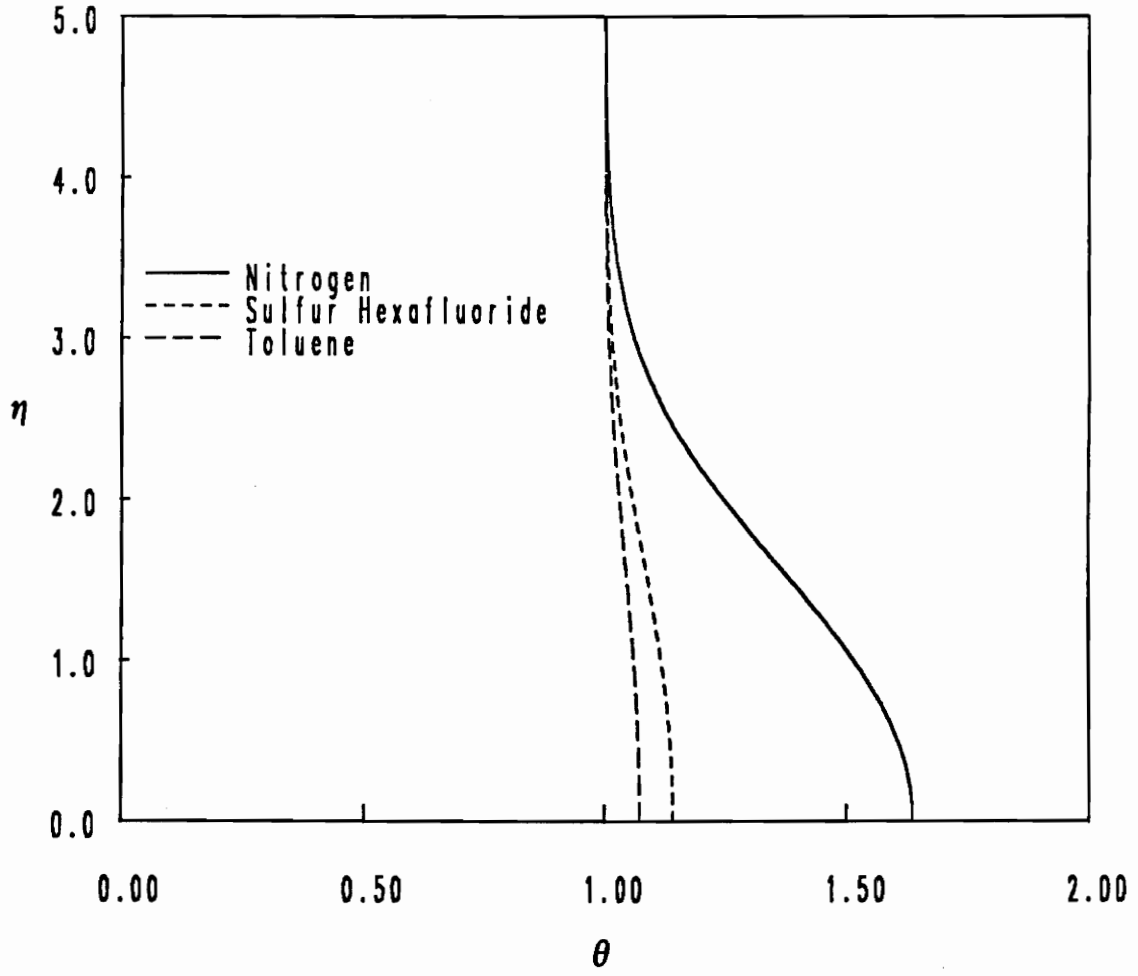

Figure 5.21. Plot of θ vs. η for various fluids in a one-atmosphere flow: Illustrated are the results for a freestream Mach number of 2.0 and a freestream temperature of $1.01*T_c$. The freestream volumes for the one-atmosphere flows of nitrogen, sulfur hexafluoride, and toluene are $115*v_c$, $133*v_c$, and $156*v_c$, respectively.

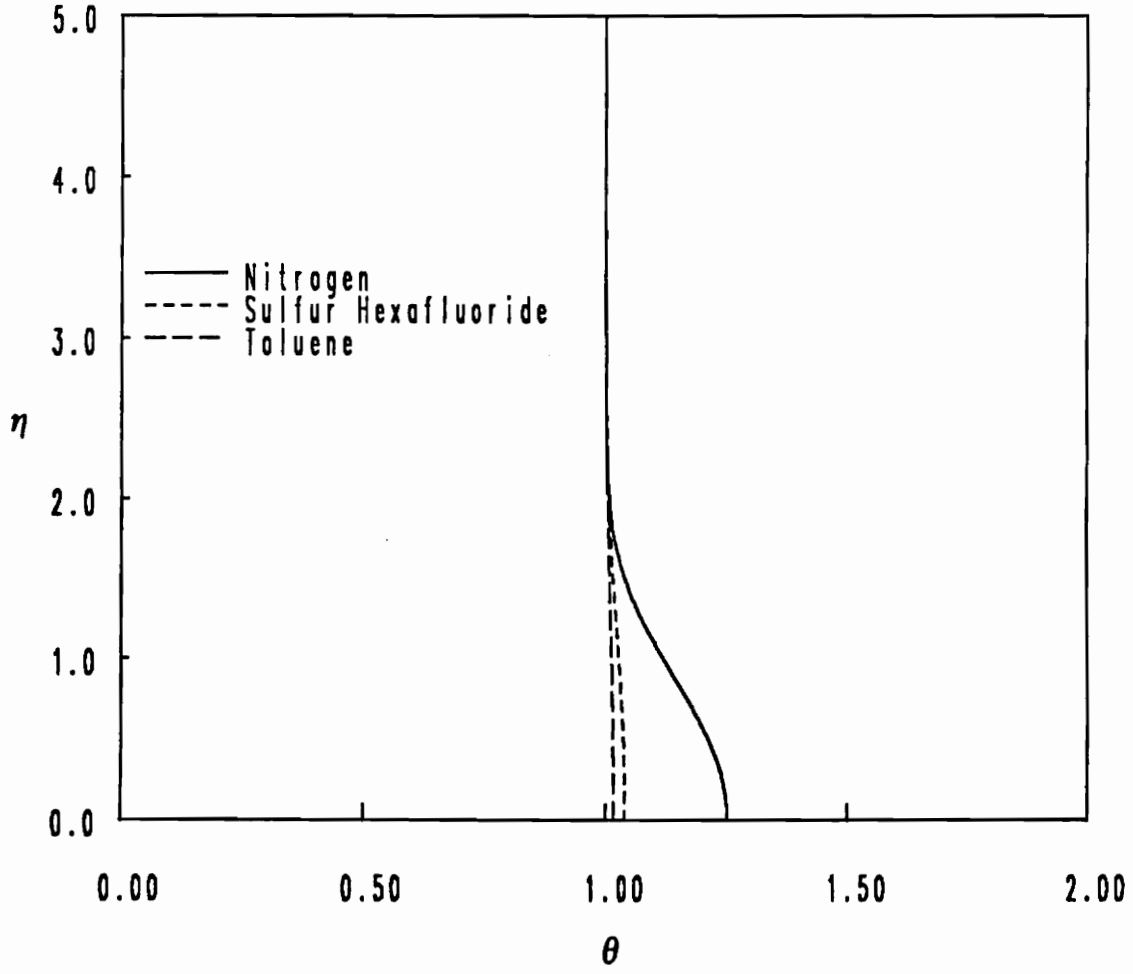

Figure 5.22. Plot of θ vs. η for various fluids in a dense-gas flow: Illustrated are the results for a freestream Mach number of 2.0 and a freestream temperature of $1.01 * T_c$.

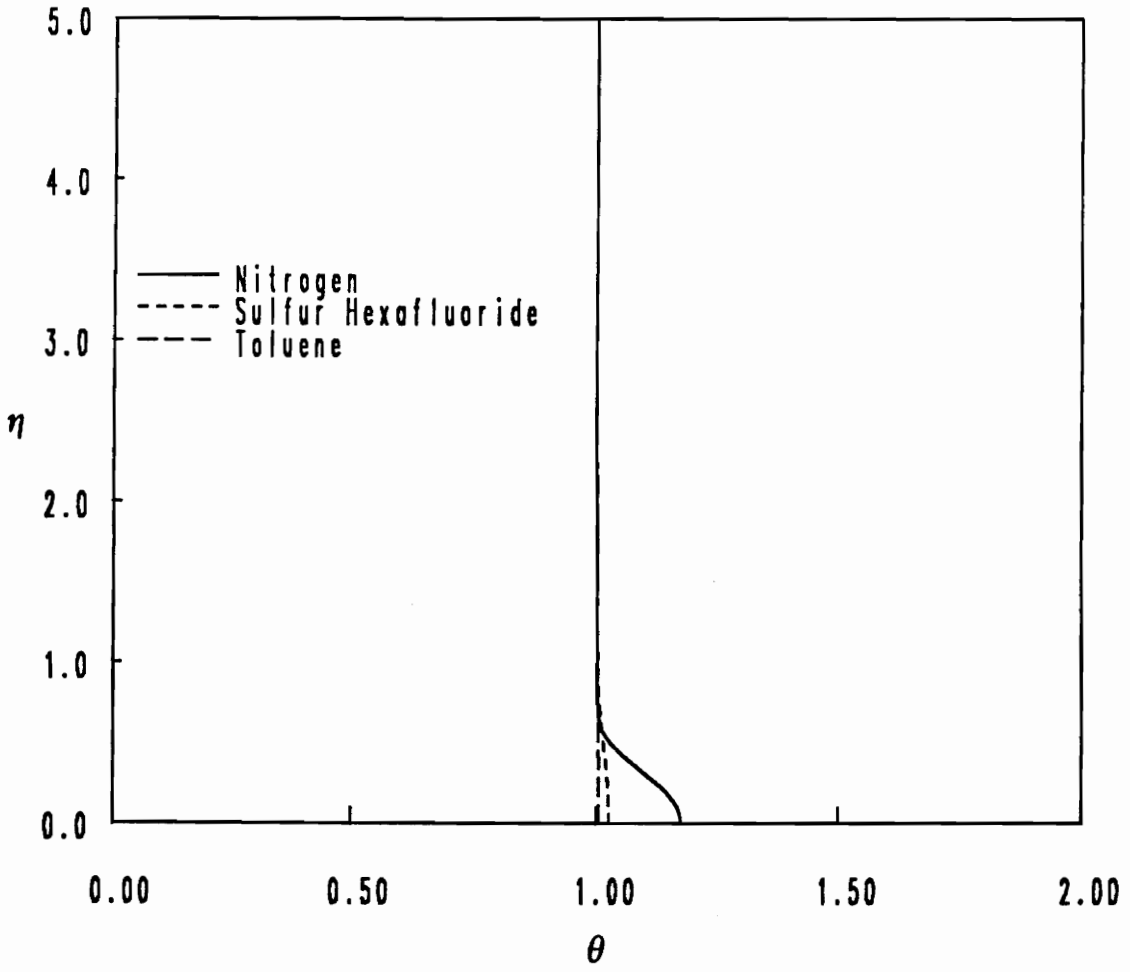

Figure 5.23. **Plot of θ vs. η for various fluids in a near-critical flow:** Illustrated are the results for a freestream Mach number of 2.0 and a freestream temperature of $1.01 * T_c$.

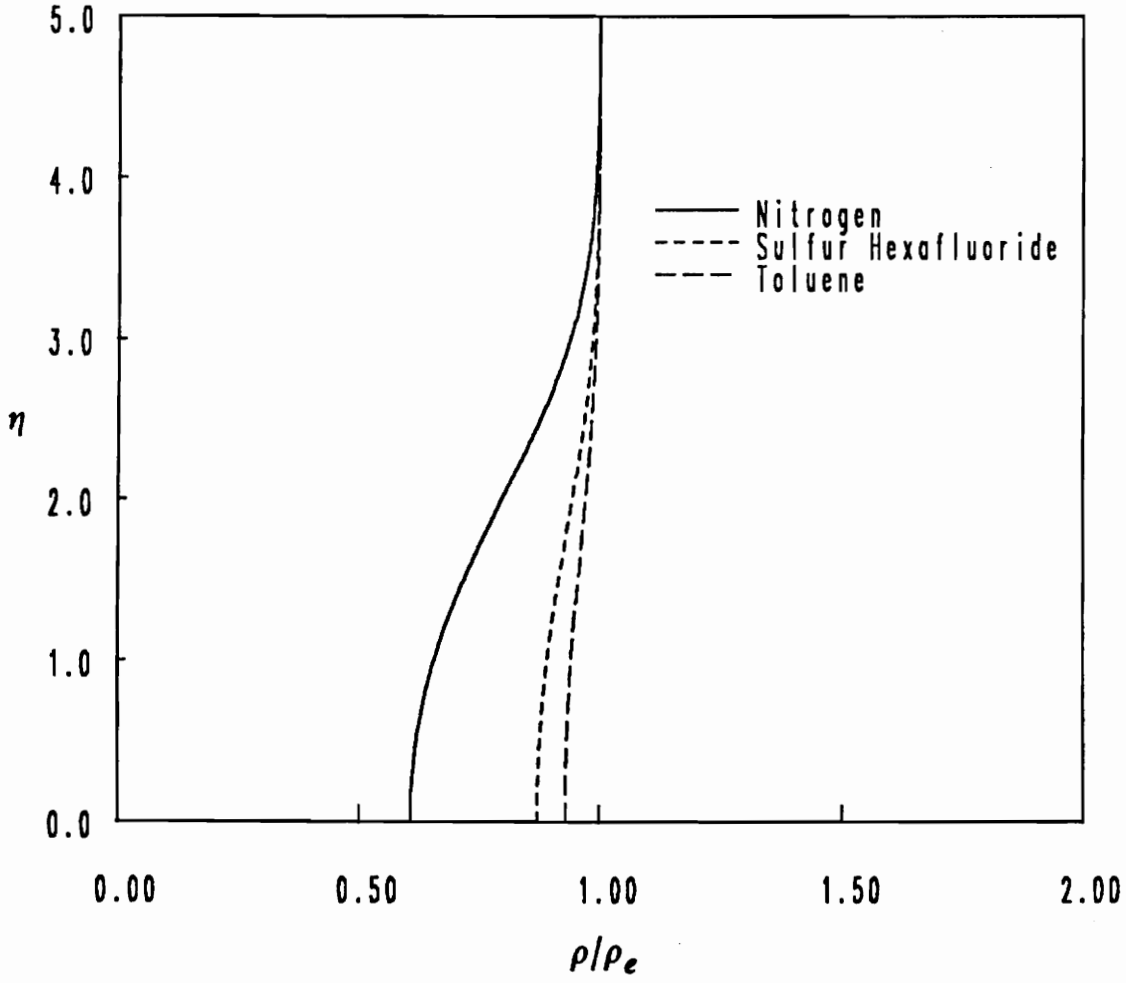

Figure 5.24. **Plot of ρ/ρ_e vs. η for various fluids in a one-atmosphere flow:** Illustrated are the results for a freestream Mach number of 2.0 and a freestream temperature of $1.01*T_c$. The freestream volumes for the one-atmosphere flows of nitrogen, sulfur hexafluoride, and toluene are $115*v_c$, $133*v_c$, and $156*v_c$, respectively.

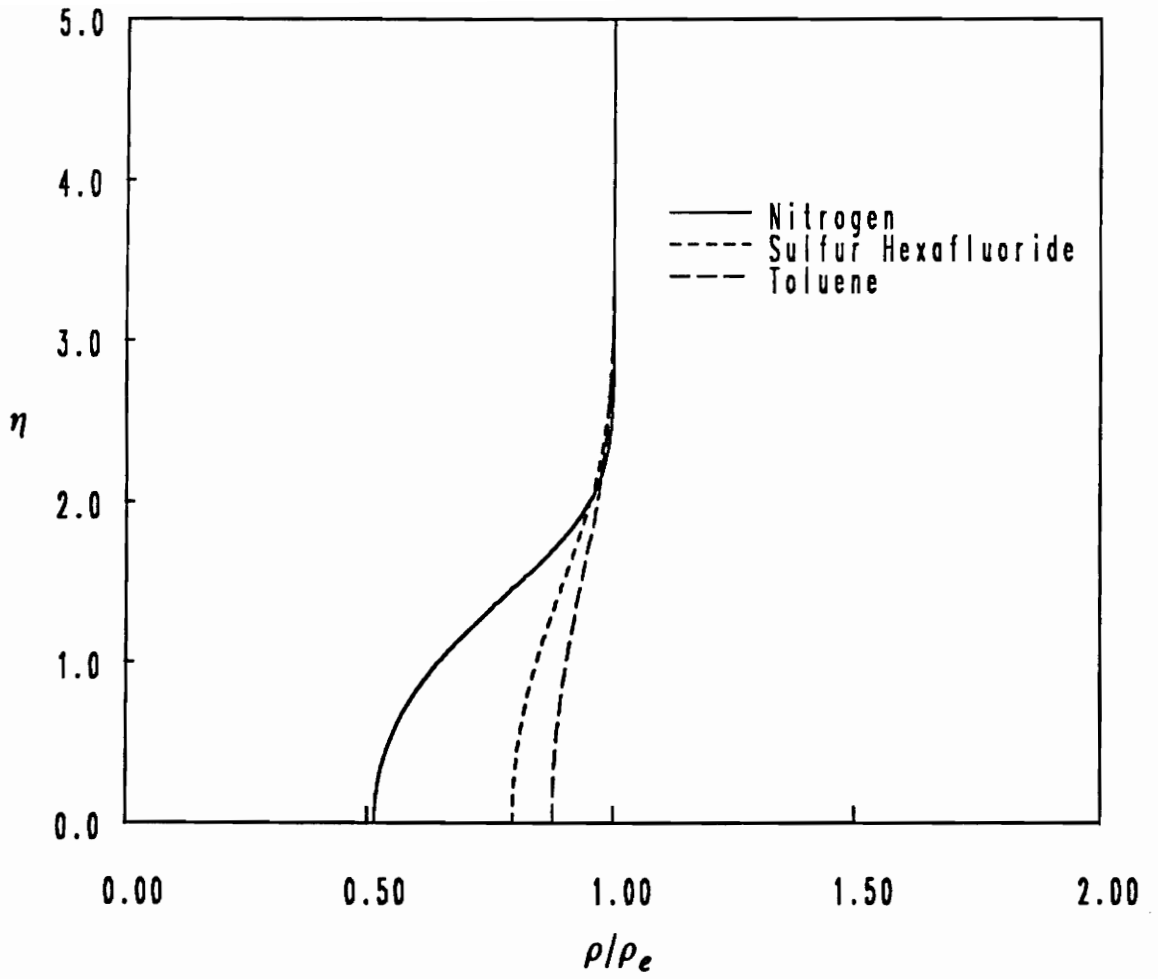

Figure 5.25. Plot of ρ/ρ_e vs. η for various fluids in a dense-gas flow: Illustrated are the results for a freestream Mach number of 2.0 and a freestream temperature of $1.01*T_c$.

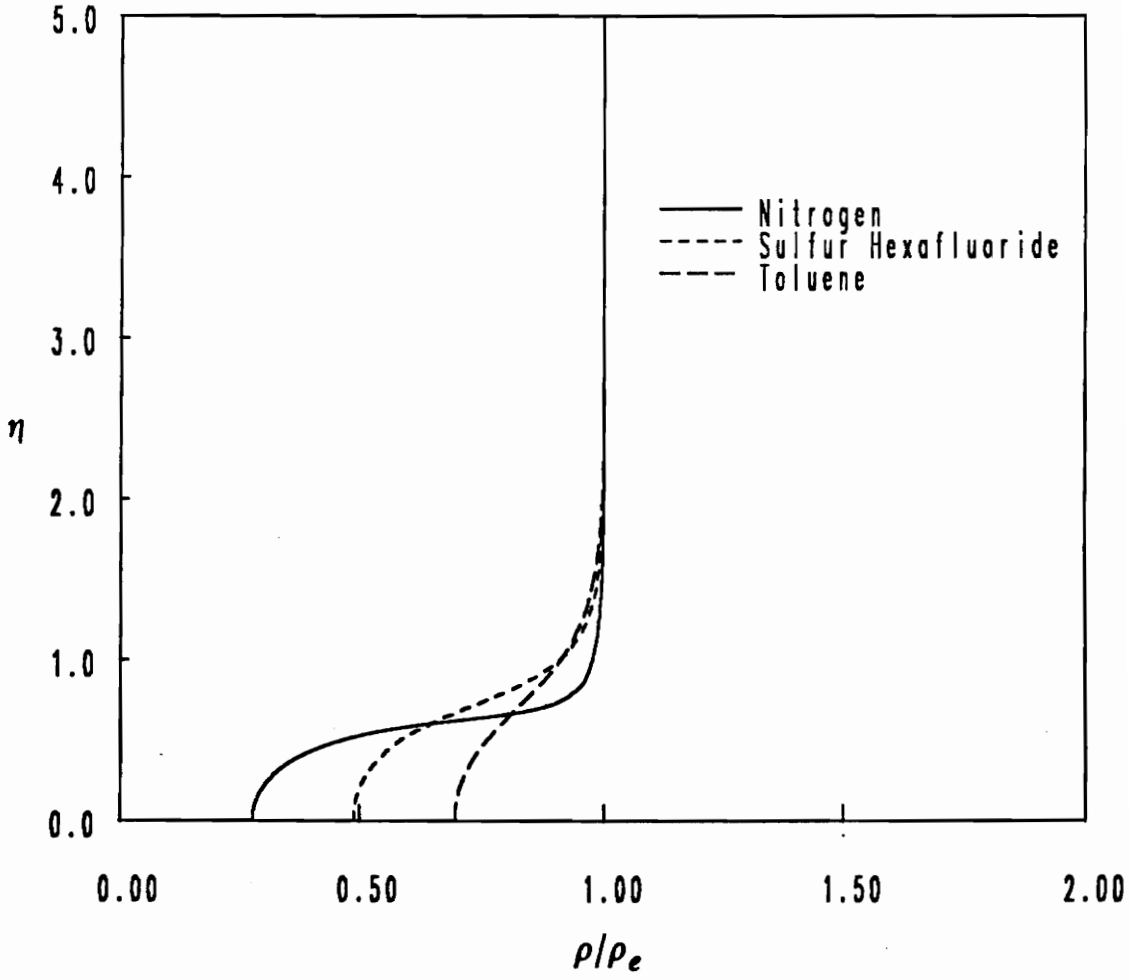

Figure 5.26. Plot of ρ/ρ_e vs. η for various fluids in a near-critical flow: Illustrated are the results for a freestream Mach number of 2.0 and a freestream temperature of $1.01*T_c$.

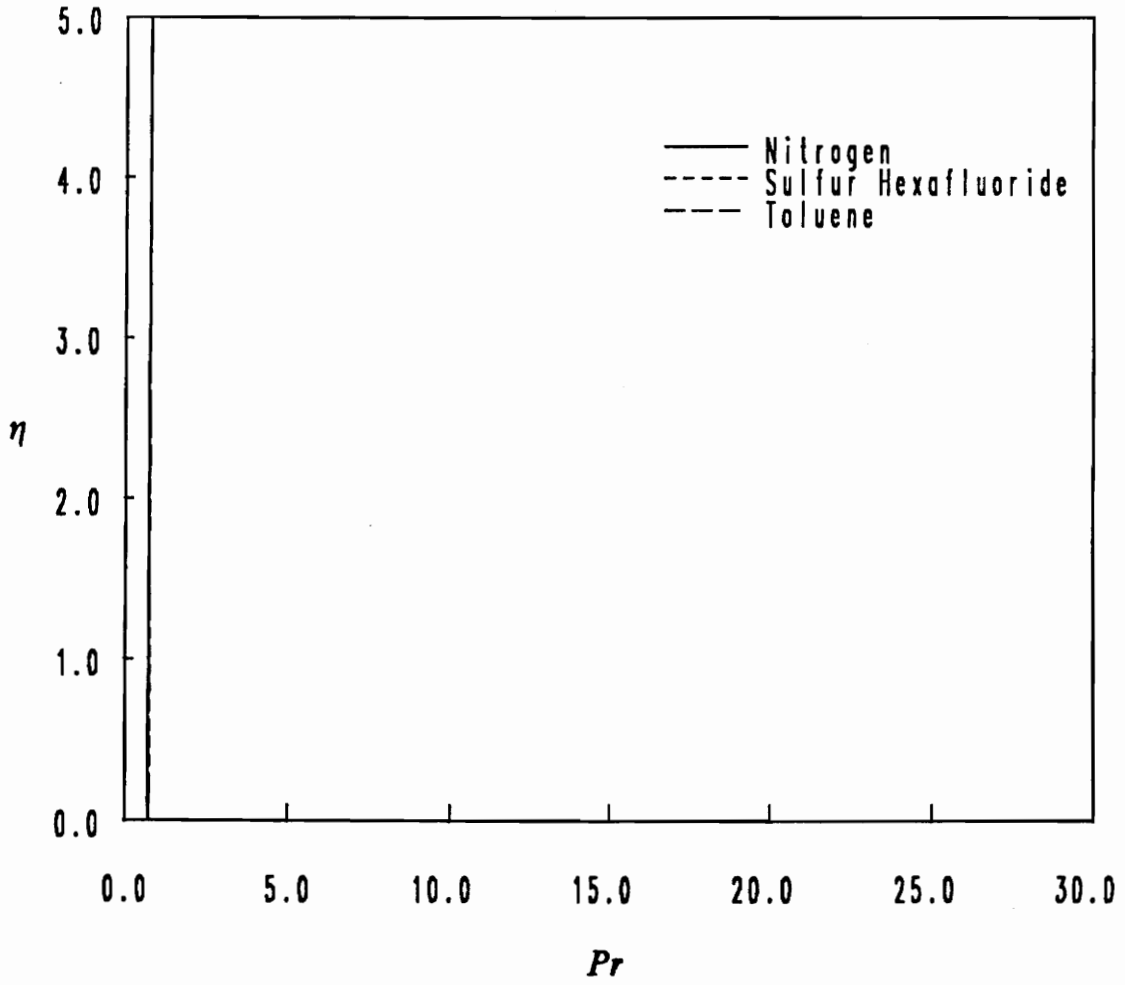

Figure 5.27. Plot of Pr vs. η for various fluids in a one-atmosphere flow: Illustrated are the results for a freestream Mach number of 2.0 and a freestream temperature of $1.01*T_c$. The freestream volumes for the one-atmosphere flows of nitrogen, sulfur hexafluoride, and toluene are $115*v_c$, $133*v_c$, and $156*v_c$, respectively.

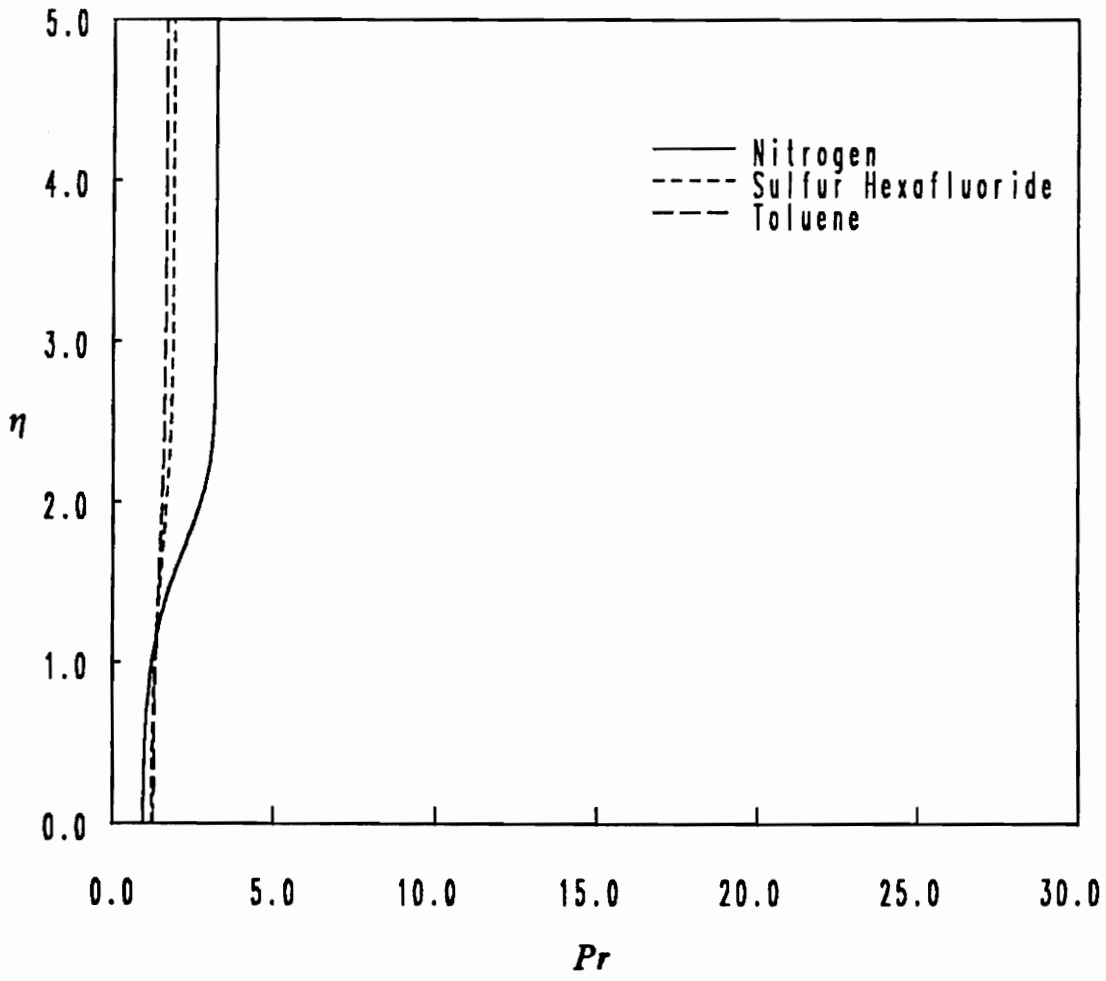

Figure 5.28. Plot of Pr vs. η for various fluids in a dense-gas flow: Illustrated are the results for a freestream Mach number of 2.0 and a freestream temperature of $1.01 * T_c$.

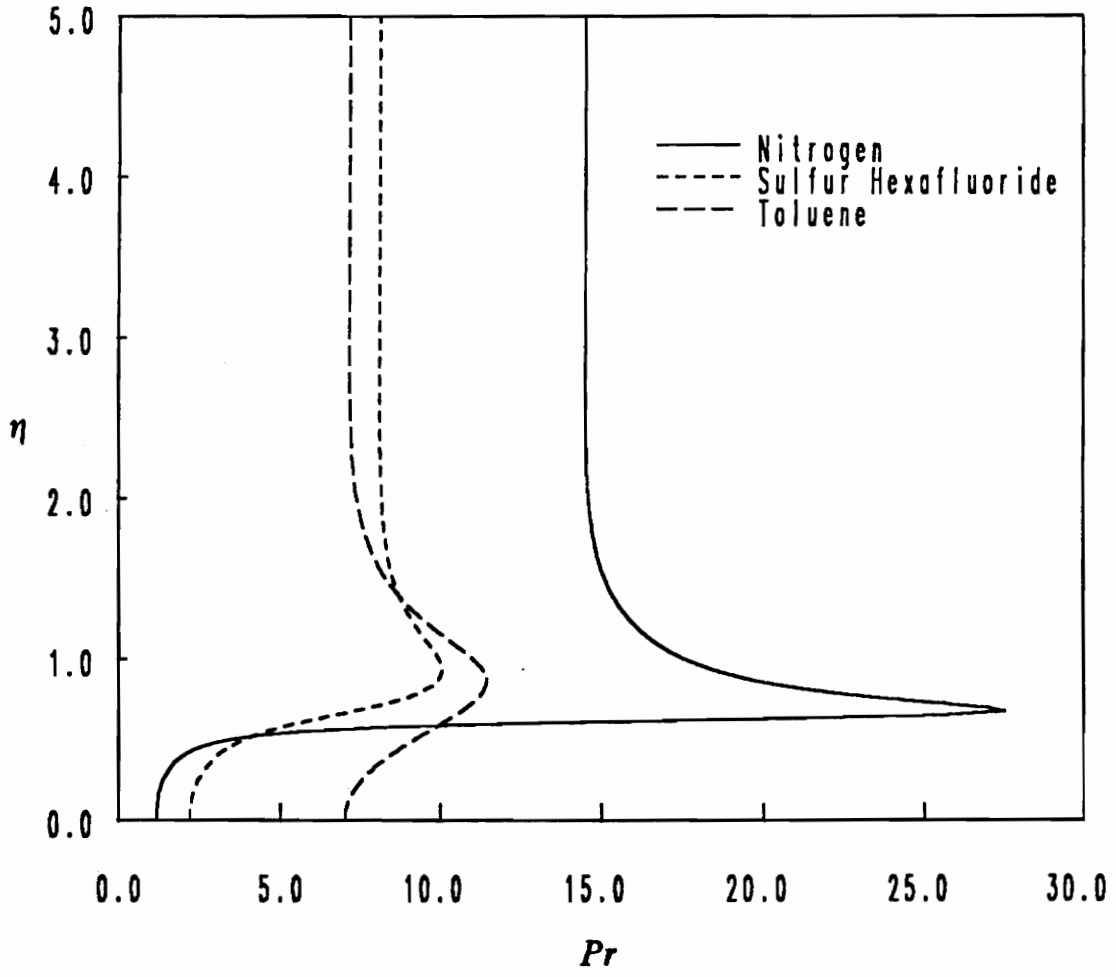

Figure 5.29. Plot of *Pr* vs. η for various fluids in a near-critical flow: Illustrated are the results for a freestream Mach number of 2.0 and a freestream temperature of $1.01*T_c$.

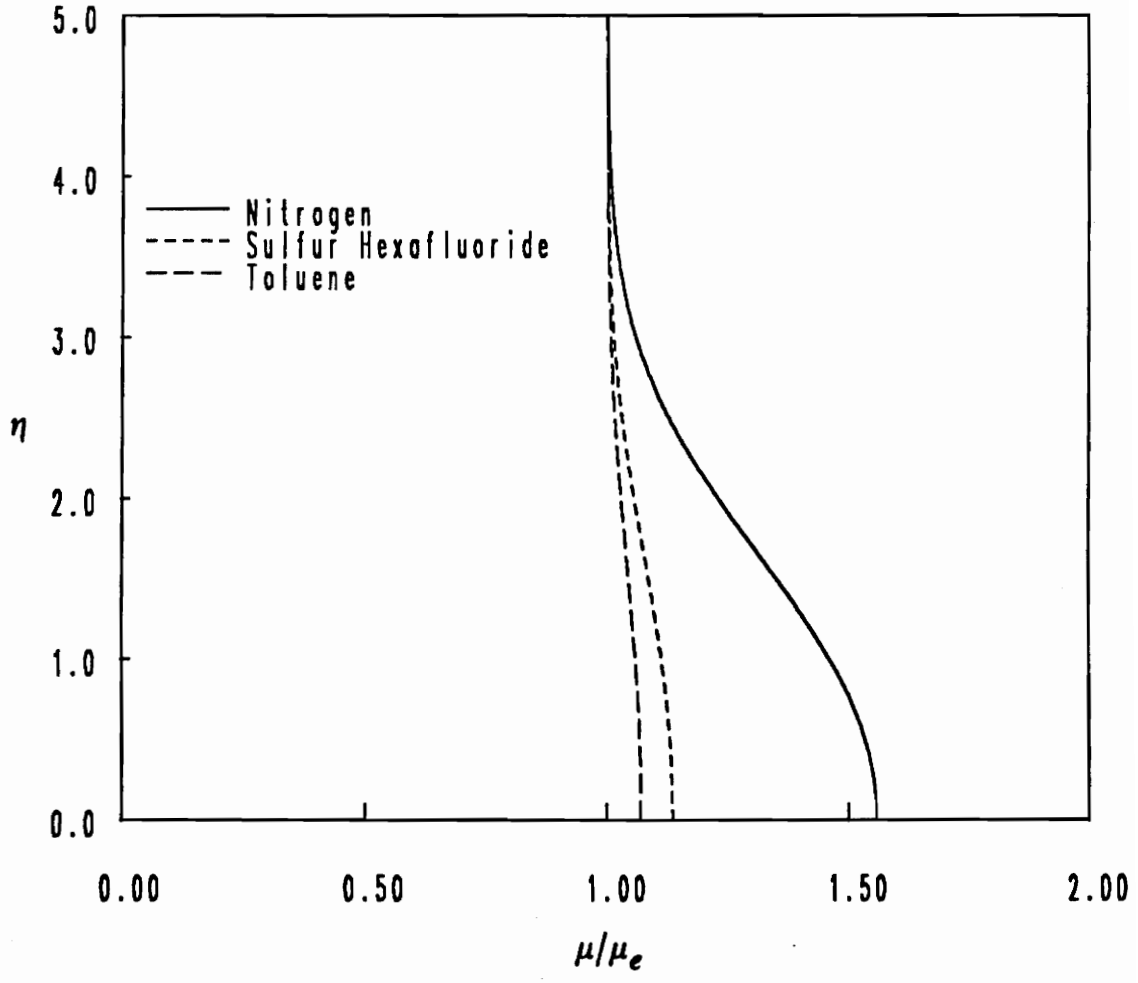

Figure 5.30. Plot of μ/μ_e vs. η for various fluids in a one-atmosphere flow: Illustrated are the results for a freestream Mach number of 2.0 and a freestream temperature of $1.01*T_c$. The freestream volumes for the one-atmosphere flows of nitrogen, sulfur hexafluoride, and toluene are $115*v_c$, $133*v_c$, and $156*v_c$, respectively.

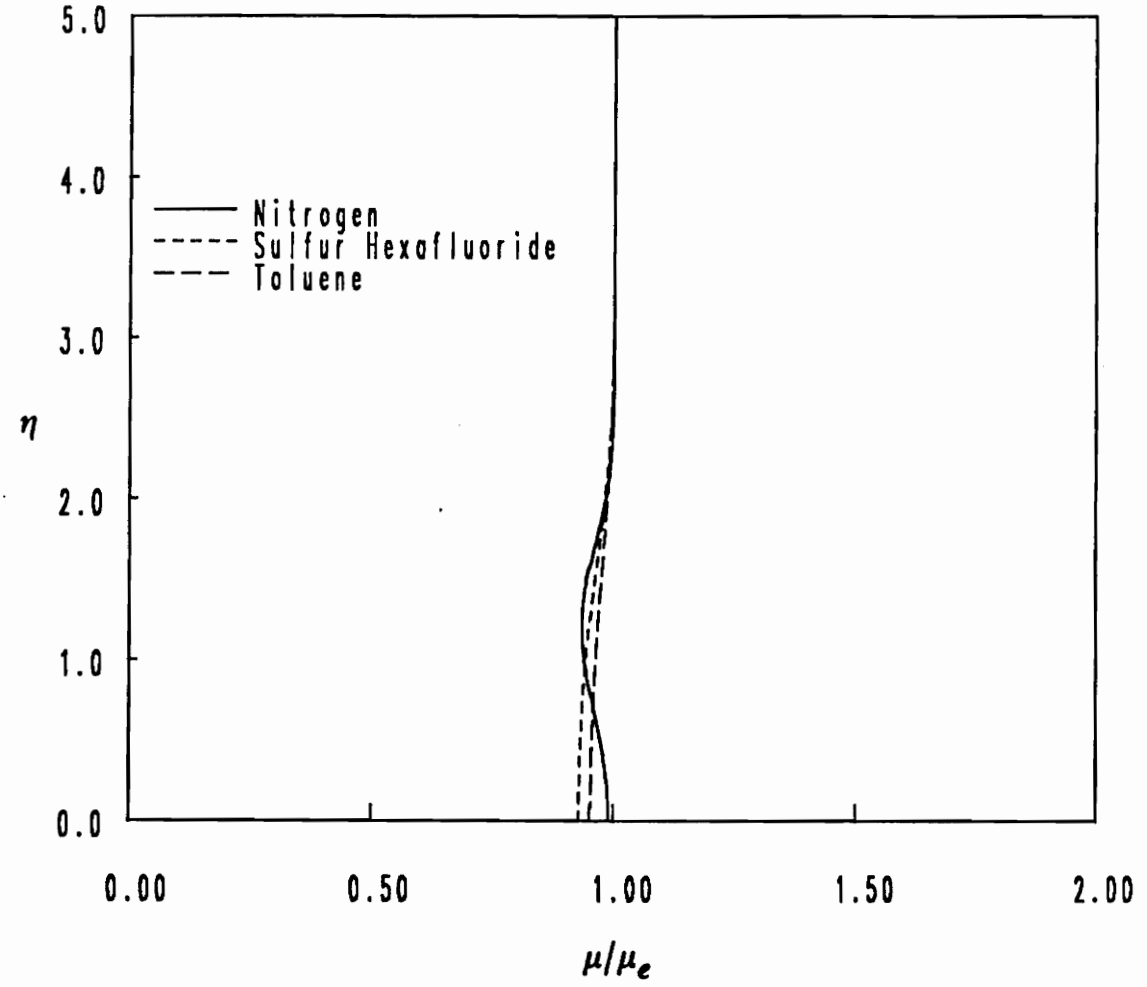

Figure 5.31. Plot of μ/μ_e vs. η for various fluids in a dense-gas flow: Illustrated are the results for a freestream Mach number of 2.0 and a freestream temperature of $1.01*T_c$.

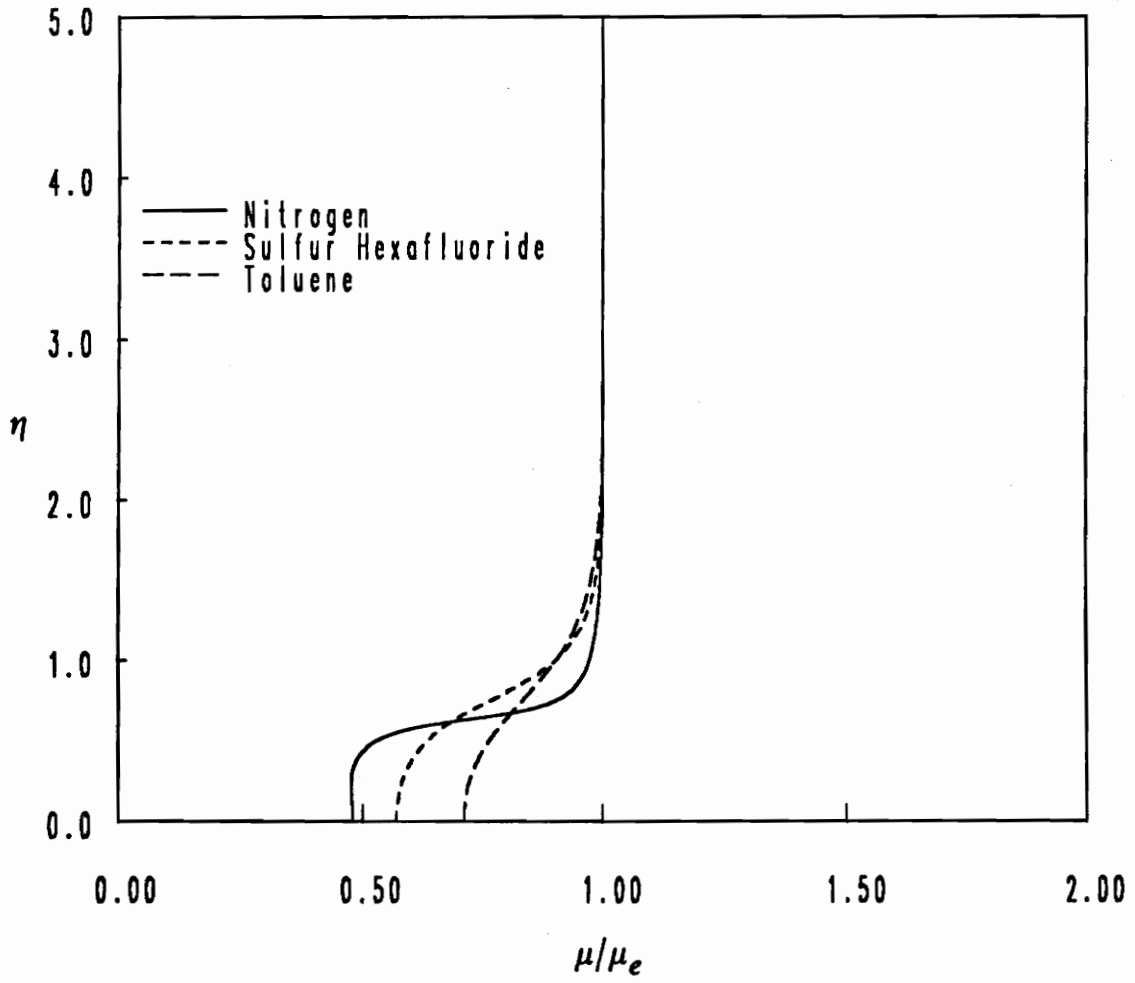

Figure 5.32. Plot of μ/μ_e vs. η for various fluids in a near-critical flow: Illustrated are the results for a freestream Mach number of 2.0 and a freestream temperature of $1.01*T_c$.

Comparison of Fluids: Global-Flow Variables

The impact of the weaker variations in the local-flow variables on the global-flow parameters is illustrated here. The trend toward a quasi-Blasius flow, such as that observed in the case having a freestream Mach number of 2.0, is also apparent over a wide range of freestream Mach numbers.

An inspection of Figures 5.33 - 5.38, which illustrate the variation of the wall density ratio and the ℓ_w parameter with Mach number, suggests that the variations in density and viscosity over a wide range of Mach numbers are dramatically decreased as a consequence of the increase in the specific heat. The result is an increase in the value of the skin-friction coefficient for the fluids having the larger values of the specific heat. Figures 5.39 - 5.41, which show the variation with Mach number of the computed skin-friction coefficient relative to the Blasius skin friction, indicate that even the near-critical flows, which typically display the most extreme variation in flow parameters such as the skin friction, exhibit noticeably less variation of the skin-friction coefficient with Mach number. Consequently, the fluids having larger values of the specific heat are expected to exhibit less tendency toward separation than lower specific-heat fluids.

The suppression of the variation of the Prandtl number observed in the case having a freestream Mach number of 2.0 is also observed over a wide range of Mach numbers. The variation with Mach number of the wall Prandtl-number ratio for the various freestream thermodynamic states, depicted in Figures 5.42 - 5.44, confirms this assertion. The fact that the ℓ_w parameter and the Prandtl number exhibit less variation also results in a recovery-factor ratio which approaches a constant value throughout the freestream Mach-number ranges as shown in Figures 5.45 - 5.47.

Note that the near-critical scaled recovery factors, shown in Figure 5.47, do not tend toward a value of one in the incompressible limit. As in the case of the near-critical recovery-factor ratio for nitrogen displayed in Figure 5.13, one reason for this behavior is due to the error inherent in Equation (4.6) in approximating the actual $b(Pr)$ function. Another reason for the scaled recovery factors not approaching a value of one in the zero Mach-number limit is the influence of numerical truncation errors. For the large specific-heat fluids, the temperature variation through the boundary

layer in the near-critical cases is virtually isothermal for freestream Mach numbers as large as 0.75. Consequently, in the zero Mach-number limit, the temperature differences needed for the recovery-factor ratios are well beyond the limit of the accuracy of the numerical scheme employed here. A computational grid with roughly twenty-five times the resolution used here would be required to accurately resolve the behavior of the recovery factor in the zero Mach-number limit for the higher specific-heat fluids.

A plot of the near-critical recovery factors for the various fluids scaled to the actual value of $b(Pr)$ obtained from Schlichting's graphical results is supplied in Figure 5.48. The recovery factors scaled to the correct values of $b(Pr)$ are seen to approach the value of one in the zero Mach-number limit, although they never reach the theoretical value due to the numerical truncation errors mentioned above.

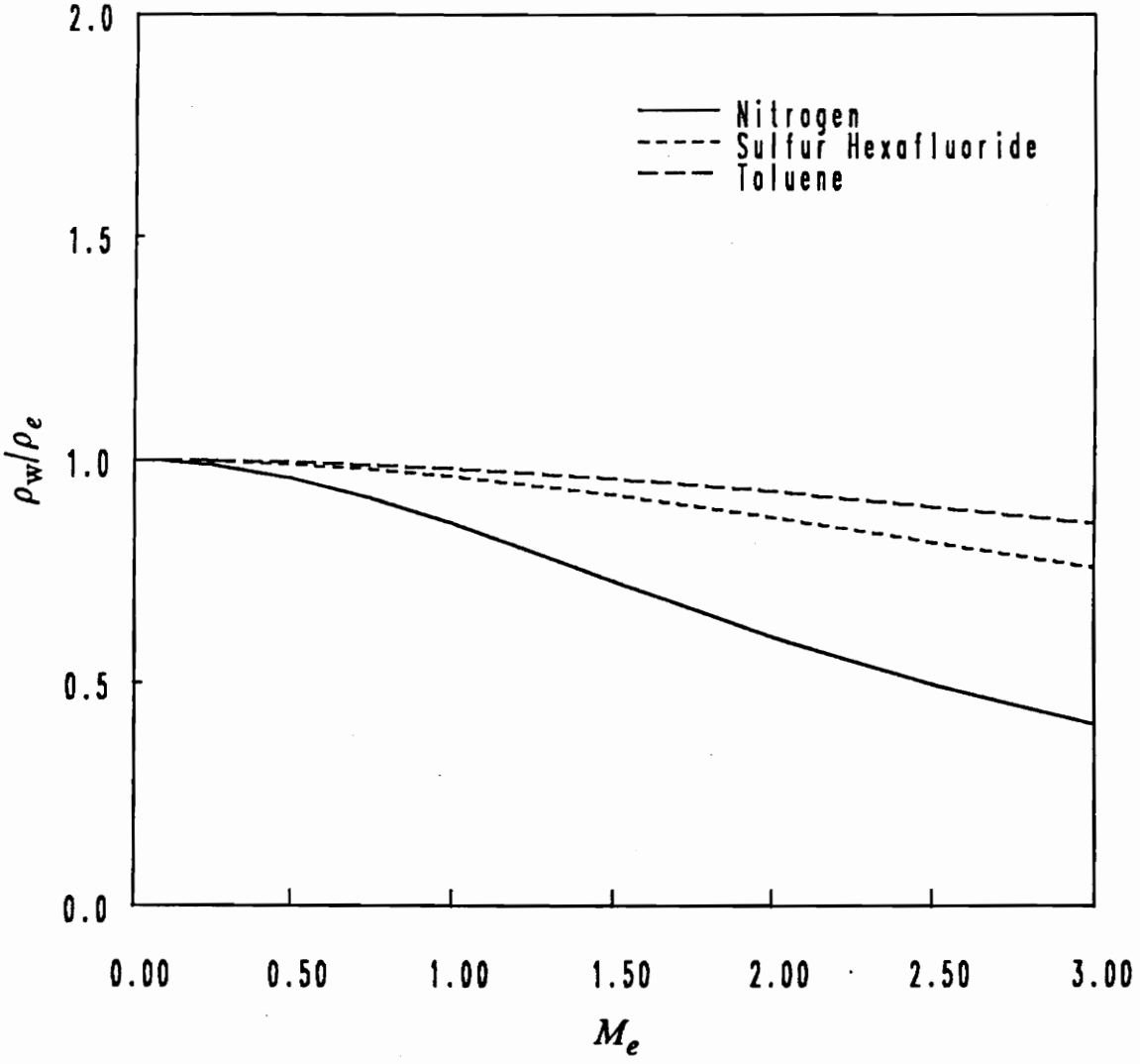

Figure 5.33. Plot of ρ_w/ρ_e vs. M_e for various fluids in a one-atmosphere flow: Illustrated are the results for a freestream Mach number of 2.0 and a freestream temperature of $1.01*T_c$. The freestream volumes for the one-atmosphere flows of nitrogen, sulfur hexafluoride, and toluene are $115*v_c$, $133*v_c$, and $156*v_c$, respectively.

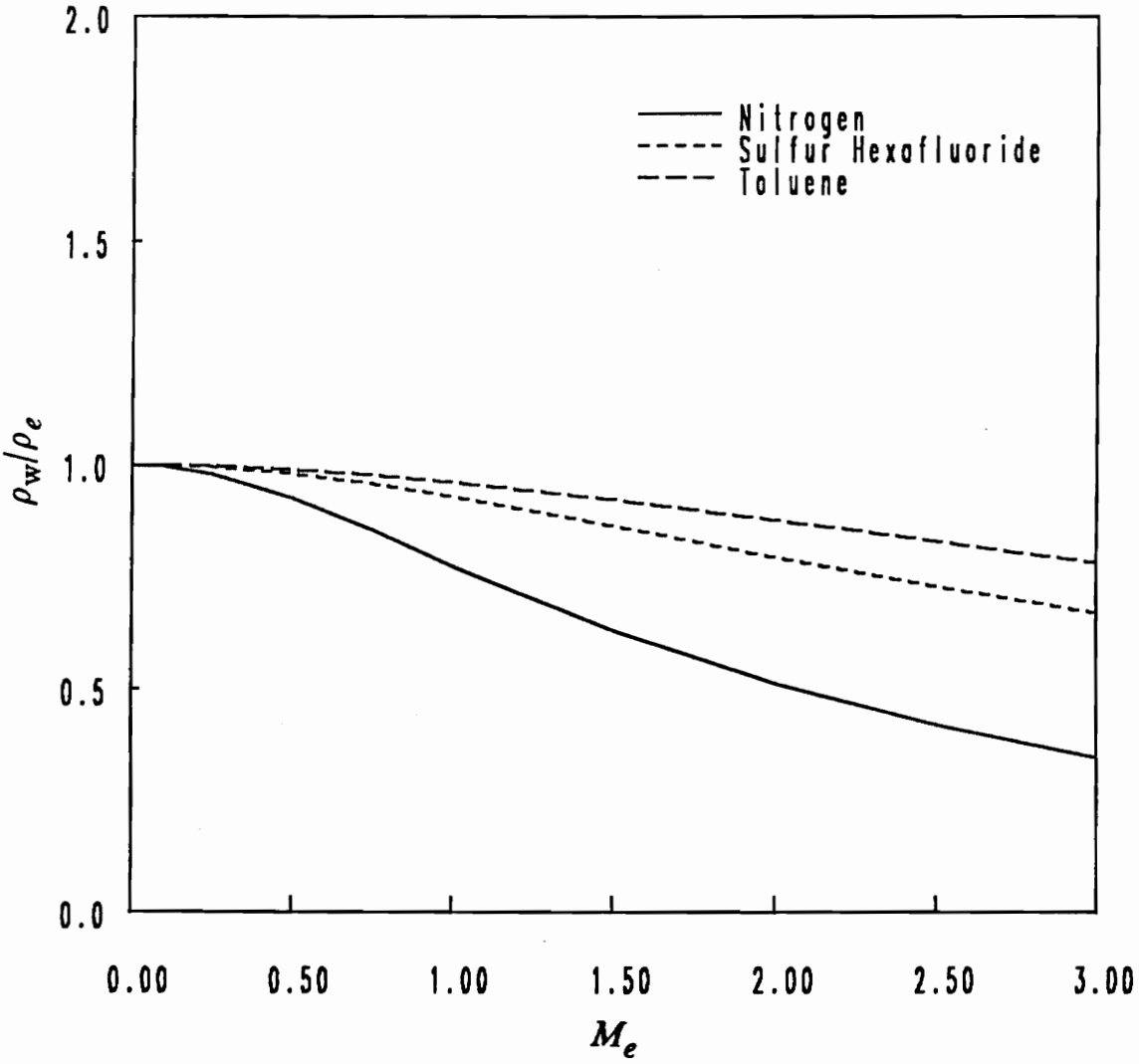

Figure 5.34. Plot of ρ_w/ρ_e vs. M_e for various fluids in a dense-gas flow: Illustrated are the results for a freestream Mach number of 2.0 and a freestream temperature of $1.01*T_c$.

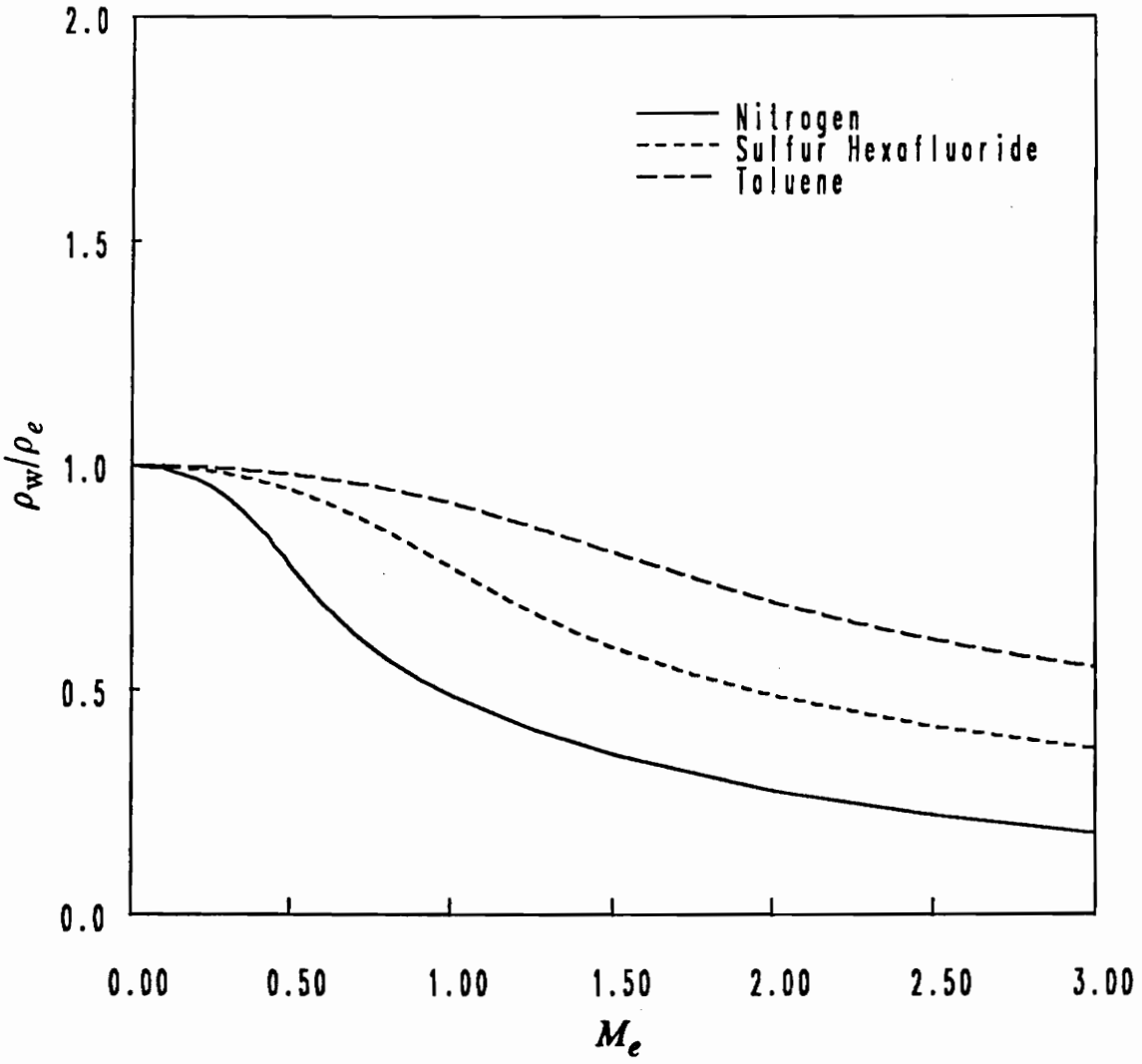

Figure 5.35. Plot of ρ_w/ρ_e vs. M_e for various fluids in a near-critical flow: Illustrated are the results for a freestream Mach number of 2.0 and a freestream temperature of $1.01*T_c$.

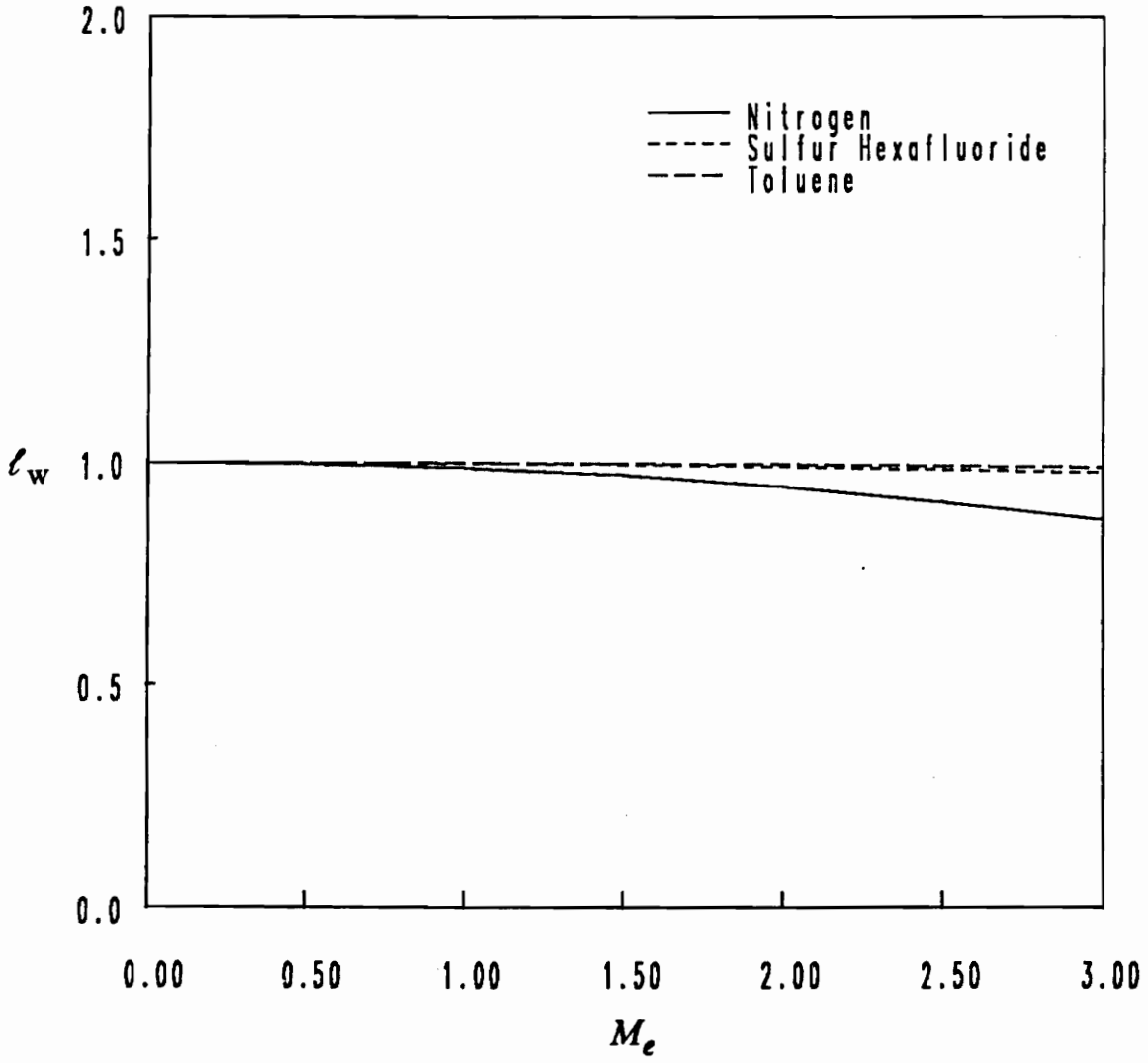

Figure 5.36. Plot of ℓ_w vs. M_e for various fluids in a one-atmosphere flow: Illustrated are the results for a freestream Mach number of 2.0 and a freestream temperature of $1.01*T_c$. The freestream volumes for the one-atmosphere flows of nitrogen, sulfur hexafluoride, and toluene are $115*v_c$, $133*v_c$, and $156*v_c$, respectively.

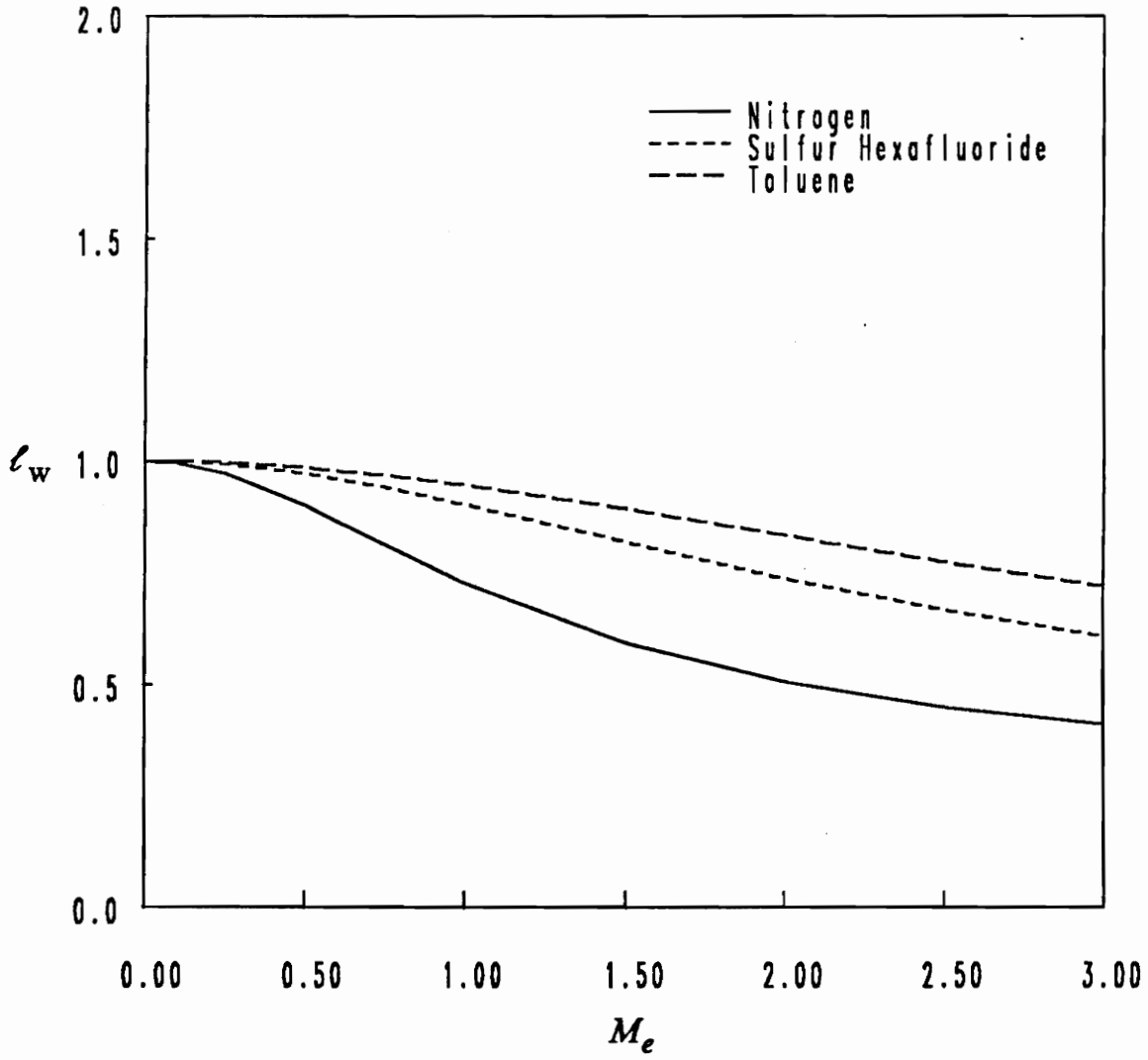

Figure 5.37. Plot of ℓ_w vs. M_e for various fluids in a dense-gas flow: Illustrated are the results for a freestream Mach number of 2.0 and a freestream temperature of $1.01*T_c$.

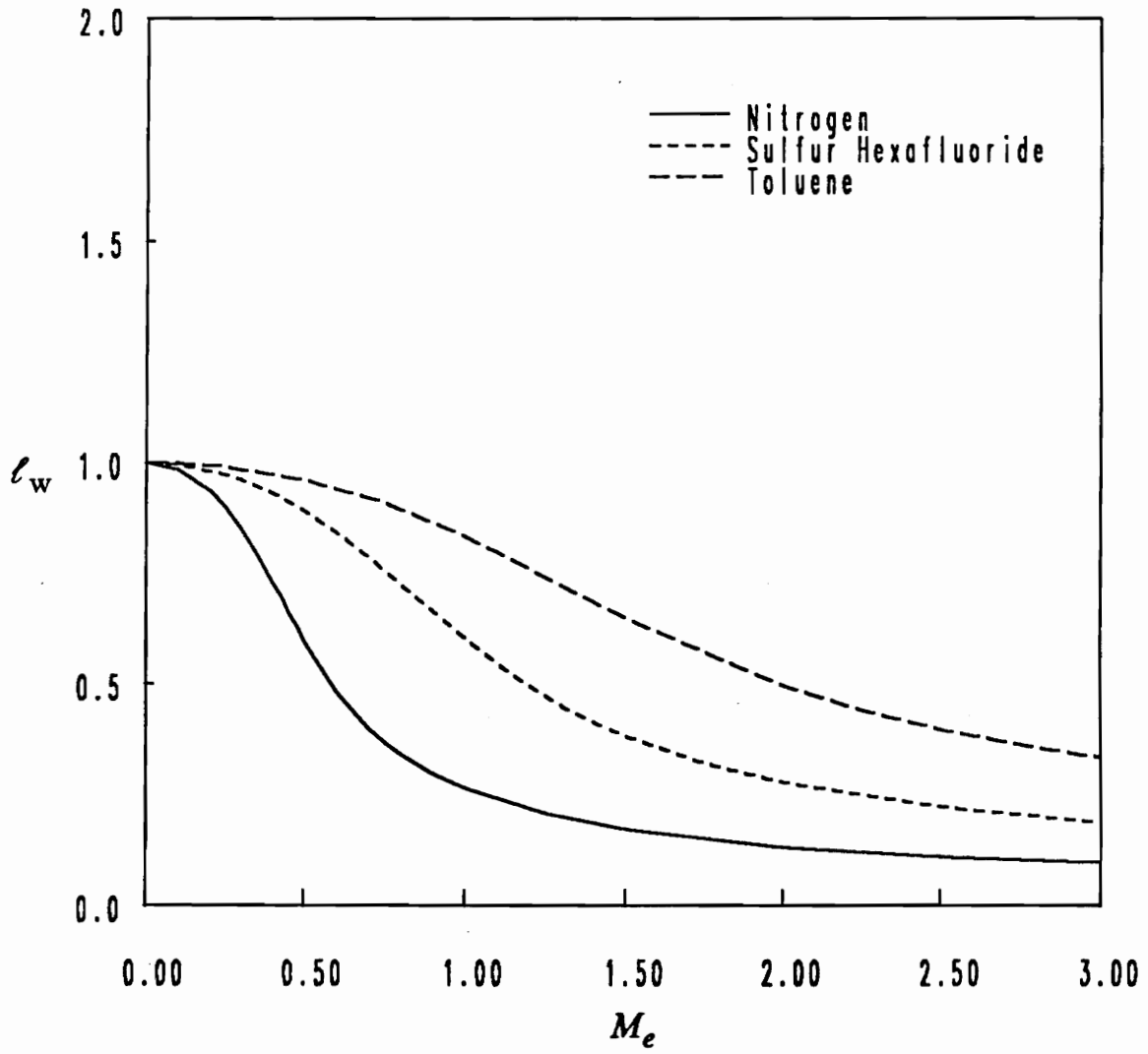

Figure 5.38. Plot of ℓ_w vs. M_e for various fluids in a near-critical flow: Illustrated are the results for a freestream Mach number of 2.0 and a freestream temperature of $1.01 * T_c$.

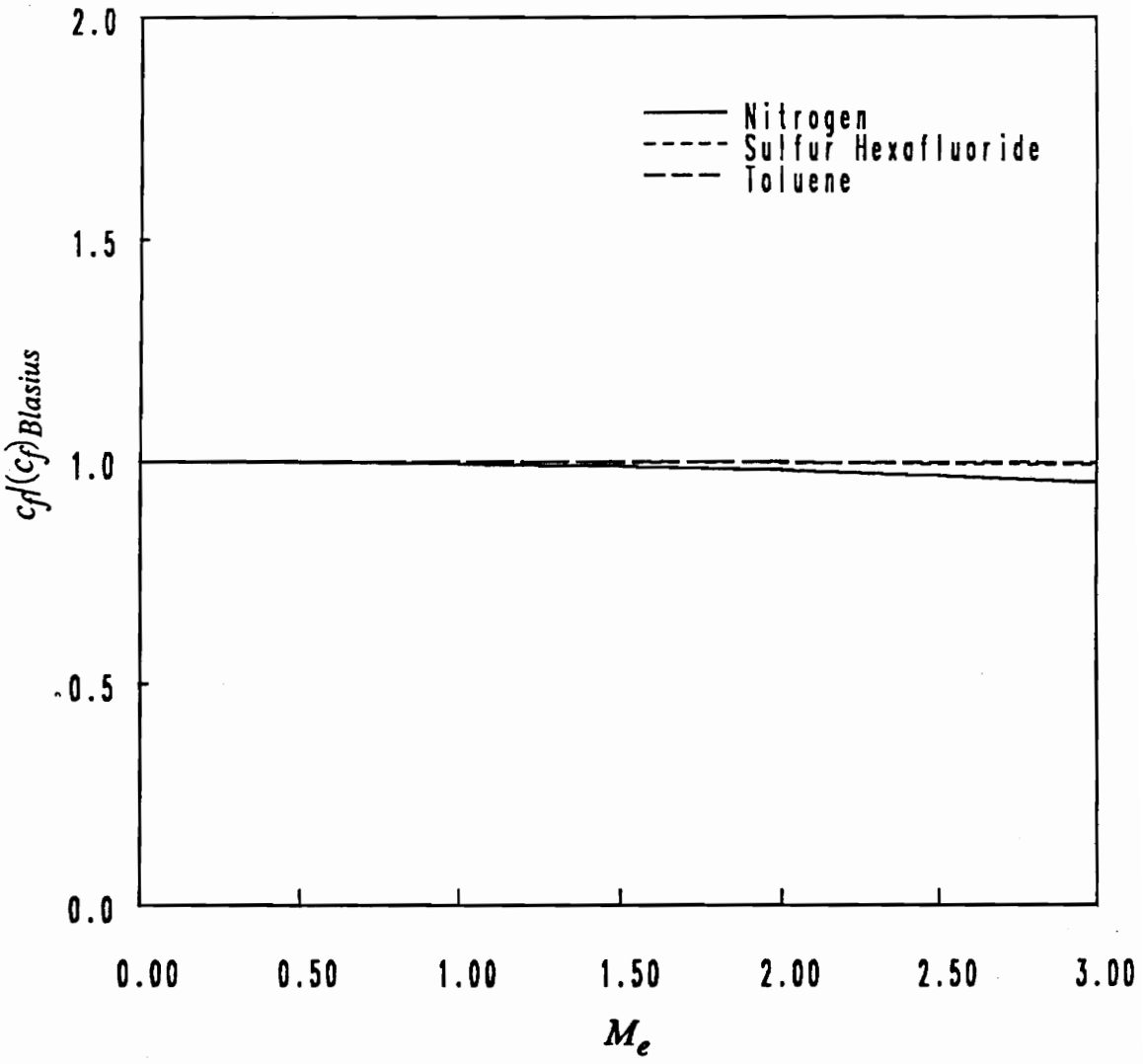

Figure 5.39. Plot of $c_f/(c_f)_{Blasius}$ vs. M_e for various fluids in a one-atmosphere flow: Illustrated are the results for a freestream Mach number of 2.0 and a freestream temperature of $1.01*T_c$. The freestream volumes for the one-atmosphere flows of nitrogen, sulfur hexafluoride, and toluene are $115*v_c$, $133*v_c$, and $156*v_c$, respectively.

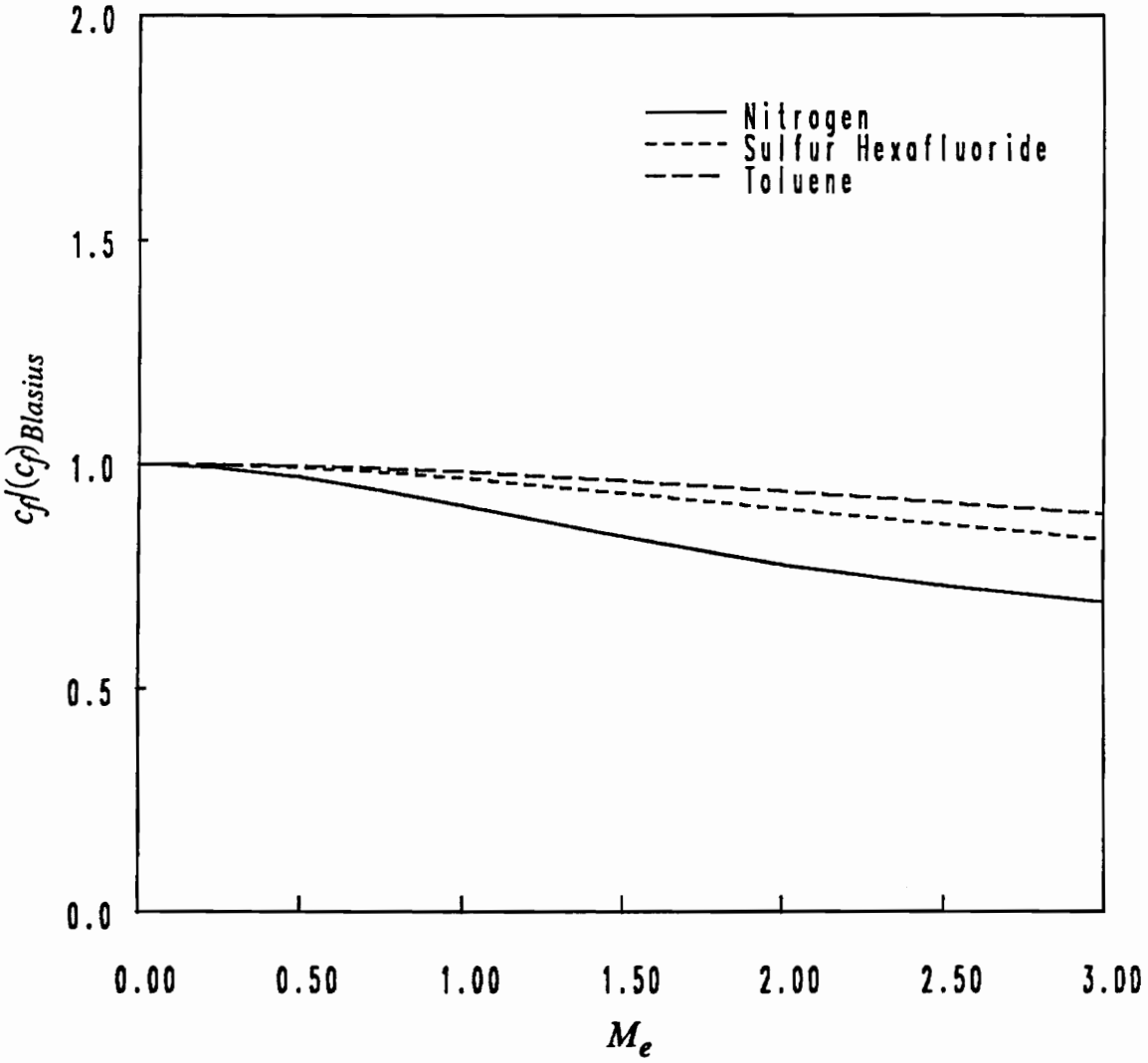

Figure 5.40. Plot of $c_f/(c_f)_{Blasius}$ vs. M_e for various fluids in a dense-gas flow: Illustrated are the results for a freestream Mach number of 2.0 and a freestream temperature of $1.01 * T_c$.

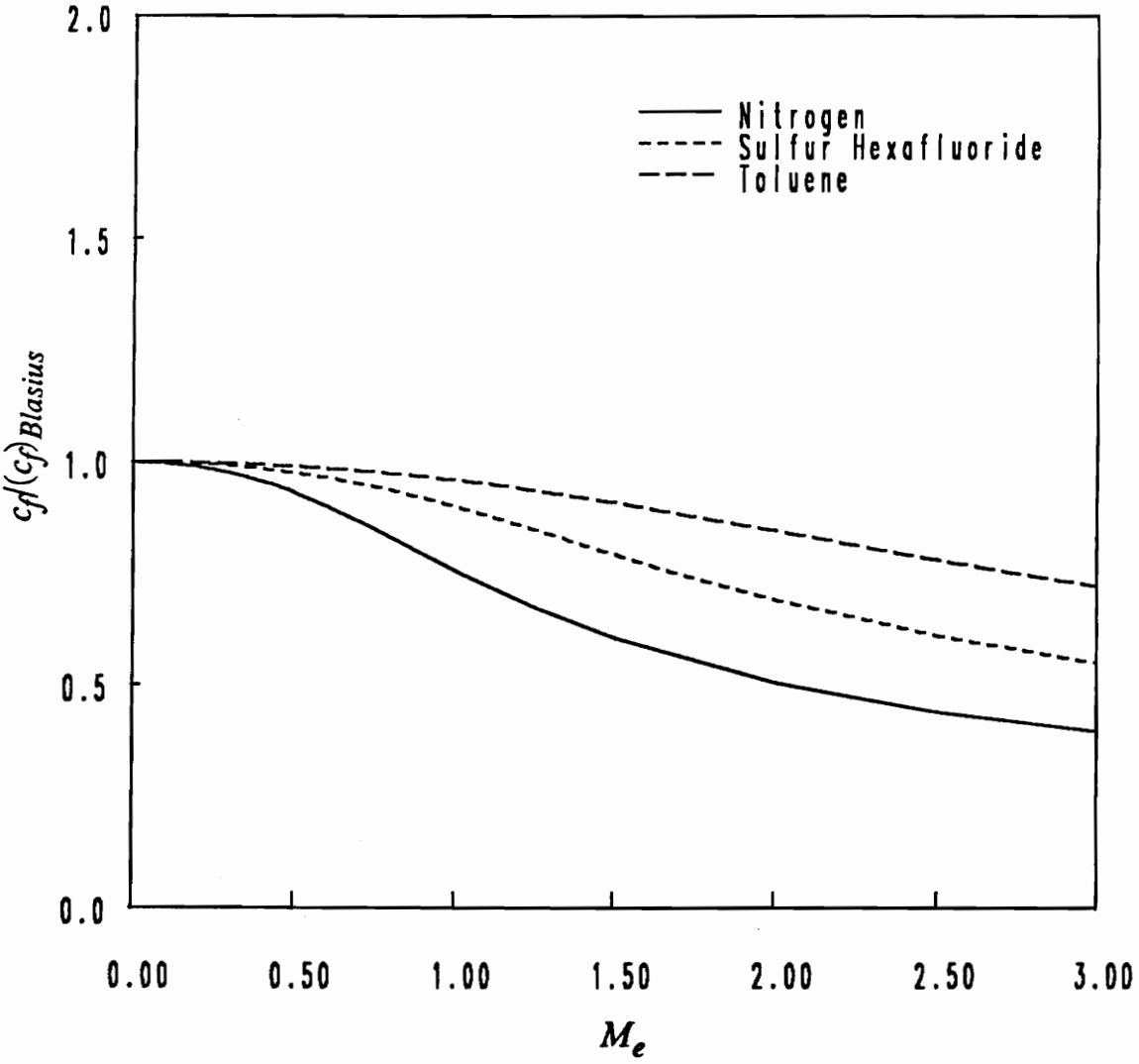

Figure 5.41. Plot of $c_f/(c_f)_{Blasius}$ vs. M_e for various fluids in a near-critical flow: Illustrated are the results for a freestream Mach number of 2.0 and a freestream temperature of $1.01*T_c$.

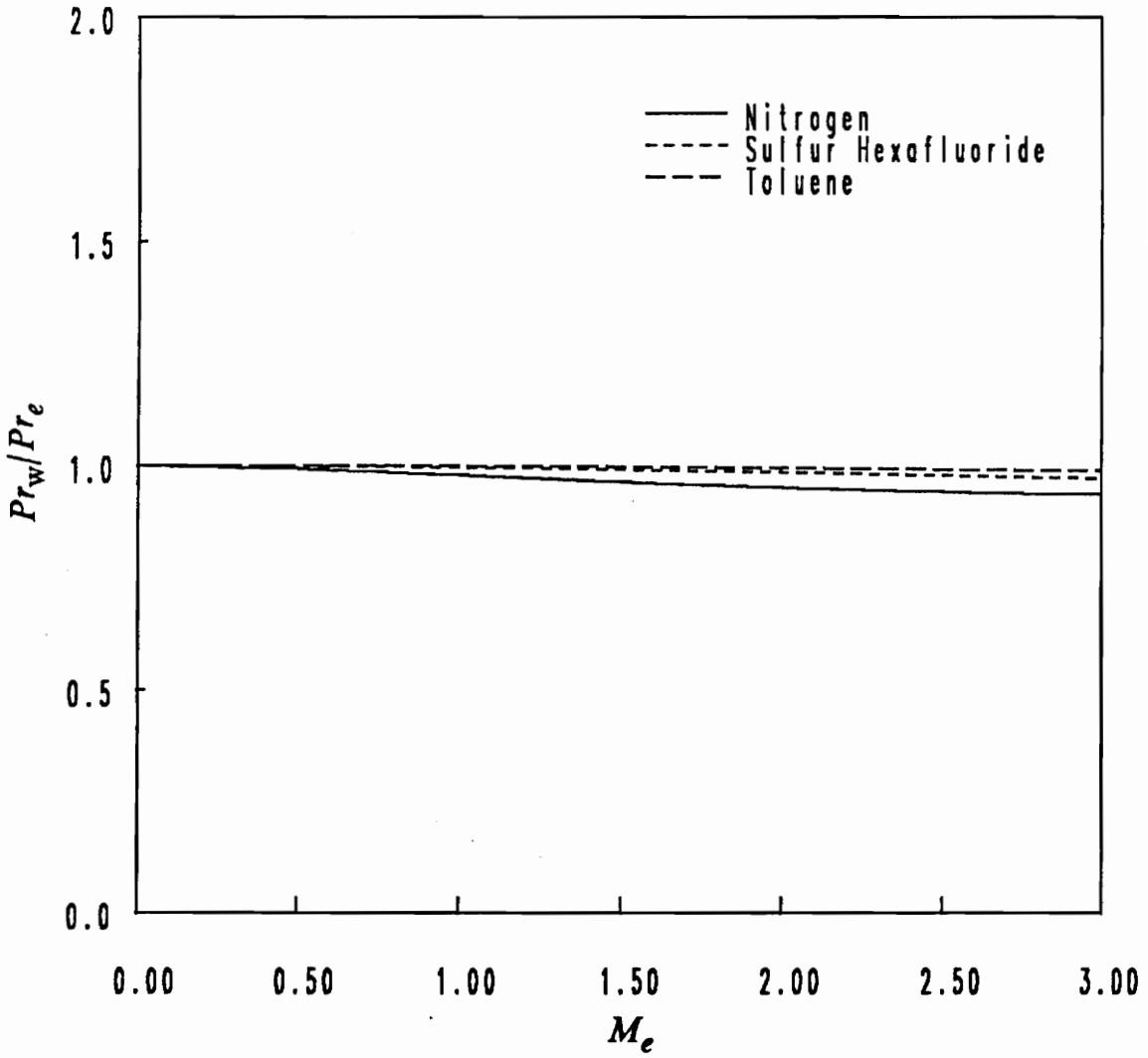

Figure 5.42. Plot of Pr_w/Pr_e vs. M_e for various fluids in a one-atmosphere flow: Illustrated are the results for a freestream Mach number of 2.0 and a freestream temperature of $1.01*T_c$. The freestream volumes for the one-atmosphere flows of nitrogen, sulfur hexafluoride, and toluene are $115*v_c$, $133*v_c$, and $156*v_c$, respectively.

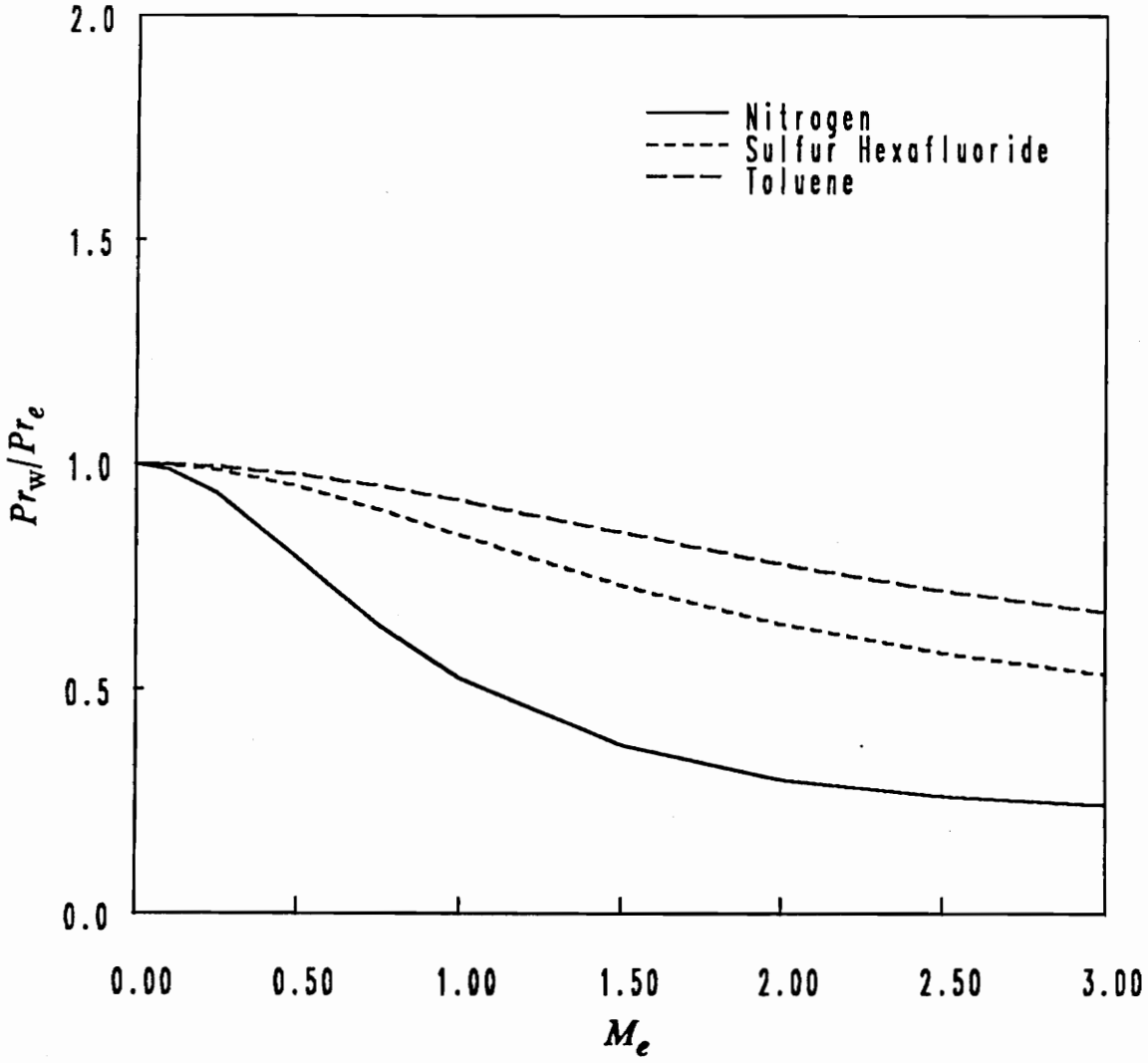

Figure 5.43. Plot of Pr_w/Pr_e vs. M_e for various fluids in a dense-gas flow: Illustrated are the results for a freestream Mach number of 2.0 and a freestream temperature of $1.01*T_c$.

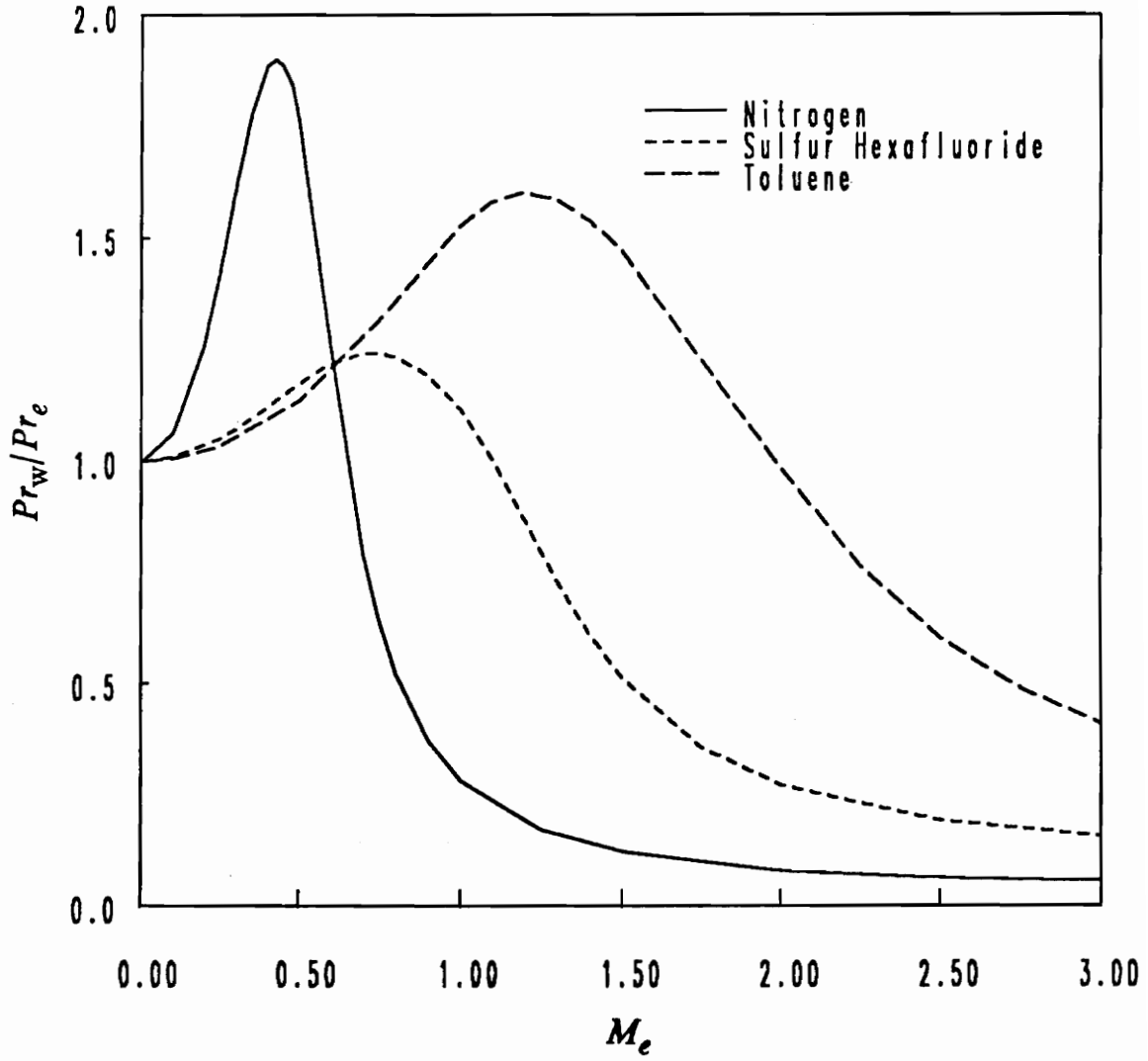

Figure 5.44. Plot of Pr_w/Pr_e vs. M_e for various fluids in a near-critical flow: Illustrated are the results for a freestream Mach number of 2.0 and a freestream temperature of $1.01*T_c$.

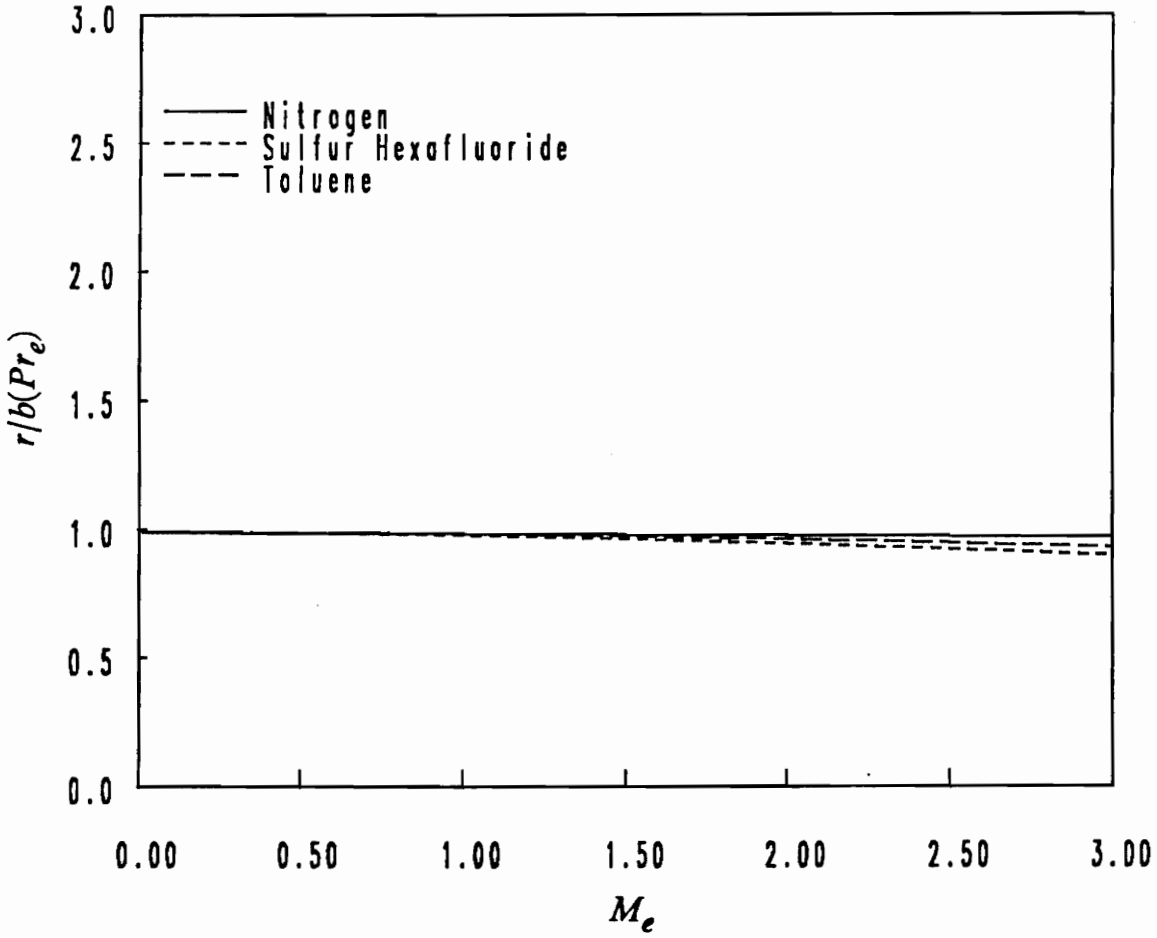

Figure 5.45. **Plot of $r/b(Pr_e)$ vs. M_e for various fluids in a one-atmosphere flow:** Illustrated are the results for a freestream Mach number of 2.0 and a freestream temperature of $1.01*T_c$. The freestream volumes for the one-atmosphere flows of nitrogen, sulfur hexafluoride, and toluene are $115*v_c$, $133*v_c$, and $156*v_c$, respectively.

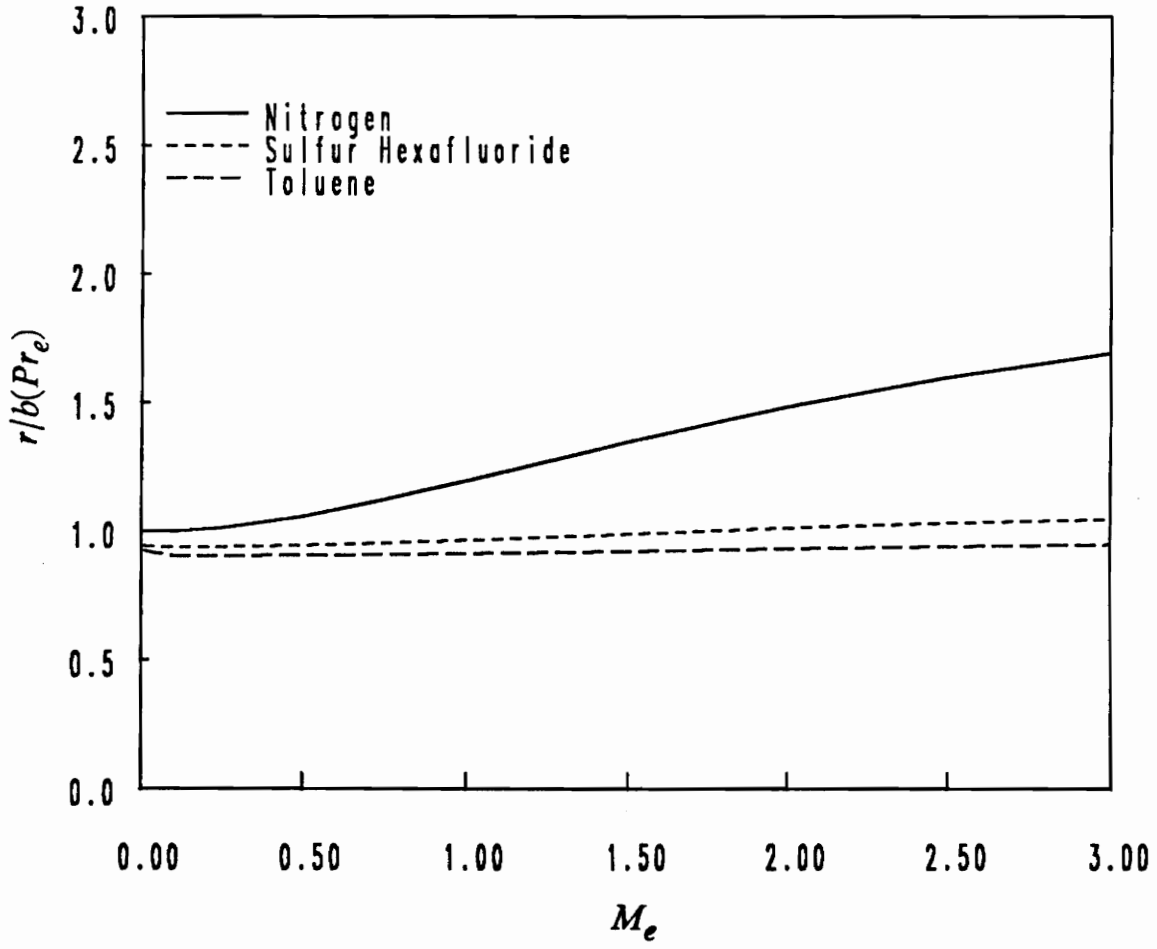

Figure 5.46. Plot of $r/b(Pr_e)$ vs. M_e for various fluids in a dense-gas flow: Illustrated are the results for a freestream Mach number of 2.0 and a freestream temperature of $1.01*T_c$.

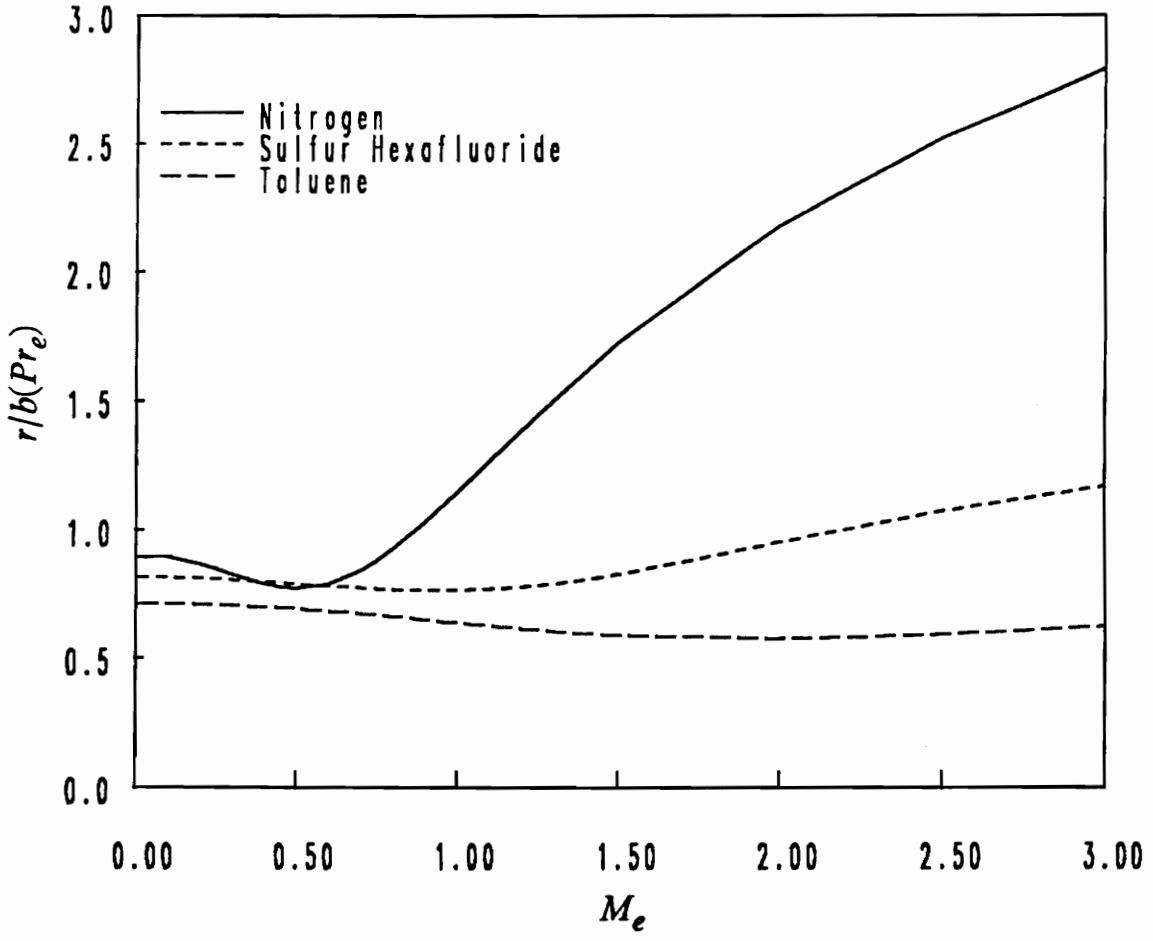

Figure 5.47. Plot of $r/b(Pr_e)$ vs. M_e for various fluids in a near-critical flow: Illustrated are the results for a freestream Mach number of 2.0 and a freestream temperature of $1.01 * T_c$.

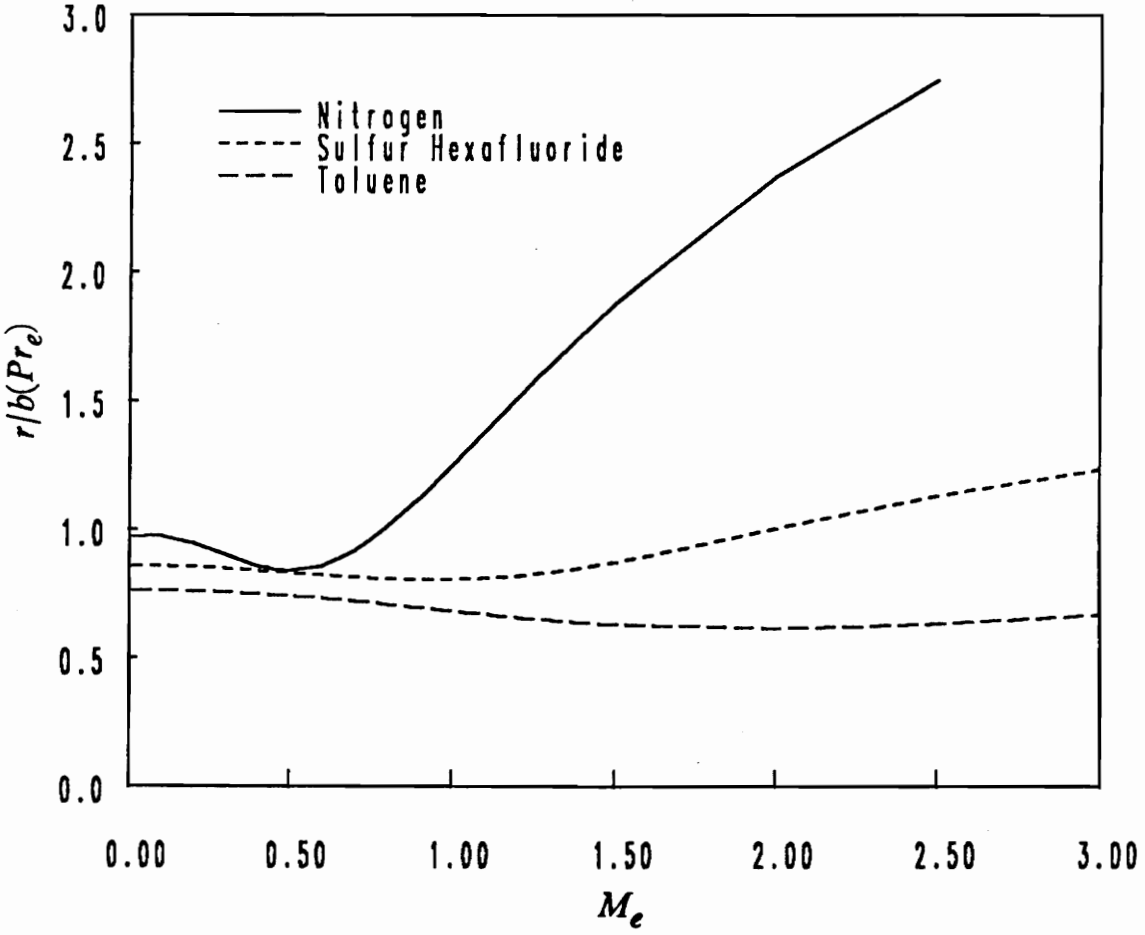

Figure 5.48. Plot of $r/b(Pr_e)$ vs. M_e for various fluids using the actual $b(Pr_e)$, near-critical case: Illustrated are the results for a freestream temperature of $1.01*T_c$. The one-atmosphere case corresponds to a freestream volume of $115*v_c$.

Conclusions

The mean-flow results for the flow of nitrogen over a flat plate with an adiabatic wall indicate a number of deviations from the standard ideal-gas boundary-layer flows once the commonly used ideal-gas constraints are relaxed. Among the deviations found is the potential for nonnegligible variation of flow parameters such as the specific heat and the Prandtl number. Such variation is particularly pronounced when the freestream conditions are in the neighborhood of the thermodynamic critical point. Furthermore, an examination of flows throughout the entire single-phase vapor regime reveals non-classical viscosity and thermal-conductivity behavior due to the dependence of the fluid material properties on density as well as temperature.

The strong local variations observed give rise to corresponding variations in global parameters such as the skin friction and the recovery factor. In the dense-gas and near-critical regimes, the skin friction is seen to be considerably smaller than that for ideal-gas flows. This decrease is attributed to the strong local variation of ℓ in the boundary layer. As discussed earlier in this chapter, it is expected that dense gases are therefore more susceptible to separation than their ideal-gas counterparts.

The strong variations in the recovery factor are expected to be primarily due to the strong local variations of the Prandtl number. The classical estimates of the recovery factor given by Equation (4.6) are seen to significantly underpredict the actual value of r, at least in the specific cases considered. It is consequently concluded that no simple extension of the estimates for r are possible when dense-gas effects are nonnegligible.

The comparison of the flows of nitrogen, sulfur hexafluoride, and toluene over a flat plate with an adiabatic wall illustrates the influence of the specific heat on the boundary-layer flows. The most important impact of increasing the specific heat on a boundary-layer flow is the reduction in the strength of the viscous dissipation which leads to a decrease in the temperature variation, and hence the variation of all the flow parameters, throughout the boundary layer. Even the rapid variation of the flow parameters characteristic of the near-critical flows is minimized by an increase in the

specific heat. Because of the decrease in the variation of the flow parameters, large specific-heat fluids exhibit larger values of the skin-friction coefficient and therefore less tendency toward separation than fluids with smaller specific-heat values. Thus, the increased susceptibility toward separation observed in the dense-gas and near-critical flows of nitrogen can be partially offset by the substitution of fluids with larger specific heats. Another consequence of the decrease in the variation of the flow parameters due to the effects of increasing specific heat is the trend toward quasi-Blasius flow. This trend is observed in spite of the non-classical behavior of the dense-gas and near-critical flows.

Chapter 6

Mean-Flow Results: Heated and Cooled Walls

The results for the flow of nitrogen over heated and cooled walls at various freestream thermodynamic states are presented in this chapter. The effects of heating and cooling of the flow on the global parameters, such as the skin-friction coefficient and the Nusselt number, are analyzed here. The temperature of the wall, T_w, in each case is measured relative to the temperature of the corresponding adiabatic wall, T_{adb}. Only flows over isothermal walls are considered.

For the near-critical and dense-gas flows, the degree of cooling considered is less than that employed in the one-atmosphere flows. In the near-critical case, the amount of cooling allowed is limited by the maximum-density restriction imposed on the equation of state. For the dense-gas case, the amount of cooling is limited by the two-phase region. For all of the cooled-wall results presented in this chapter, the curves corresponding to the near-critical and dense-gas flows are terminated at the respective limiting values. In contrast, the heated flows are not subject to any inherent restrictions.

The variations with freestream Mach number of ℓ_w, the scaled skin-friction coefficient, the wall Prandtl-number ratio, and the local Nusselt number for the one-atmosphere, dense-gas, and

near-critical flows are presented in Figures 6.1 - 6.12. The Nusselt number is scaled to the following expressions, which are based on the outer-edge Prandtl number as found in Schlichting (1979):

$$cb(Pr_e) = \begin{cases} 0.564\sqrt{Pr_e}\,\sqrt{Re_\xi} & \text{for } Pr_e \to 0 \\ 0.332 Pr_e^{1/3}\sqrt{Re_\xi} & \text{for } 0.6 < Pr_e < 10. \\ 0.339 Pr_e^{1/3}\sqrt{Re_\xi} & \text{for } Pr_e \to \infty \end{cases} \tag{6.1}$$

In each of the plots of ℓ_w, the skin-friction ratio, and the wall Prandtl-number ratio, the results for heated and cooled walls are presented relative to the adiabatic-wall results. Thus, the effects of heating and cooling on the global flow parameters are clearly illustrated.

The predominant influence of cooling of the wall for each of the three freestream thermodynamic states is an increase in the skin-friction coefficient. The increase in ℓ_w due to cooling of the wall is regarded as the source of the increase in the skin-friction coefficient. Predictions of triple-deck theory suggest that this rise in the skin-friction coefficient translates into a decrease in the susceptibility of the boundary layer to separation. The increase in the skin-friction coefficient in the dense-gas and near-critical boundary layers due to cooling of the wall is larger than the corresponding increase for the one-atmosphere flow. As a result, the greater susceptibility of the near-critical and dense-gas boundary layers to separation observed in Chapter 5 can be partially offset by cooling of the wall.

The rapid changes in the values of ℓ_w and the Prandtl number, seen in Figures 6.9 and 6.11, correspond to the freestream Mach numbers at which the conditions at the wall are closest to the thermodynamic critical point. At each of these freestream Mach numbers, the value of the Prandtl number at the wall is at its local maximum. In addition, the gradients at the wall for all the local-flow parameters are substantial. The resolution of the computational grid at the wall is inadequate to accurately capture the rapid changes encountered in the physical variables at the wall. As a result, Figure 6.10 exhibits what appear to be irregularities in the skin-friction coefficient; these irregularities are particularly noticeable at a Mach number of approximately 2.0 in the case having $T_w = 0.85^* T_{adb}$. Further resolution of the grid is expected to provide a better representation of the

variation of the skin-friction coefficient for the flows in which the wall conditions are in the immediate vicinity of the thermodynamic critical point.

In contrast to the effects of cooling of the wall, heating of the wall tends to lower the ℓ_w parameter and hence the value of the skin-friction coefficient for each of the three freestream thermodynamic states. Consequently, heating of the wall is expected to increase the susceptibility of the boundary-layer flows to separation.

Heating of the wall is seen to yield roughly constant values of ℓ_w, the skin-friction ratio, the Prandtl-number ratio, and the scaled Nusselt number throughout the range of freestream Mach numbers for each of the three freestream thermodynamic states. This behavior seems to suggest the existence of an ideal-gas wall region in the flow for each of the cases due to the approach of the wall density to the ideal-gas limit. This result is consistent with the findings of Chapter 5 in which the increase in the temperature associated with an increase of the freestream Mach number yielded an ideal-gas wall region in the near-critical flows.

The values of the heated- and cooled-wall Prandtl-number ratios are considerably less than one in the near-critical and dense-gas cases, thus indicating that the Prandtl number varies appreciably throughout the boundary layer. This is in marked contrast to the one-atmosphere flow in which the Prandtl number remains virtually constant throughout the boundary layer for the full range of freestream Mach numbers shown.

The magnitude of change in all the global parameters is largest in the near-critical flow. This result is consistent with the findings of Chapter 5 in which it was observed that very small changes in the temperature produced large changes in density and consequently large variations in the local flow parameters.

A consequence of the nonnegligible variation of properties, particularly the Prandtl number and ℓ_w, seen in the dense-gas and near-critical flows, is a breakdown of Equation (6.1) in accurately modeling the variation of the Nusselt number with freestream Mach number. For the dense-gas and near-critical flows, Equation (6.1) is seen to overpredict the Nusselt number. Consequently, predictions of the heat-transfer rate made using Equation (6.1) are likely to be incorrect when applied to flows with freestream conditions which are beyond the ideal-gas limit.

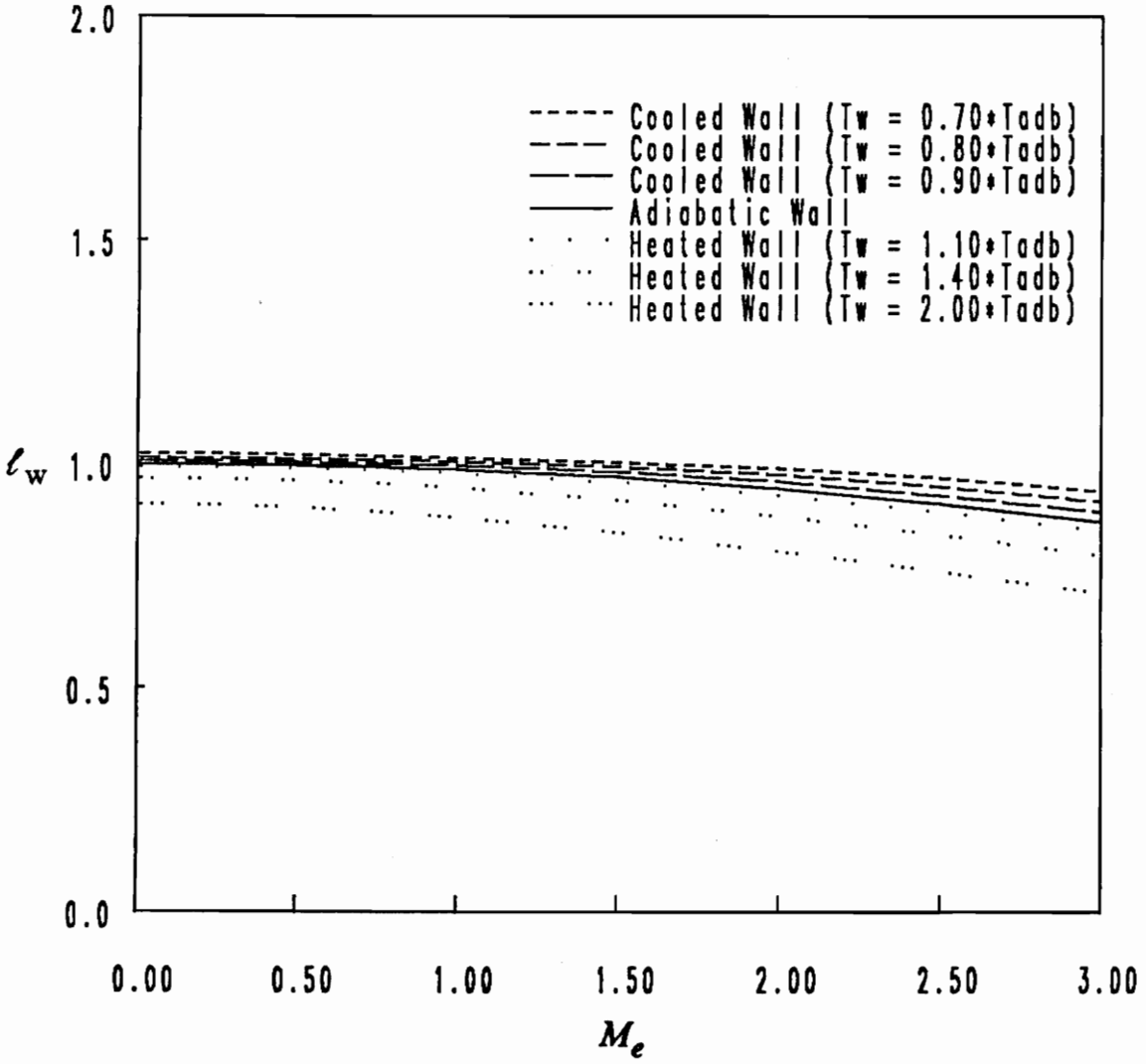

Figure 6.1. Plot of ℓ_w vs. M_e in a one-atmosphere flow: The one-atmosphere case corresponds to a freestream volume of $115*v_c$.

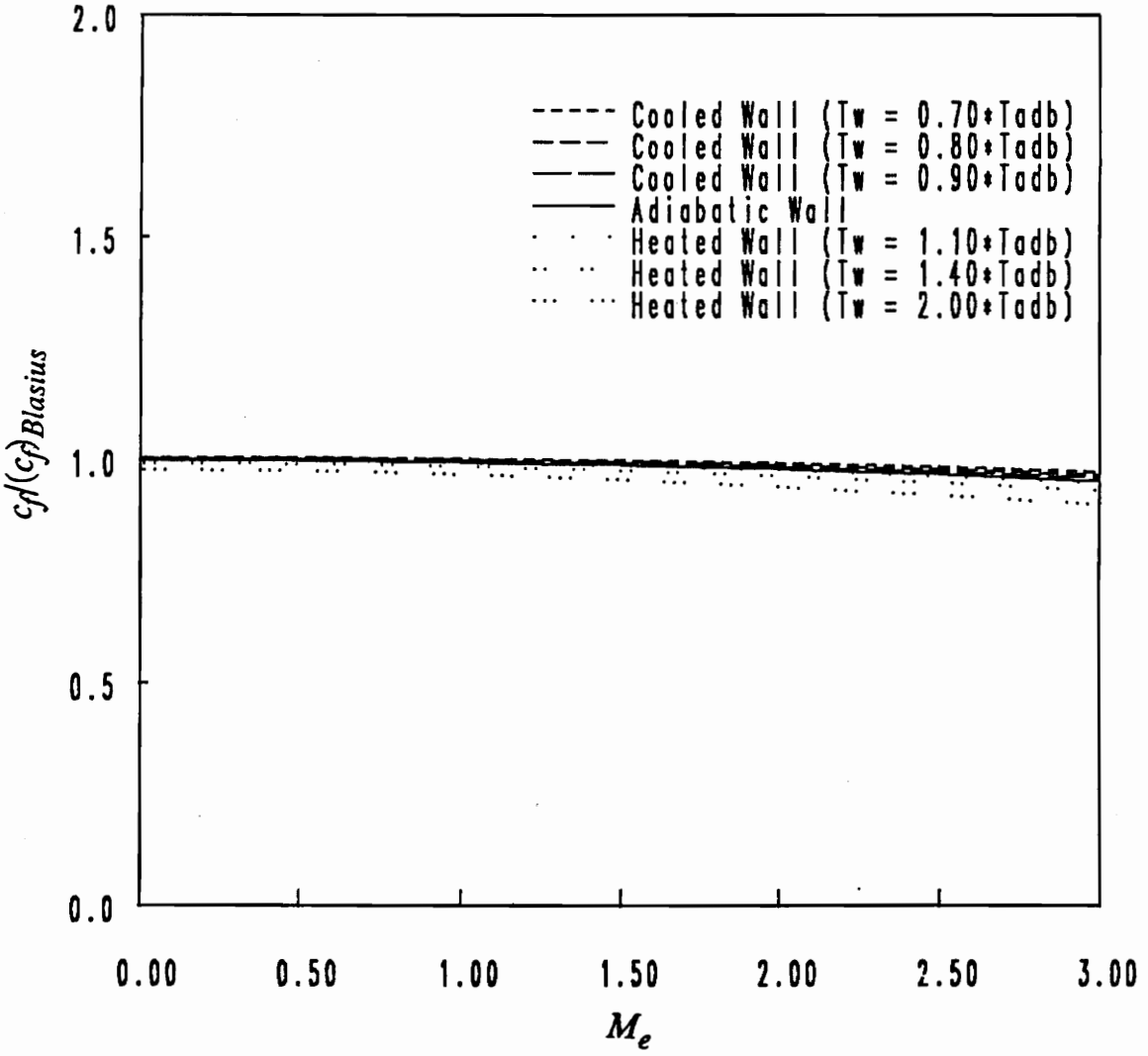

Figure 6.2. Plot of $c_f/(c_f)_{Blasius}$ vs. M_e in a one-atmosphere flow: The one-atmosphere case corresponds to a freestream volume of $115*v_c$.

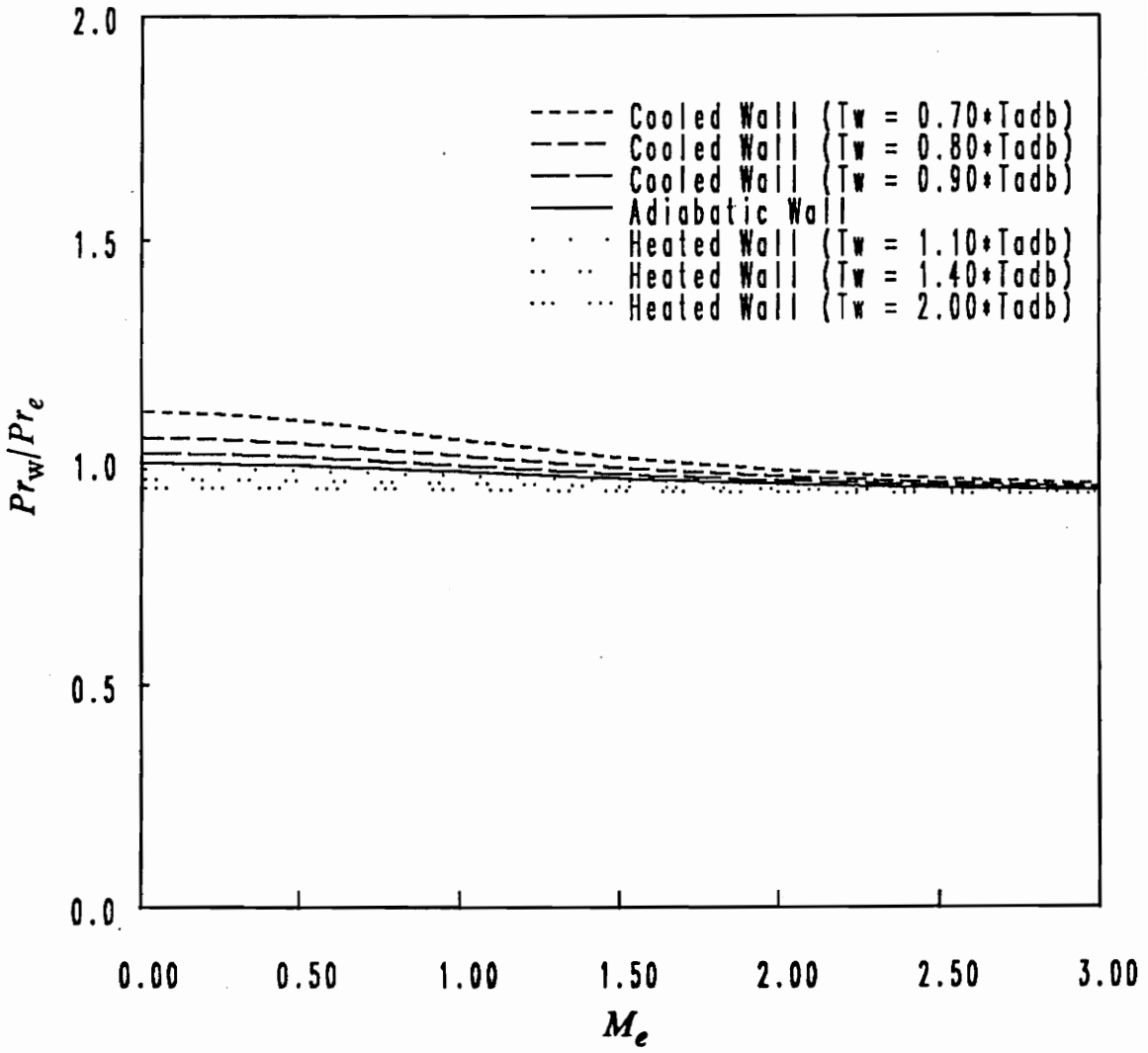

Figure 6.3. Plot of Pr_w/Pr_e vs. M_e in a one-atmosphere flow: The one-atmosphere case corresponds to a freestream volume of $115*v_c$.

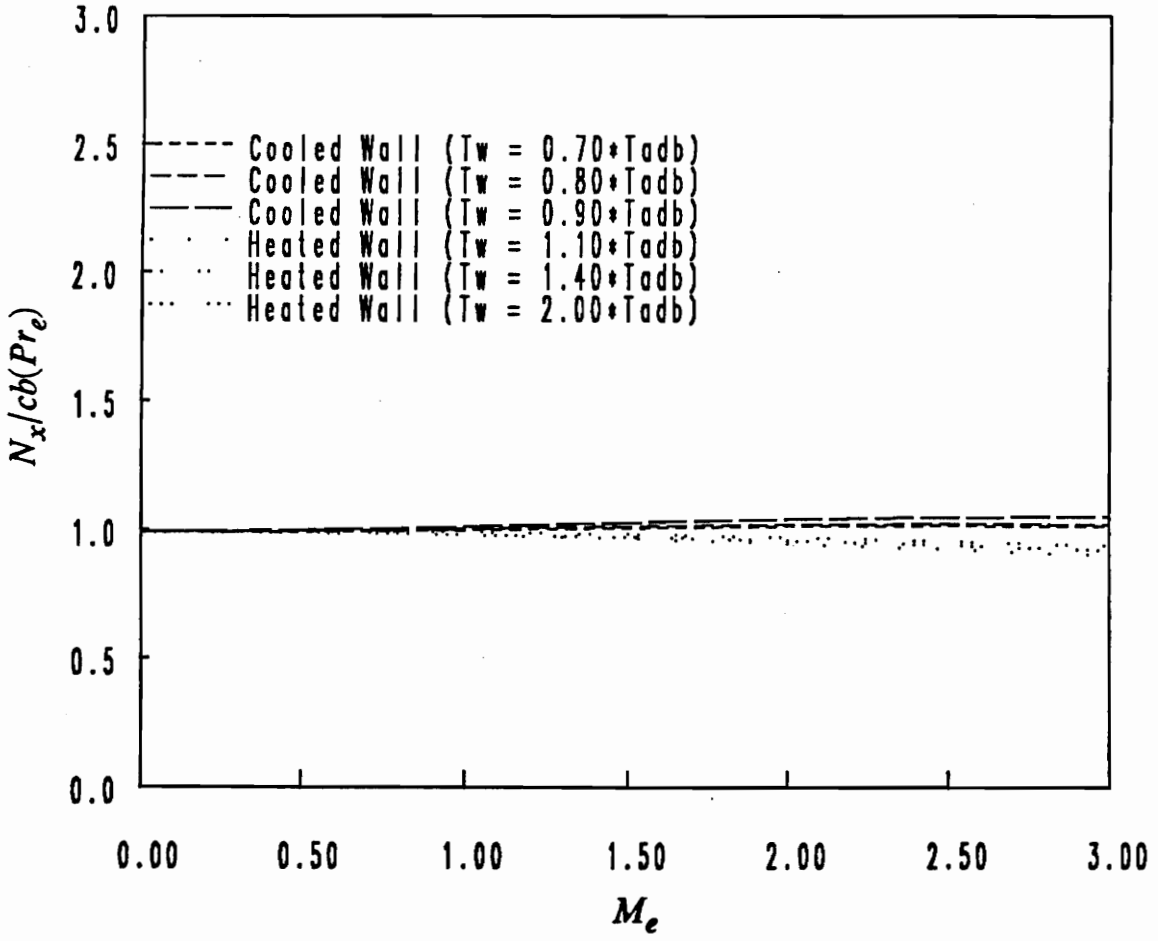

Figure 6.4. Plot of $N_x/cb(Pr_e)$ vs. M_e in a one-atmosphere flow: The one-atmosphere case corresponds to a freestream volume of 115^*v_c.

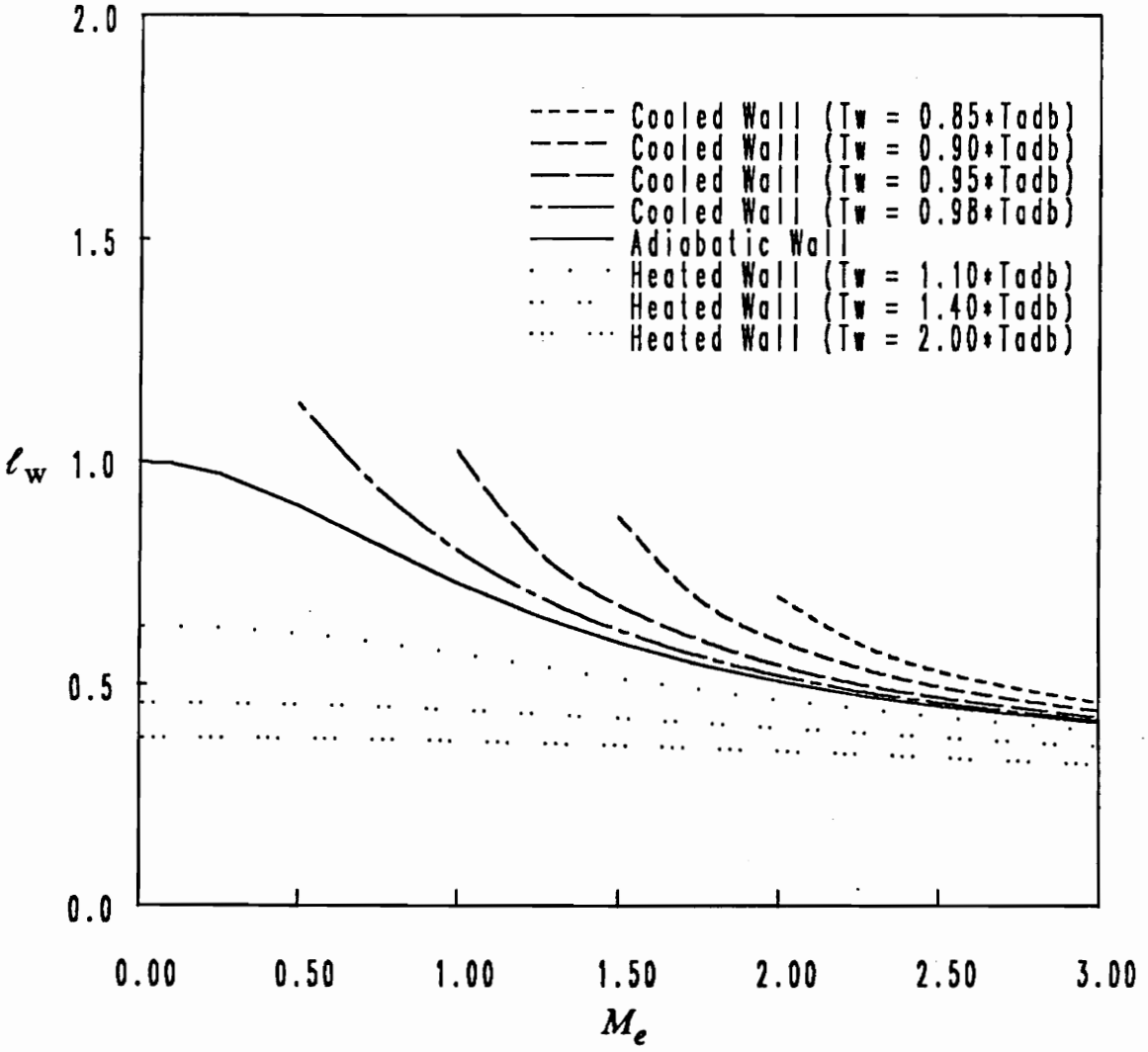

Figure 6.5. Plot of ℓ_w vs. M_e in a dense-gas flow

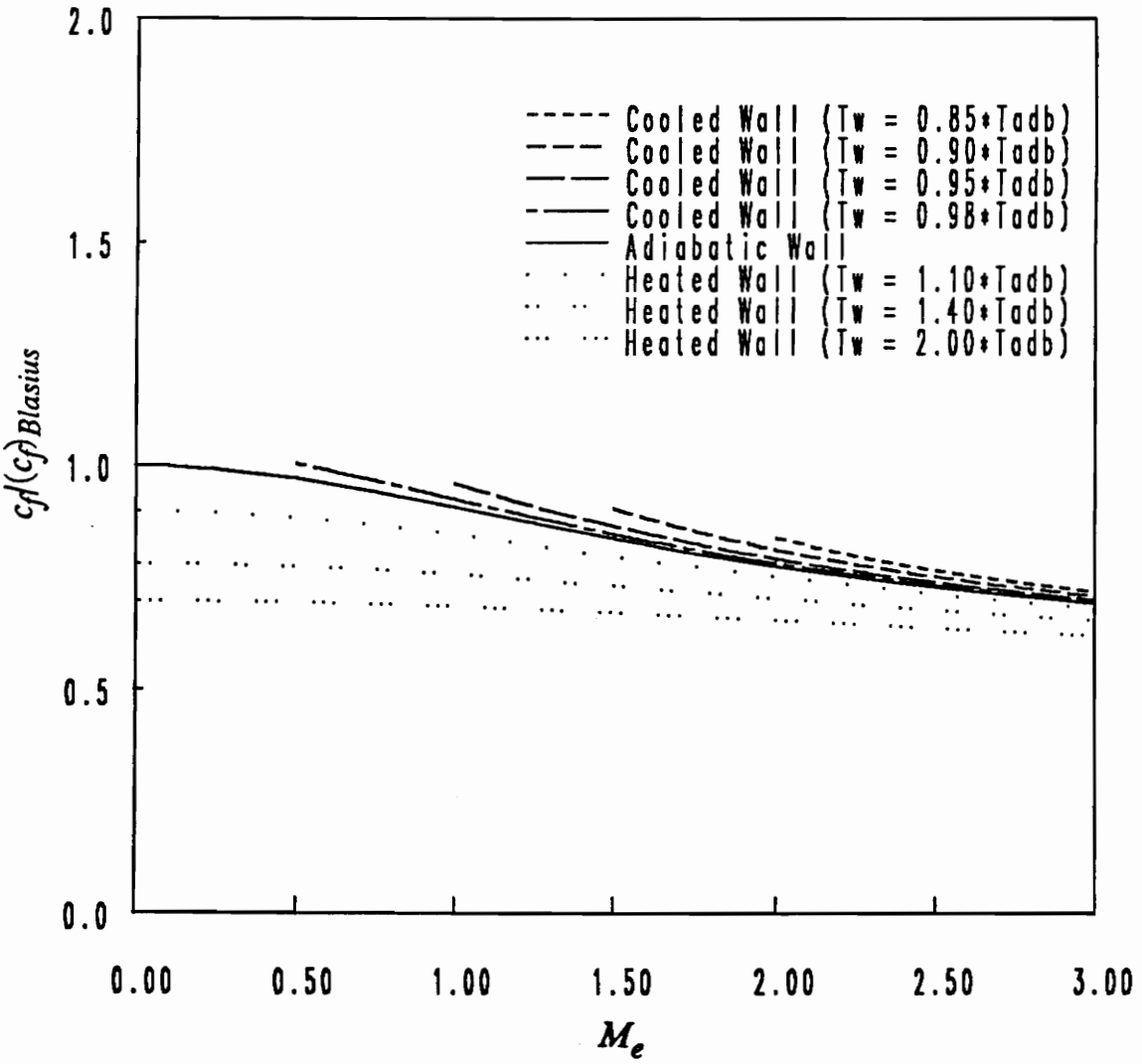

Figure 6.6. Plot of $c_f/(c_f)_{Blasius}$ vs. M_e in a dense-gas flow

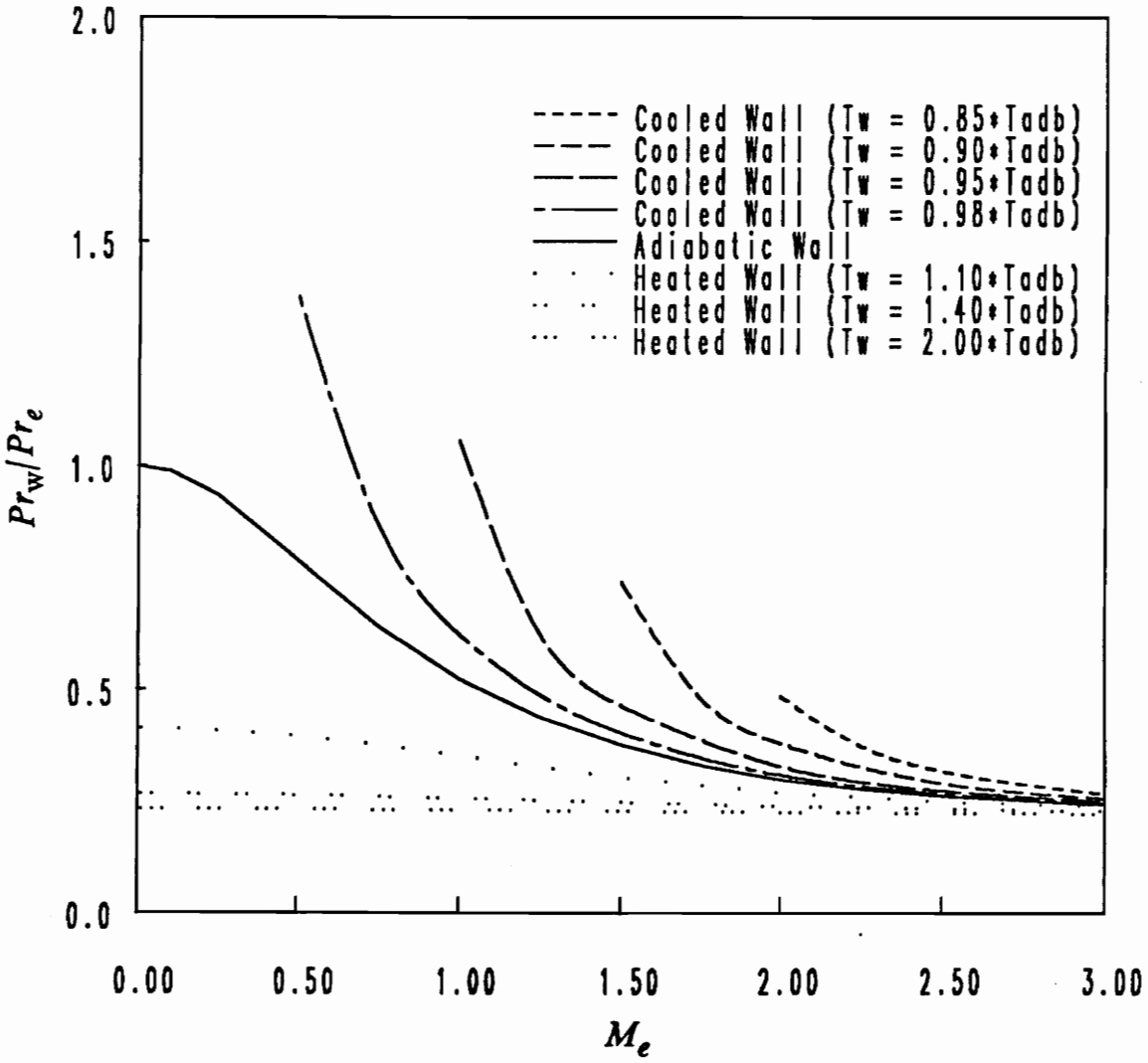

Figure 6.7. Plot of Pr_w/Pr_e vs. M_e in a dense-gas flow

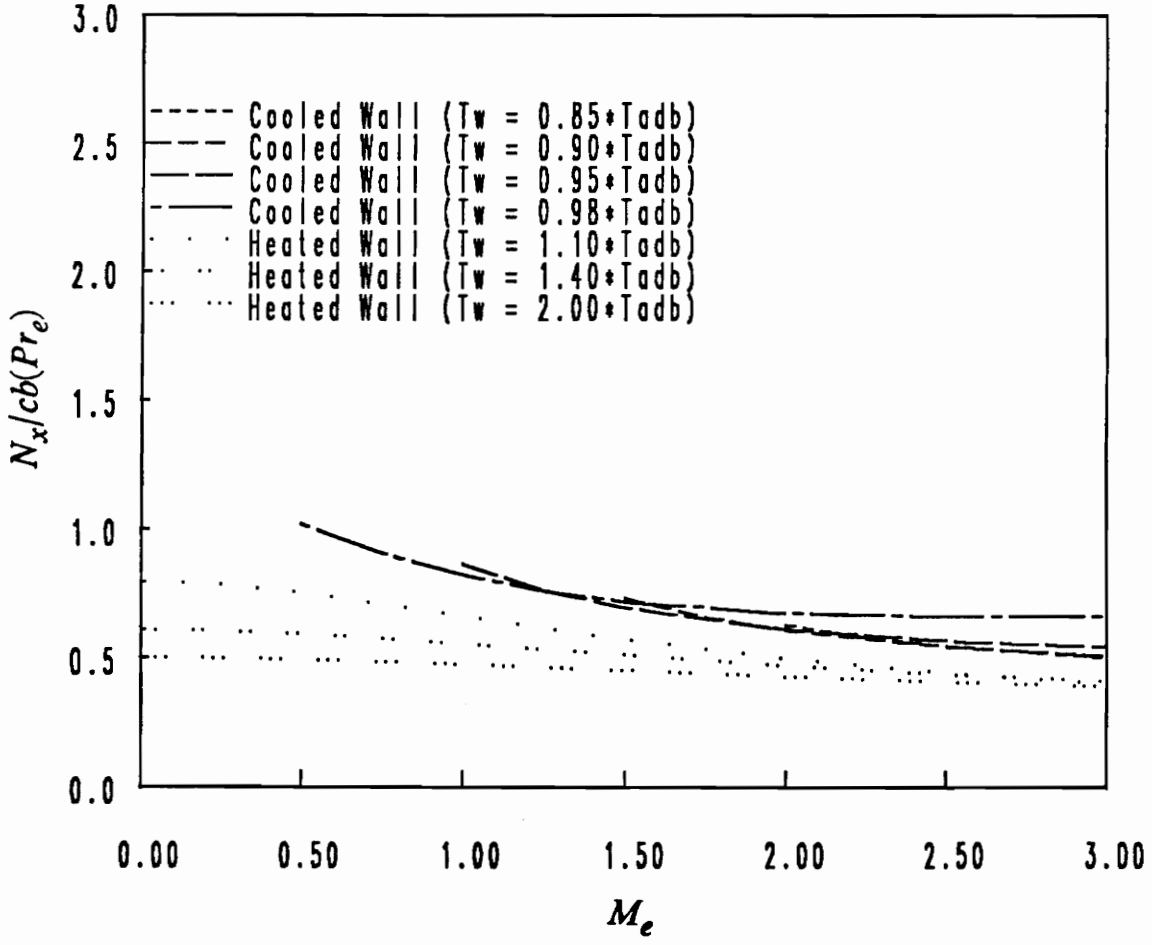

Figure 6.8. Plot of $N_x/cb(Pr_e)$ vs. M_e in a dense-gas flow

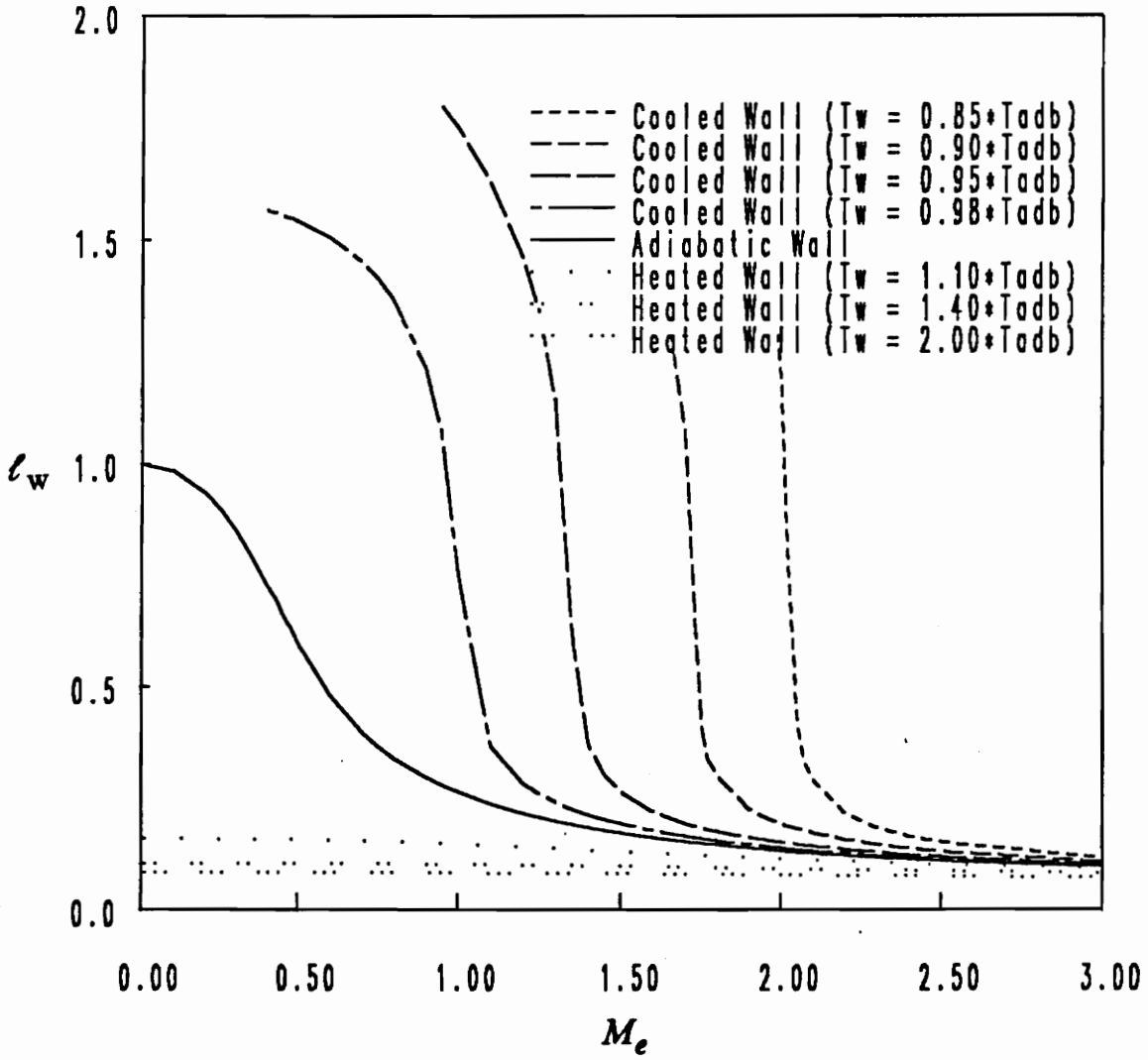

Figure 6.9. Plot of ℓ_w vs. M_e in a near-critical flow

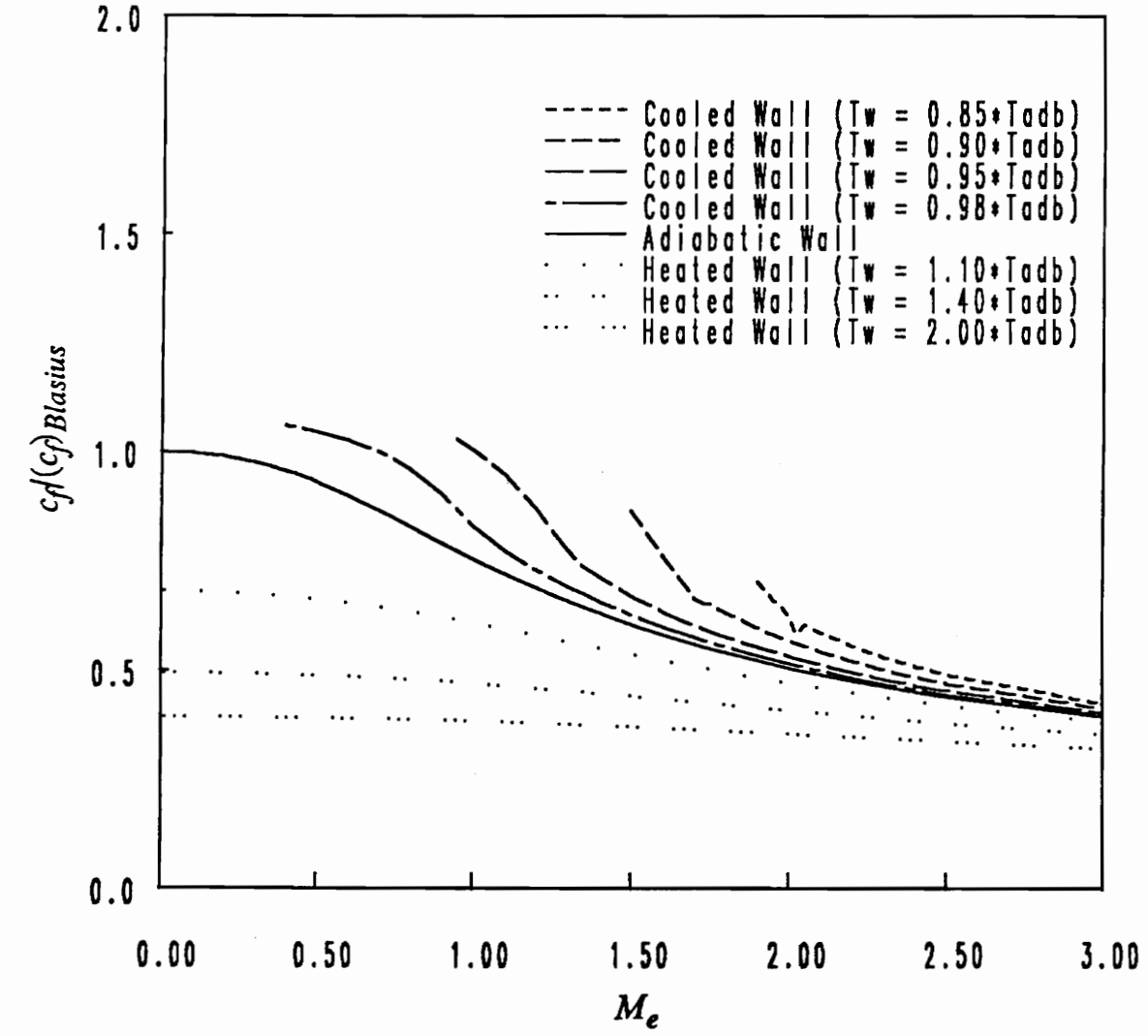

Figure 6.10. Plot of $c_f/(c_f)_{Blasius}$ vs. M_e in a near-critical flow

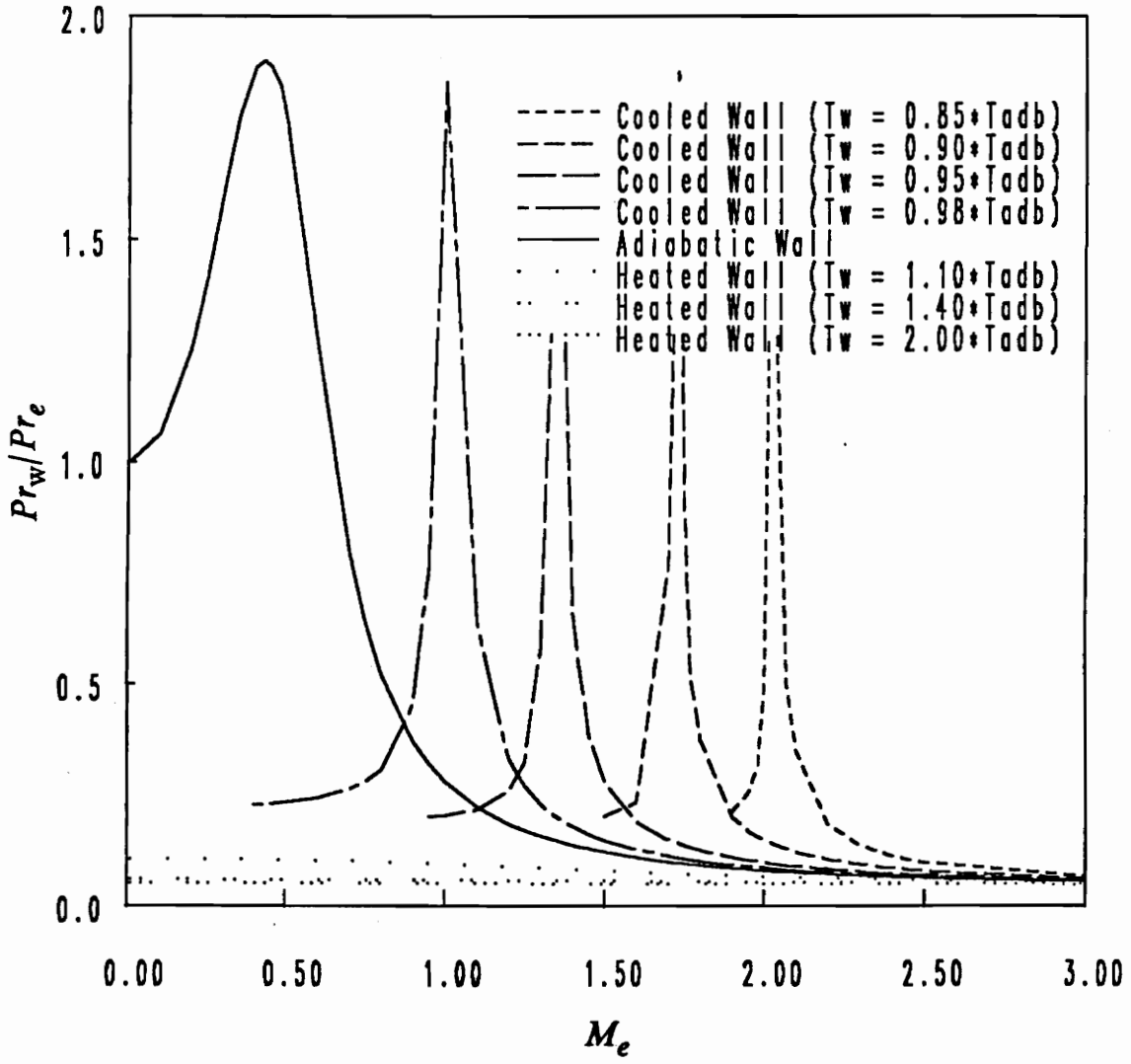

Figure 6.11. Plot of Pr_w/Pr_e vs. M_e in a near-critical flow

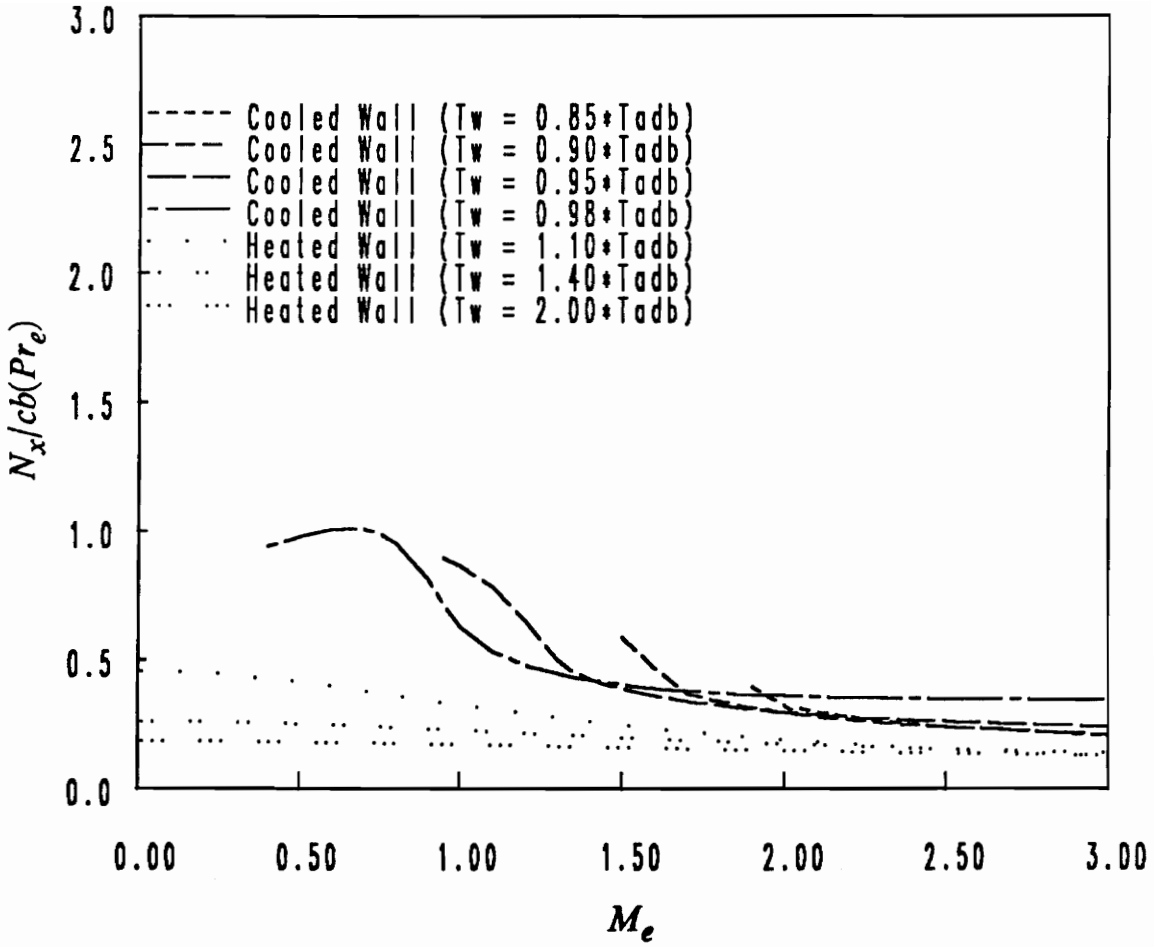

Figure 6.12. Plot of $N_x/cb(Pr_e)$ vs. M_e in a near-critical flow

Chapter 7

Stability Analysis of a General Fluid

Introduction

It is assumed that the growth of small disturbances in a laminar flowfield is the process which gives rise to the onset of turbulence. Therefore, in a preliminary effort to determine the likelihood that the dense-gas and near-critical flows discussed in the previous chapters will exhibit turbulent behavior, the stability of the laminar boundary layers in the presence of small disturbances is examined here. The basic idea is to return to the full unsteady Navier-Stokes-Fourier equations recorded in Chapter 2 and then to consider small disturbances propagating in the mean flow computed in Chapters 5 and 6. If the disturbances decay in time and space, the mean flow is considered stable. Likewise, if the disturbances grow without bound, the mean flow is considered unstable and the potential for transition to turbulent flow is recognized.

Physically, the small disturbances superimposed on the mean flow may be thought of as the result of wall roughness or irregularities in the external flow. Mathematically, the disturbances are

modeled as temporally and spatially varying waves having wavelengths that are short in comparison to the length scales associated with the growth of the boundary layer.

In this preliminary analysis, only the temporal stability of subsonic, two-dimensional, inviscid disturbances are considered. Furthermore, the analysis is restricted to flows over flat plates for which the mean-flow streamlines can be considered parallel and for which all mean-flow quantities are functions of $\bar{y}$ alone.

In the following section, the stability equations for a general fluid will be derived. The corresponding expression for the generalized inflection-point criterion will be extracted from the stability equations and used to characterize the stability of the boundary-layer flows.

Stability Equations for a General Fluid

The dimensional flow quantities resulting from the superposition of a disturbance on the mean flow are represented by $\tilde{q}$, where

$$\tilde{q}(\bar{x}, \bar{y}, \bar{t}) = \bar{q}(\bar{y}) + \bar{q}'(\bar{x}, \bar{y}, \bar{t}) \tag{7.1}$$

and $\tilde{q}$ is taken to be any flow variable appearing in Equations (2.1) - (2.4). Here, $\bar{q}$ denotes a dimensional mean-flow quantity as determined from the solution of the boundary-layer equations of Chapter 2, and $\bar{q}'$ is the dimensional disturbance imposed on the mean flow. The size of the disturbance is regarded as small in relation to the size of the mean-flow quantity so that

$$\frac{\bar{q}'}{\bar{q}} << 1. \tag{7.2}$$

To be consistent with the parallel-flow assumption, the vertical mean-flow velocity is assumed to be identically zero so that

$$\tilde{\mathrm{v}}(\bar{x}, \bar{y}, \bar{t}) = \bar{\mathrm{v}}'(\bar{x}, \bar{y}, \bar{t}). \tag{7.3}$$

The unsteady Navier-Stokes-Fourier equations governing $\tilde{q}$ are linearized to the order $\bar{q}'$, and the terms satisfying the original mean-flow equations are canceled. The results, in the limit of infinite Reynolds number, are the stability equations for a general fluid governing the two-dimensional, inviscid disturbance quantities $\bar{u}'$, $\bar{\mathrm{v}}'$, $\bar{\rho}'$, and $\bar{T}'$. The equations take the form

$$\frac{\partial \bar{\rho}'}{\partial \bar{t}} + \bar{\rho}\frac{\partial \bar{u}'}{\partial \bar{x}} + \bar{u}\frac{\partial \bar{\rho}'}{\partial \bar{x}} + \bar{\rho}\frac{\partial \bar{\mathrm{v}}'}{\partial \bar{y}} + \bar{\mathrm{v}}'\frac{d\bar{\rho}}{d\bar{y}} = 0, \tag{7.4}$$

$$\bar{\rho}\left(\frac{\partial \bar{u}'}{\partial \bar{t}} + \bar{u}\frac{\partial \bar{u}'}{\partial \bar{x}} + \bar{\mathrm{v}}'\frac{d\bar{u}}{d\bar{y}} \right) = -\frac{\partial \bar{p}'}{\partial \bar{x}}, \tag{7.5}$$

$$\bar{\rho}\left(\frac{\partial \bar{\mathrm{v}}'}{\partial \bar{t}} + \bar{u}\frac{\partial \bar{\mathrm{v}}'}{\partial \bar{x}} \right) = -\frac{\partial \bar{p}'}{\partial \bar{y}}, \tag{7.6}$$

$$\bar{\rho}\bar{c}_p\left(\frac{\partial \bar{T}'}{\partial \bar{x}} + \bar{u}\frac{\partial \bar{T}'}{\partial \bar{x}} + \bar{\mathrm{v}}'\frac{d\bar{T}}{d\bar{y}} \right) = \bar{\beta}\bar{T}\left(\frac{\partial \bar{p}'}{\partial \bar{t}} + \bar{u}\frac{\partial \bar{p}'}{\partial \bar{x}} \right). \tag{7.7}$$

In addition to Equations (7.4) - (7.7), an equation of state is also required to provide the relationship between pressure and temperature. Equations (7.4) - (7.7) are in agreement with those of Shen (1964) once the flow of two-dimensional, inviscid disturbances through a perfect gas is assumed.

The disturbances satisfying the stability equations are assumed to be two-dimensional traveling waves of the form

$$\bar{q}'(\bar{x}, \bar{y}, \bar{t}) = \bar{\hat{q}}(\bar{y}) e^{i\bar{\kappa}(\bar{x} - \bar{c}\bar{t})} + \text{ complex conjugate} \tag{7.8}$$

where $\bar{\hat{q}}$ is the eigenfunction describing the amplitude of the disturbance wave, $\bar{\kappa}$ is the wavenumber, $\bar{c}$ is the wave phase speed, and i is the imaginary number $\sqrt{-1}$. In general, $\bar{\hat{q}}$, $\bar{\kappa}$, and $\bar{c}$ are complex functions. In the temporal analysis employed here, $\bar{\kappa}$ is taken to be a real number, and $\bar{c}$ is regarded as complex. Equation (7.8) is recognized as the standard normal-mode form of the disturbances.

With the substitution of the normal-mode form for the disturbances into Equations (7.4) - (7.7), the stability equations may be written as

$$i\bar{\kappa}\bar{\hat{\rho}}(\bar{u} - \bar{c}) + i\bar{\kappa}\,\bar{\rho}\,\bar{\hat{u}} + \bar{\hat{v}}\frac{d\bar{\rho}}{d\bar{y}} + \bar{\rho}\frac{d\bar{\hat{v}}}{d\bar{y}} = 0, \tag{7.9}$$

$$i\bar{\kappa}\,\bar{\rho}\,\bar{\hat{u}}(\bar{u} - \bar{c}) + \bar{\rho}\,\bar{\hat{v}}\frac{d\bar{u}}{d\bar{y}} + i\bar{\kappa}\,\bar{\hat{p}} = 0, \tag{7.10}$$

$$i\bar{\kappa}\,\bar{\rho}\,\bar{\hat{v}}(\bar{u} - \bar{c}) + \frac{d\bar{\hat{p}}}{d\bar{y}} = 0, \tag{7.11}$$

$$\bar{\rho}\bar{c}_p\left[i\bar{\kappa}\,\bar{\hat{T}}(\bar{u} - \bar{c}) + \bar{\hat{v}}\frac{d\bar{T}}{d\bar{y}}\right] = \bar{\beta}\bar{T}i\bar{\kappa}\,\bar{\hat{p}}(\bar{u} - \bar{c}). \tag{7.12}$$

After considerable algebraic manipulation, Equations (7.9) - (7.12) may be reduced to a single equation in $\bar{\hat{v}}$,

$$\frac{d}{d\bar{y}}\left(\frac{1}{\bar{B}}\frac{d\bar{\hat{v}}}{d\bar{y}}\right) - \left[\frac{1}{(\bar{u} - \bar{c})}\frac{d}{d\bar{y}}\left(\frac{1}{\bar{B}}\frac{d\bar{u}}{d\bar{y}}\right) + \bar{\rho}\,\bar{\kappa}^2\right]\bar{\hat{v}} = 0 \tag{7.13}$$

where

$$\overline{B} = \frac{1}{\overline{\rho}} \left[1 - \frac{(\overline{u} - \overline{c})^2}{\overline{a}^2} \right]. \tag{7.14}$$

The remaining disturbance quantitities may be calculated once $\overline{\hat{v}}$ is known. The equation for the disturbance pressure, $\overline{\hat{p}}$, in terms of $\overline{\hat{v}}$ is

$$\frac{d\overline{\hat{p}}}{d\overline{y}} = i\,\overline{\kappa}\,\overline{\rho}(\overline{u} - \overline{c})\,\overline{\hat{v}}. \tag{7.15}$$

The disturbance density, $\overline{\hat{\rho}}$, and the disturbance velocity, $\overline{\hat{u}}$, may then be found in terms of $\overline{\hat{v}}$ and $\overline{\hat{p}}$ to be

$$\overline{\hat{\rho}} = \frac{1}{\overline{a}^2}\,\overline{\hat{p}} + \frac{i}{\overline{\kappa}(\overline{u} - \overline{c})} \frac{d\overline{\rho}}{d\overline{y}}\,\overline{\hat{v}} \tag{7.16}$$

and

$$\overline{\hat{u}} = \frac{i}{\overline{\kappa}(\overline{u} - \overline{c})} \frac{d\overline{u}}{d\overline{y}}\,\overline{\hat{v}} - \frac{1}{\overline{\rho}(\overline{u} - \overline{c})}\,\overline{\hat{p}}. \tag{7.17}$$

The disturbance temperature, $\overline{\hat{T}}$, is determined from the perturbed equation of state once $\overline{\hat{\rho}}$ and $\overline{\hat{p}}$ are known. The non-dimensional form of Equation (7.13) may be written as

$$\frac{d}{dy}\left(\frac{1}{B} \frac{d\hat{v}}{dy} \right) - \left[\frac{1}{(u - c)} \frac{d}{dy}\left(\frac{1}{B} \frac{du}{dy} \right) + \rho\kappa^2 \right] \hat{v} = 0. \tag{7.18}$$

Here the scalings adopted in Chapter 2 are applied to the velocities and the density,

$$y = \frac{\bar{y}}{\bar{\delta}}, \quad \kappa = \bar{\kappa}\bar{\delta}, \quad B = \frac{\bar{B}}{\bar{\rho}_c}, \tag{7.19}$$

and $\bar{\delta} \propto 1/\sqrt{Re_{\bar{x}}}$ is the thickness of the boundary layer, where $Re_{\bar{x}}$ is the Reynolds number based on $\bar{x}$.

The familiar perfect-gas form of Equation (7.18) may be recovered by recognizing that

$$\bar{p} \to \bar{\rho}\bar{R}\bar{T} \qquad \text{and} \qquad \bar{a}^2 \to \gamma \bar{R}\bar{T} \tag{7.20}$$

in the perfect-gas limit. Consequently, Equation (7.18) reduces to

$$\frac{d}{dy}\left[\frac{1}{P}\frac{d\hat{v}}{dy}\right] - \left[\frac{1}{(u-c)}\frac{d}{dy}\left(\frac{1}{P}\frac{du}{dy}\right) + \frac{\kappa^2}{T}\right]\hat{v} = 0 \tag{7.21}$$

where

$$P = T - M_\infty^2 (u-c)^2 \tag{7.22}$$

and all terms have been rescaled with freestream quantities. Equations (7.21) - (7.22) are identical to the forms given by Shen (1964).

Boundary Conditions

The formulation of the stability equations is complete once the appropriate boundary conditions for Equation (7.18) are specified. Equation (7.18) is a second-order ordinary differential equation requiring two boundary conditions. The first of these conditions is the no-penetration condition at the wall, which is imposed by

$$\hat{v} = 0 \quad \text{on} \quad y = 0. \tag{7.23}$$

The second boundary condition restricts the disturbance to be bounded at the edge of the boundary layer.

The ordinary differential equation governing the disturbance velocity, coupled with the appropriate boundary conditions, is now solvable. As with the mean-flow equations, no analytic solution to the disturbance equation is available for the general case. Thus, a solution must be generated numerically. In the present analysis, however, the numerical solution to the disturbance equation is not provided. Rather, the generalized inflection-point criterion is used to provide a qualitative measure of the stability characteristics of general boundary-layer flows. The numerical solution to the stability equation is left for future investigations.

Generalized Inflection-Point Criterion

The generalized inflection-point criterion of Lees and Lin (1946), which serves as a necessary and sufficient condition for the existence of a neutral subsonic disturbance, may be extracted from

Equation (7.18). Because the general form of Equation (7.18) is the same as the form of the standard perfect-gas inviscid stability equation, arguments similar to those employed by Shen (1964) are used to derive the generalized inflection-point condition.

For a neutral subsonic disturbance, the imaginary part of the wave speed is identically zero and the velocity of the disturbance relative to the freestream must satisfy $c > 1 - 1/M_e$. Because it is expected that $0 < c < 1$, there exists some point in the flow $y = y_s$, defined as the point at which $u = c$, where it is required that

$$\frac{d}{dy}\left(\frac{1}{B}\frac{du}{dy}\right)\bigg|_{y_s} \to 0 \tag{7.24}$$

in order to guarantee bounded solutions. Furthermore, because $B = \frac{1}{\rho}$ at y_s, the necessary condition for the existence of a neutral subsonic disturbance is

$$\frac{d}{dy}\left(\rho\frac{du}{dy}\right)\bigg|_{y_s} = 0. \tag{7.25}$$

Equation (7.25) is also a sufficient condition provided that the velocity of the disturbance ρpropagation relative to the freestream is subsonic. Equation (7.25) is recognized as the generalized inflection-point criterion. Note that the equation is identical to the perfect-gas result given by Mack (1969).

In order to determine the conditions under which boundary-layer flows are unstable, it is necessary to identify what conditions will cause a generalized inflection point to exist within a particular flow. At the outer edge of the boundary layer,

$$\mathscr{I} \equiv \frac{d}{dy}\left(\rho\frac{du}{dy}\right) \to 0^{-}. \tag{7.26}$$

Therefore it follows immediately that any boundary-layer flow in which $\mathscr{I}$ at the wall, $\mathscr{I}_w$, is greater than zero must possess at least one generalized inflection point somewhere within the thickness. Furthermore, at least one of these inflection points must correspond to a local maximum of the quantity $\rho du/dy$. A negative value of $\mathscr{I}_w$ does not preclude the existence of a generalized inflection point in the boundary layer, and hence an unstable flow. However, if an inflection point exists when $\mathscr{I}_w < 0$, it must be associated with a local minimum of $\rho du/dy$. Furthermore, as a consequence of Equation (7.26), such a flow must also contain a generalized inflection point, located farther from the wall, which is associated with a local maximum of $\rho du/dy$. Because of the possibility for the existence of a generalized inflection point when $\mathscr{I}_w < 0$, no general statement about the stability of a boundary-layer flow can be made on the inspection of $\mathscr{I}_w$ alone. Rather, the variation of $\rho du/dy$ throughout the boundary layer must be examined for local maxima and minima.

In the following section, the value of $\mathscr{I}_w$ and, when necessary, the variation of $\rho du/dy$ are examined in order to characterize the stability of the boundary-layer flows. For cases that exhibit $\mathscr{I}_w > 0$, the flow is conclusively unstable, whereas for cases having $\mathscr{I}_w < 0$, the plot of $\rho du/dy$ through the thickness must be examined for the presence of generalized inflection points, which indicate instability. Specifically, effects of heating and cooling of the wall on stability are investigated.

Role of Wall Viscosity in Inviscid Stability

It is generally believed that cooling of the wall tends to stabilize boundary-layer flows of gases and that heating of the wall has a destabilizing effect. The arguments on which this belief is based are linked to the variation of the viscosity at the wall as a result of heating and cooling. To see how the viscosity influences the stability of boundary-layer flows, note that $\mathscr{I}_w$ may be written as

$$\mathcal{I}_w = \left[\frac{d\rho}{dy}\frac{du}{dy} + \rho\frac{d^2u}{dy^2} \right]_w, \tag{7.27}$$

and that the last term on the right in Equation (7.27) may obtained from the momentum equation, Equation (2.7), as

$$\left.\frac{d^2u}{dy^2}\right|_w = \left[-\frac{1}{\mu}\frac{d\mu}{dy}\frac{du}{dy} \right]_w. \tag{7.28}$$

As above, the subscript w refers to evaluation at the wall. The result is that $\mathcal{I}_w$ may be cast in terms of the gradients of density and viscosity at the wall as

$$\mathcal{I}_w = \left[\frac{du}{dy}\left(\frac{d\rho}{dy} - \frac{\rho}{\mu}\frac{d\mu}{dy} \right) \right]_w. \tag{7.29}$$

Furthermore, because

$$\left.\frac{du}{dy}\right|_w > 0 \tag{7.30}$$

for all non-separated flows, it is apparent that the sign of $\mathcal{I}_w$ depends on the slopes of the density and the viscosity at the wall.

For an ideal gas, in which the viscosity may be regarded as an increasing function of temperature alone, heating of the wall results in a negative gradient of viscosity at the wall. Thus, the value of $\mathcal{I}_w$ is positive because the slope of the density at the wall must also be positive. Consequently, heating of the wall destabilizes boundary-layer flows, at least when the density

dependence of the viscosity is negligible. In contrast, cooling of the wall tends to stabilize the flow because the positive gradient of viscosity at the wall causes $\mathscr{I}_w$ to become increasingly negative.

The viscosity of liquids behaves in a manner which is opposite of that of a gas with regard to temperature. Furthermore, liquids are generally regarded as being incompressible. Thus, Equation (7.29) reduces to

$$\mathscr{I}_w = \left[-\frac{\rho}{\mu}\frac{d\mu}{dy}\frac{du}{dy} \right]_w \tag{7.31}$$

and the effects of wall temperature on the stability of boundary-layer flows of liquids are directly related to the viscosity gradient at the wall. The stability of boundary-layer flows of liquids due to heating and cooling is exactly opposite to that of gases; that is, heating tends to stabilize the flow while cooling tends to destabilize the flow.

When the density dependence of the viscosity is included, the effects of heating and cooling on the stability of the boundary layer are not as straightforward as the two limiting cases discussed above seem to suggest. In a dense-gas or near-critical flow, cooling of the boundary layer does not necessarily produce a positive gradient of the viscosity at the wall, nor does heating necessarily yield a negative wall viscosity gradient. In particular, the slope of the viscosity at the wall will depend on the value of the wall viscosity relative to the local minimum shown in Figure 1.2.

When the wall viscosity is very close to the local minimum of μ, cooling of the wall could yield a viscosity gradient at the wall which is negative. The negative viscosity gradient has the potential to outweigh the negative density gradient at the wall and yield $\mathscr{I}_w > 0$. Furthermore, if the wall viscosity is very close to the local minimum, heating of the wall could also yield a wall viscosity gradient which is negative. The result would be a boundary-layer flow for which neither heating nor cooling has a stabilizing effect.

For an ideal gas, it is observed that the influences of viscosity and density on the stability of boundary-layer flows are complementary. That is, when the wall is cooled, the gradients of density and viscosity at the wall both contribute to a negative value of $\mathscr{I}_w$, and when the wall is heated the

gradients of density and viscosity at the wall both contribute to the destabilization of the flow. As a result, it is sufficient to examine only the behavior of the viscosity at the wall due to heating and cooling when assessing the stability of ideal-gas boundary-layer flows.

When the density dependence of the viscosity is included, however, the viscosity cannot be regarded as the primary influencing factor on the stability of dense-gas boundary-layer flows. Rather, the stability depends on a competition between the viscosity and the density, and in general it is unclear which factor is more dominant.

The ambiguity involved in determining the relative importance of density and viscosity on the stability of boundary-layer flows can be removed by considering the kinematic viscosity, ν. Note that Equation (7.29) may be cast as

$$\mathscr{I}_{\mathrm{w}} = \left[-\frac{du}{dy}\frac{\rho}{\nu}\frac{d\nu}{dy} \right]_{\mathrm{w}} \tag{7.32}$$

where $\nu = \mu/\rho$. As a result, the assessment of the stability of dense-gas boundary-layer flows may be accomplished through the inspection of a single parameter, namely the slope of the kinematic viscosity at the wall.

In the ensuing chapter, the generalized inflection-point criterion is used to characterize the stability of the flow of nitrogen over a flat plate for the three freestream thermodynamic states, and the impact of the non-classical variation of the viscosity on the existence of a generalized inflection point is analyzed.

Chapter 8

Stability Results

The variations of density, viscosity, and $\rho du/dy$ through the boundary layer for the flow of nitrogen over a flat plate at various freestream thermodynamic states and a freestream Mach number of 2.0 are presented in this chapter. Results for flows over adiabatic, heated, and cooled walls are shown. For each of the three freestream thermodynamic states, the temperatures of the heated and cooled walls, T_w, are measured relative to the corresponding temperature of the adiabatic wall, T_{adb}.

The stability characteristics of the flows with a freestream Mach number of 2.0 are not necessarily representative of the behavior over a wide range of freestream Mach numbers. However, the amount of temperature increase associated with the adiabatic-wall cases at a freestream Mach number of 2.0 permits some flexibility in the degree of cooling possible before the maximum-density limit of the equation of state is reached in the near-critical flow or before the two-phase region is encountered in the dense-gas flow. Therefore, the results corresponding to a freestream Mach number of 2.0 are chosen for illustration in this first step toward understanding the impact of dense-gas effects on the stability characteristics of boundary-layer flows.

An examination of Figures 8.1 - 8.3, which are the density, viscosity, and $\rho du/dy$ variations through the boundary layer for the one-atmosphere case, reveals that the one-atmosphere flow is stabilized on cooling and destabilized on heating. The behavior of the slopes of the viscosity and the density at the wall due to changes in the wall temperature are observed to yield the anticipated effects on the stability characteristics as predicted in the classical theories.

The dense-gas boundary layer is also seen to stabilize on cooling; in addition, instability is preserved on heating as reflected in the $\rho du/dy$ variations for the dense-gas case plotted in Figure 8.6. However, an examination of the density and viscosity variations through the boundary layer, illustrated in Figures 8.4 and 8.5, reveals that the viscosity actually tends to oppose the stabilization of the boundary layer in the case for which $T_w = 0.80 * T_{adb}$. For in this case, the variation of the viscosity resembles that of a heated-wall flow of perfect gases; that is, the viscosity gradient at the wall is negative. It is observed that the large negative density gradient at the wall for this case is responsible for the negative value of $\mathscr{I}_w$ and hence the disappearance of the inflection point. At a freestream Mach number of 2.0, further cooling of the wall causes the flow to enter the two-phase region. Therefore, it is unclear whether increased cooling of the boundary layer will yield negative viscosity gradients at the wall which are large enough to counterbalance the stabilizing effect of the negative density gradients at the wall and thus produce an unstable flow. The example shown here provides specific numerical evidence for the idea that the stability depends on a competition between viscosity and density and that the density may actually be the dominant factor in determining the existence of generalized inflection points in certain boundary-layer flows.

The variations of $\rho du/dy$ for the near-critical flow are plotted in Figure 8.11. This case provides an example for which the near-critical boundary-layer is neither stabilized by heating nor by cooling. The reason for this behavior is found through an examination of the viscosity variations provided in Figures 8.8 - 8.10 where it is seen that the variation of the viscosity is qualitatively the same for the heated- and cooled-wall cases. For both heated and cooled walls, the gradient of the viscosity at the wall is negative. In the cooled-wall case, the negative viscosity gradients at the wall overpower the stabilizing influence of the negative density gradients. The result is a positive value of $\mathscr{I}_w$ even for the cooled-wall cases.

An additional peculiarity of the near-critical flows is the existence of multiple local maxima in the $\rho du/dy$ variations for the cases in which $T_w = 0.85^* T_{adb}$ and $T_w = 0.84^* T_{adb}$. Initial cooling of the boundary layer seems to contribute to the disappearance of the original inflection point associated with the adiabatic-wall case, thus suggesting that cooling of the wall produces the anticipated stabilizing effect. However, as can be seen in Figure 8.11, additional cooling appears to give rise to a second local maximum in $\rho du/dy$ which originates at and then moves away from the wall. Numerical studies which involved increases of the resolution of the computational grid were performed, leading to the conclusion that the existence of multiple local maxima in the near-critical $\rho du/dy$ variations are of physical rather than numerical origin.

The explanation for the existence of multiple local maxima in the near-critical $\rho du/dy$ variations is apparently linked to the behavior of the density relative to the viscosity throughout the boundary layer. As seen in the example of the dense-gas flows shown previously, the near-critical $\rho du/dy$ variations indicate that the stability is dependent on a competition between the viscosity and the density. Therefore, it appears that a more illuminating view of the determination of the stability characteristics of general boundary-layer flows involves an analysis of the kinematic-viscosity behavior throughout the boundary layer as opposed to the variations of density or shear viscosity alone.

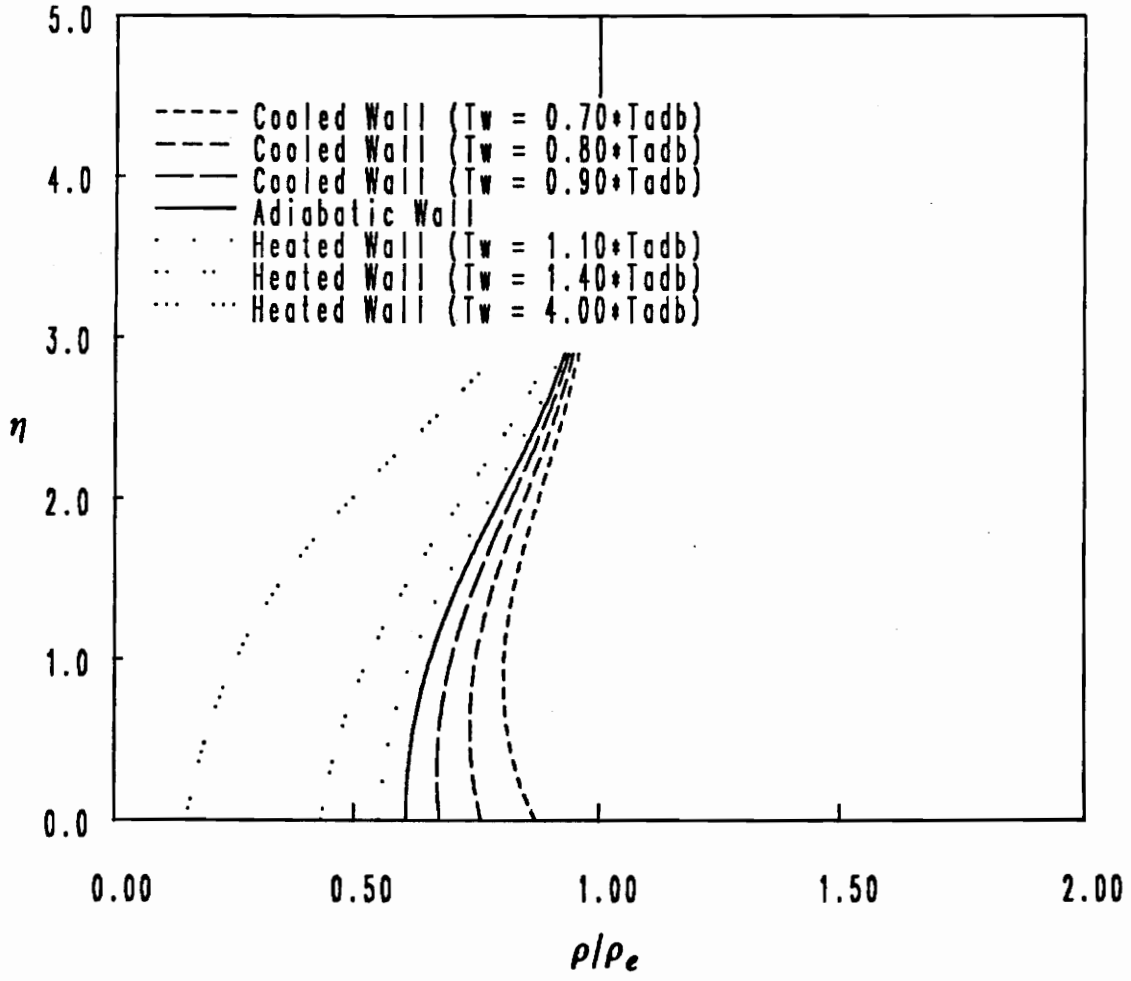

Figure 8.1. **Plot of ρ/ρ_e vs. η in a one-atmosphere flow:** Illustrated are the results for a freestream Mach number of 2.0 and a freestream temperature of $1.01*T_e$. The one-atmosphere case corresponds to a freestream volume of $115*v_e$.

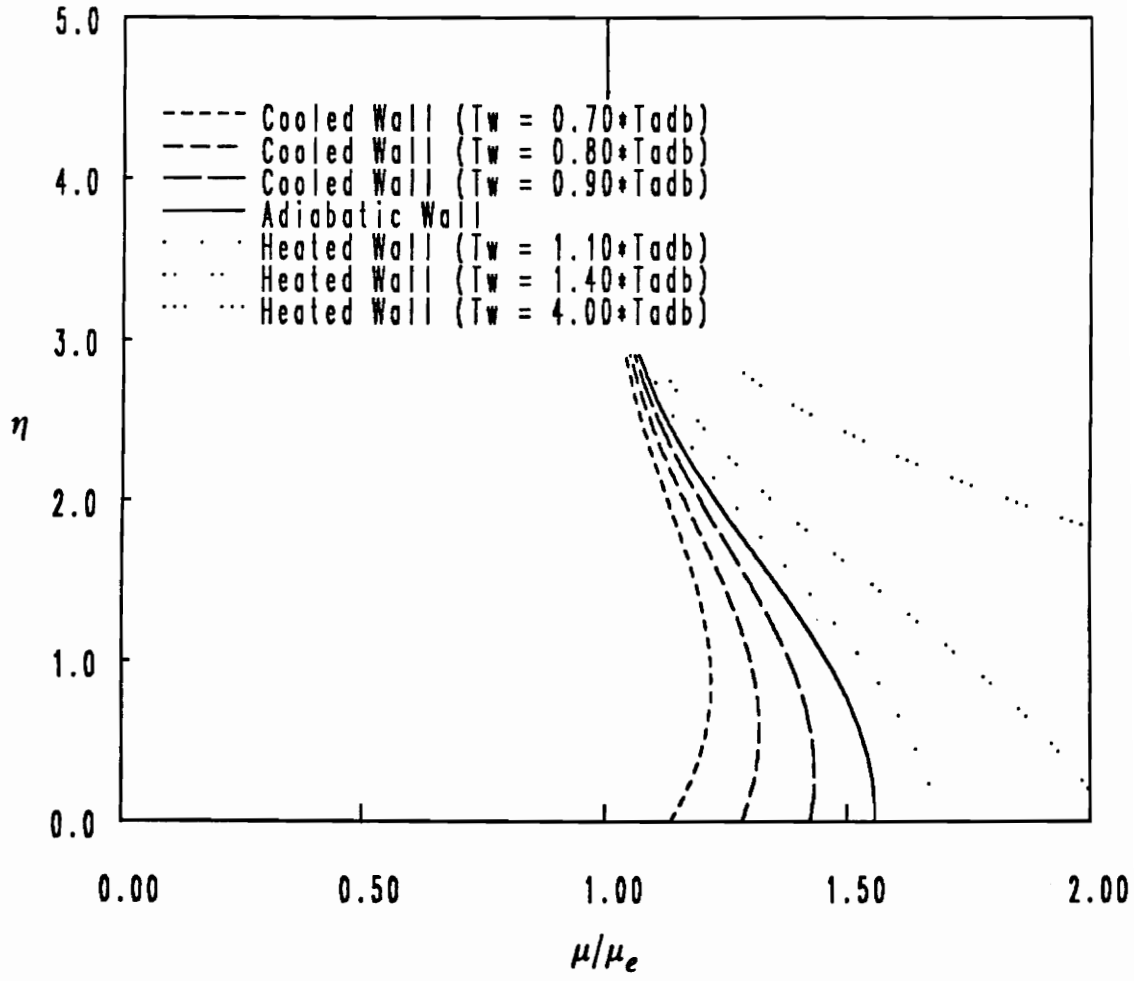

Figure 8.2. Plot of μ/μ_e vs. η in a one-atmosphere flow: Illustrated are the results for a freestream Mach number of 2.0 and a freestream temperature of $1.01*T_e$. The one-atmosphere case corresponds to a freestream volume of $115*v_e$.

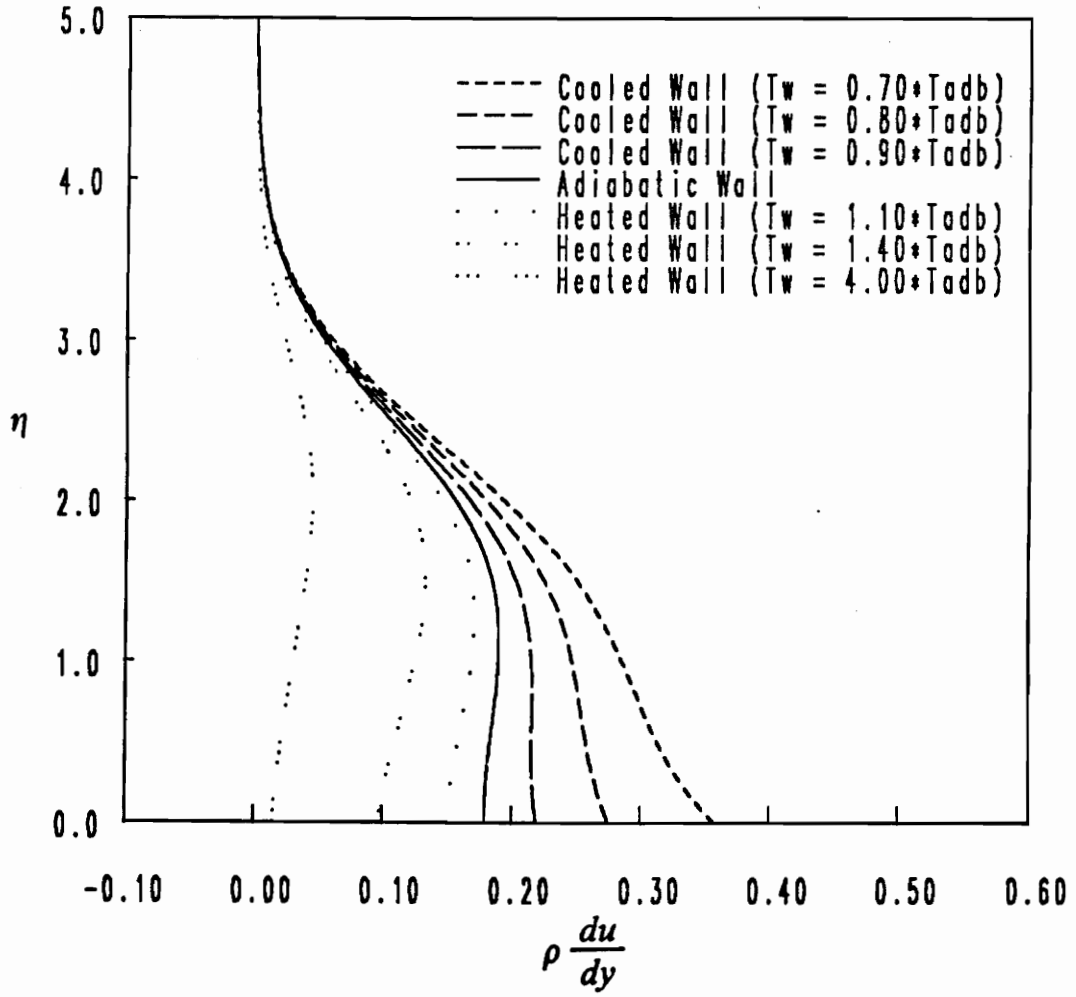

Figure 8.3. **Plot of $\rho(du/dy)$ vs. η in a one-atmosphere flow:** Illustrated are the results for a freestream Mach number of 2.0 and a freestream temperature of $1.01*T_c$. The one-atmosphere case corresponds to a freestream volume of $115*v_c$.

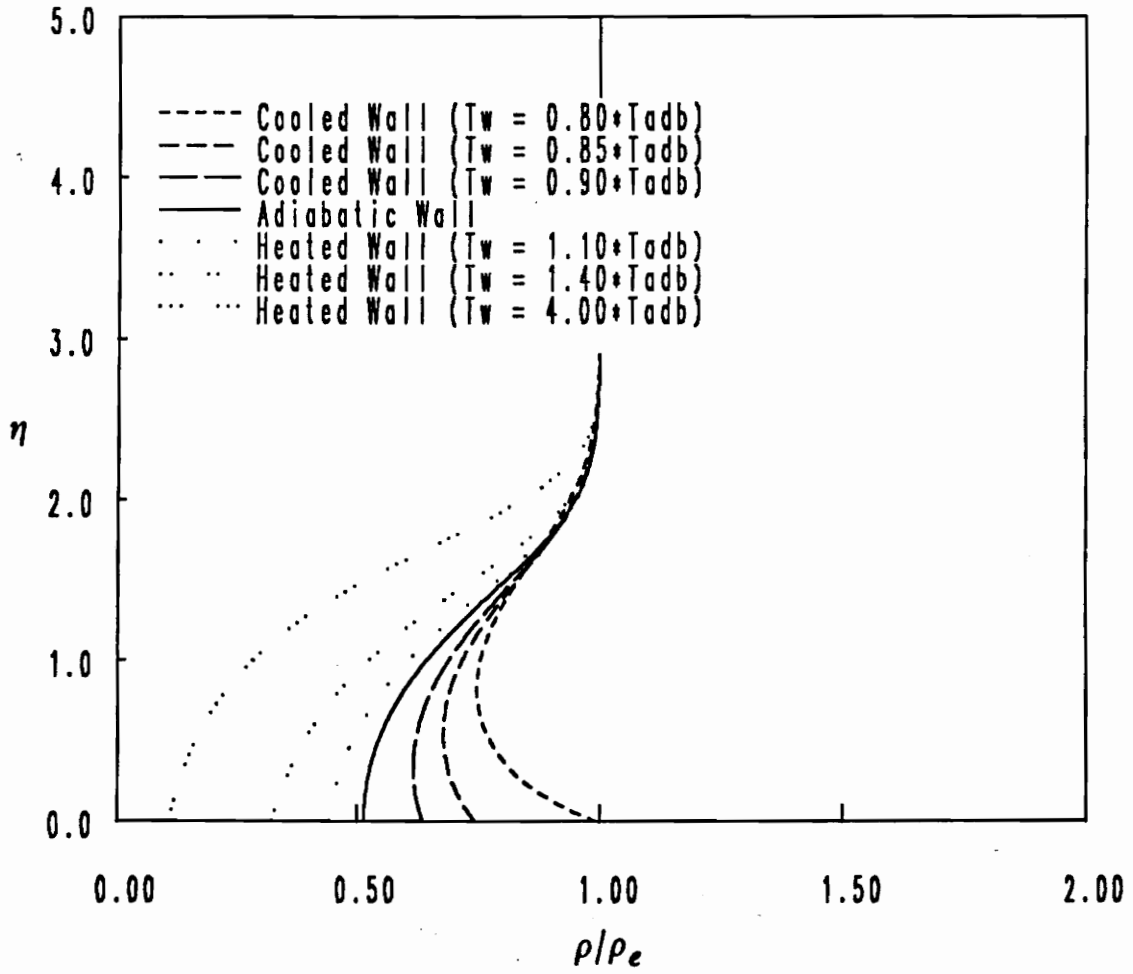

Figure 8.4. Plot of ρ/ρ_e vs. η in a dense-gas flow: Illustrated are the results for a freestream Mach number of 2.0 and a freestream temperature of $1.01*T_c$.

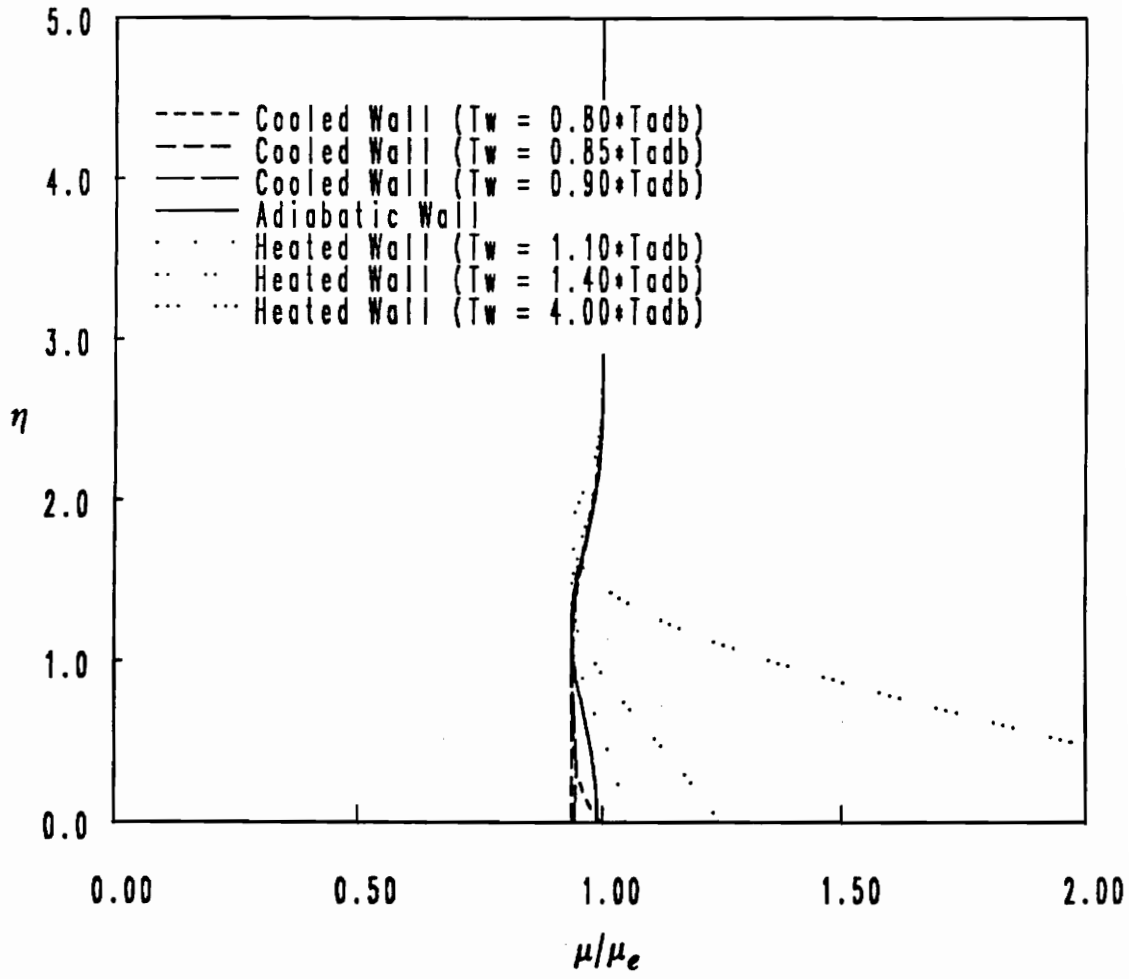

Figure 8.5. Plot of μ/μ_e vs. η in a dense-gas flow: Illustrated are the results for a freestream Mach number of 2.0 and a freestream temperature of $1.01*T_c$.

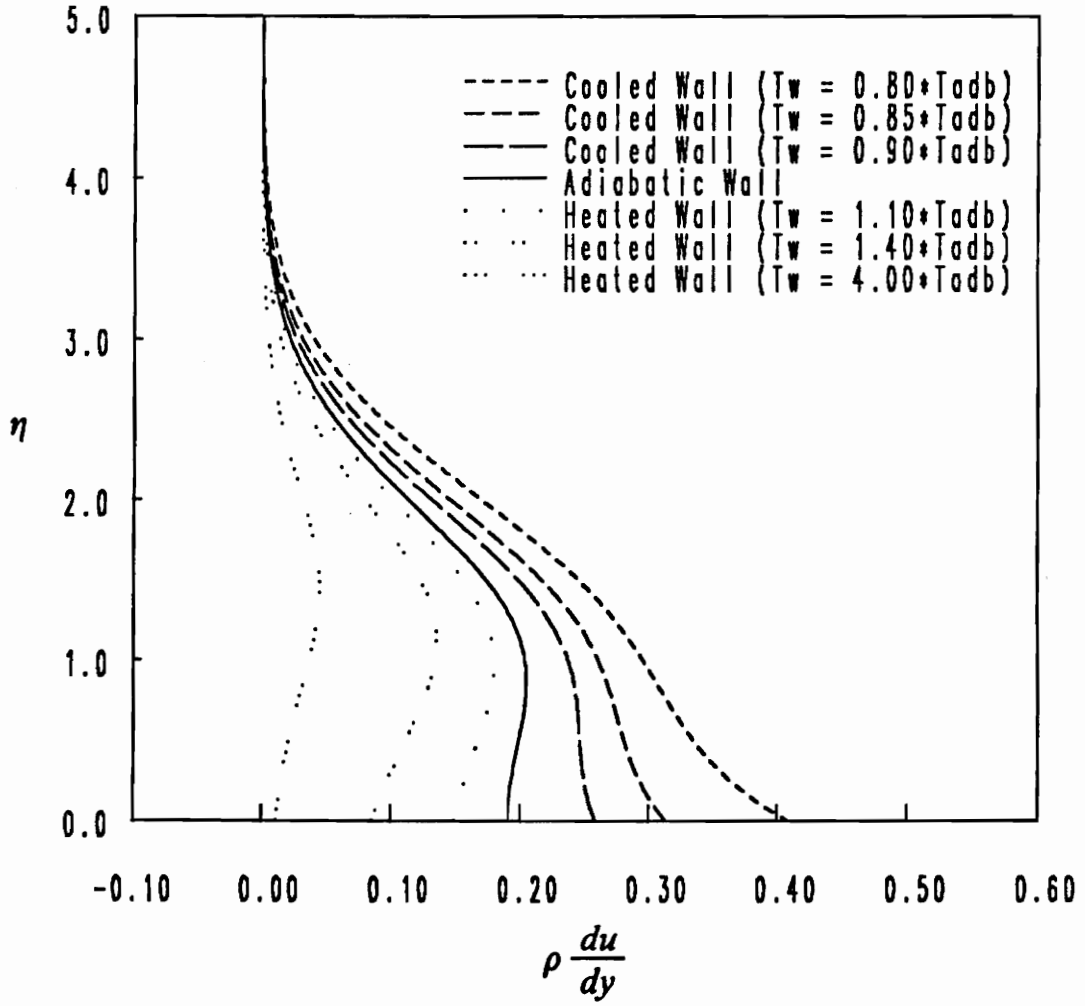

Figure 8.6. Plot of $\rho(du/dy)$ vs. η in a dense-gas flow: Illustrated are the results for a freestream Mach number of 2.0 and a freestream temperature of $1.01*T_c$.

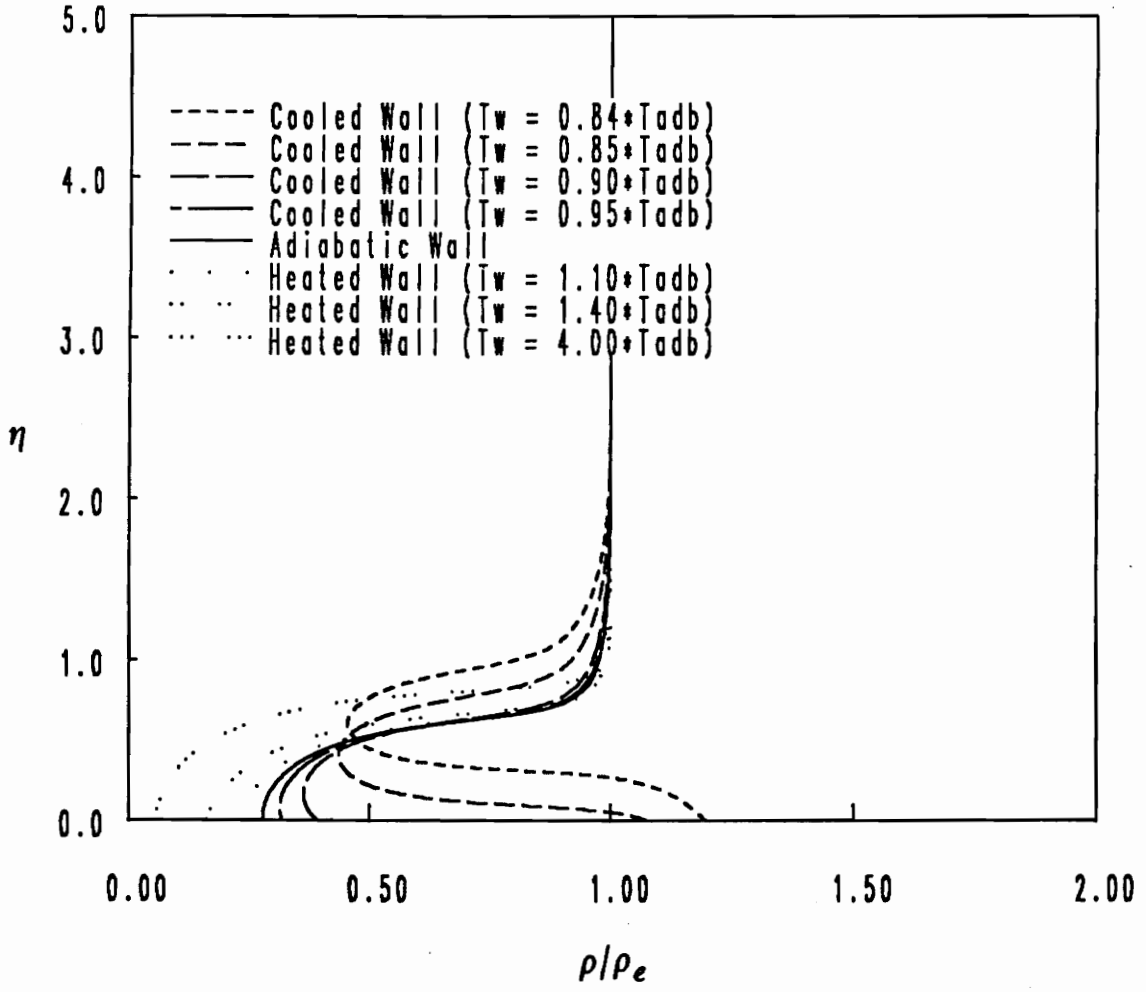

Figure 8.7. Plot of ρ/ρ_e vs. η in a near-critical flow: Illustrated are the results for a freestream Mach number of 2.0 and a freestream temperature of $1.01*T_c$.

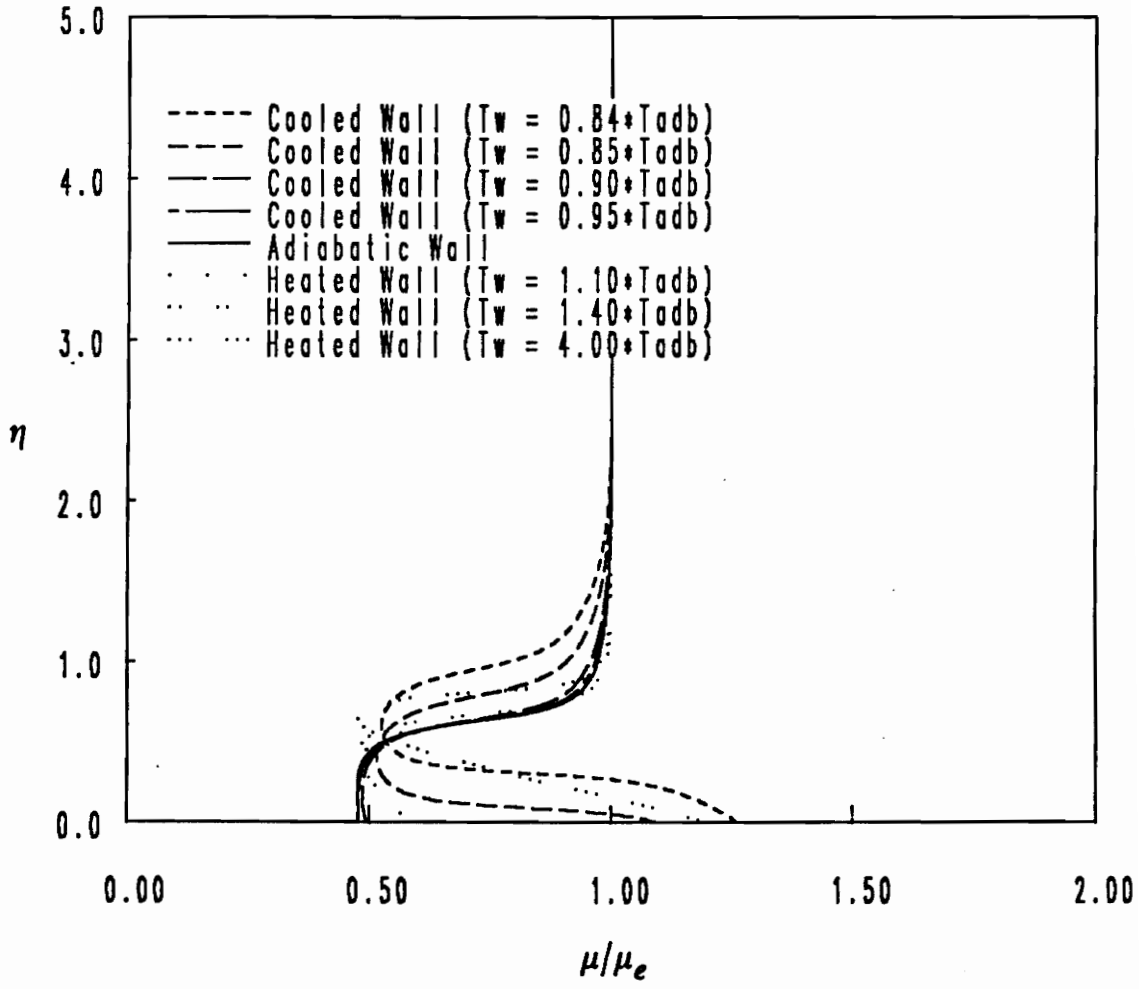

Figure 8.8. **Plot of μ/μ_e vs. η in a near-critical flow:** Illustrated are the results for a freestream Mach number of 2.0 and a freestream temperature of $1.01*T_c$.

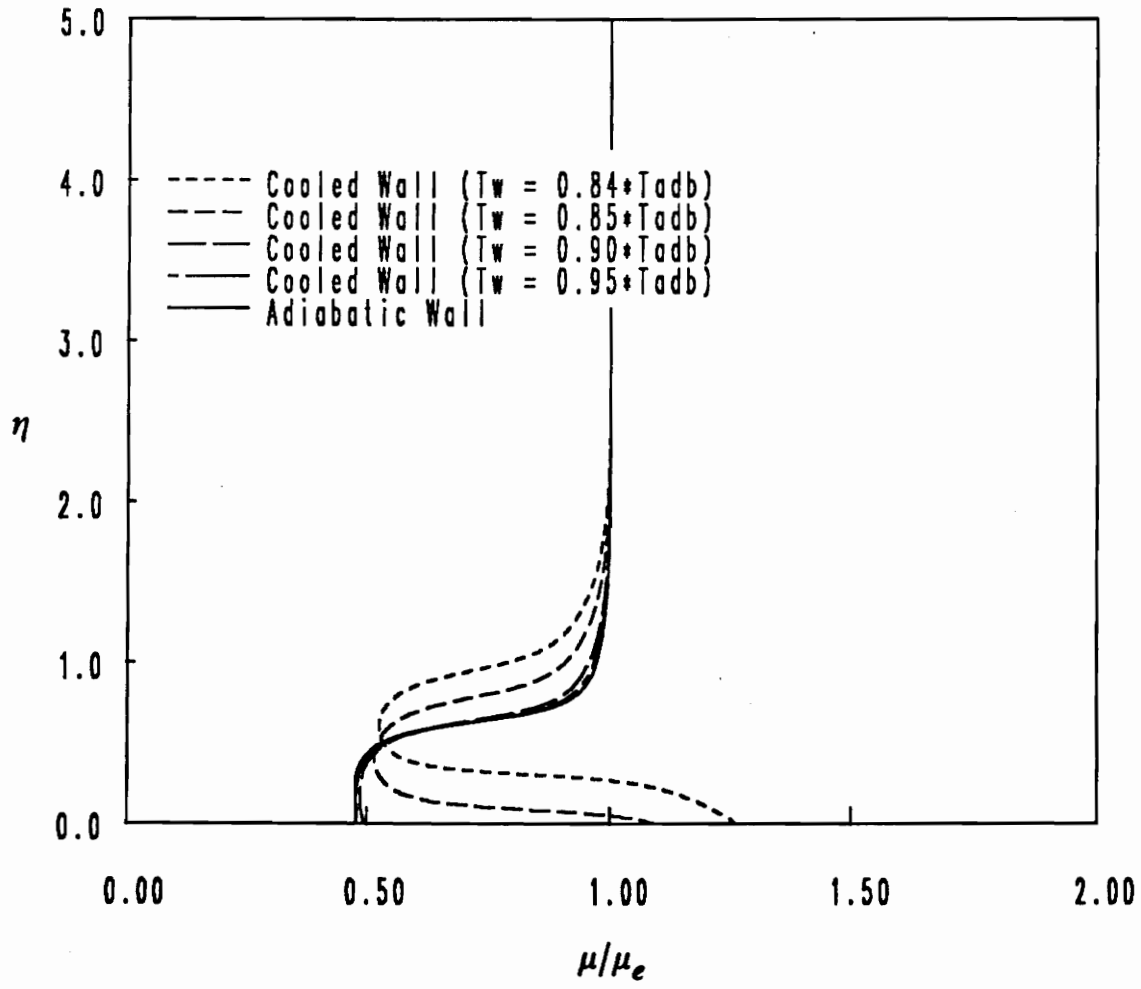

Figure 8.9. Plot of μ/μ_e vs. η for cooled walls in a near-critical flow: Illustrated are the results for a freestream Mach number of 2.0 and a freestream temperature of $1.01*T_c$.

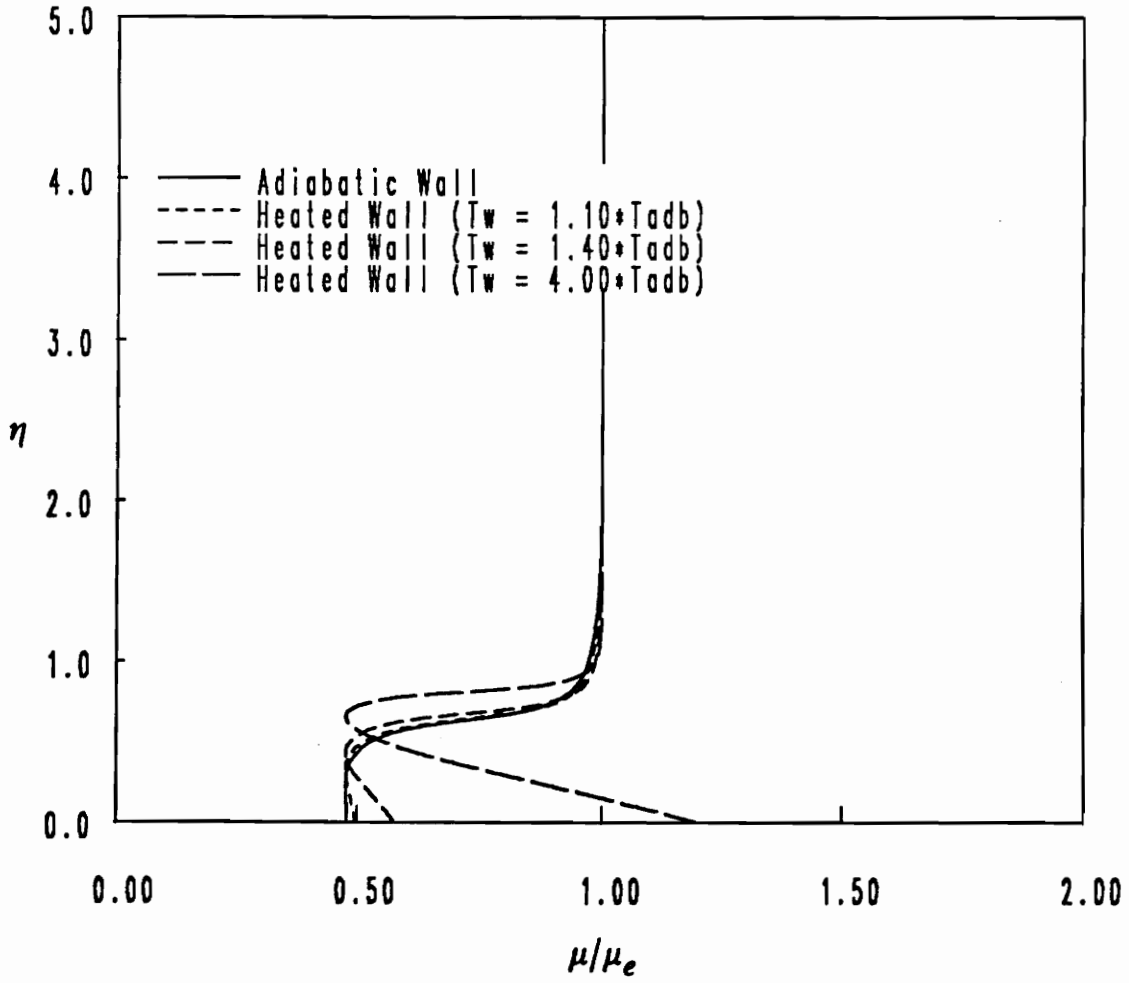

Figure 8.10. **Plot of μ/μ_e vs. η for heated walls in a near-critical flow:** Illustrated are the results for a freestream Mach number of 2.0 and a freestream temperature of $1.01*T_c$.

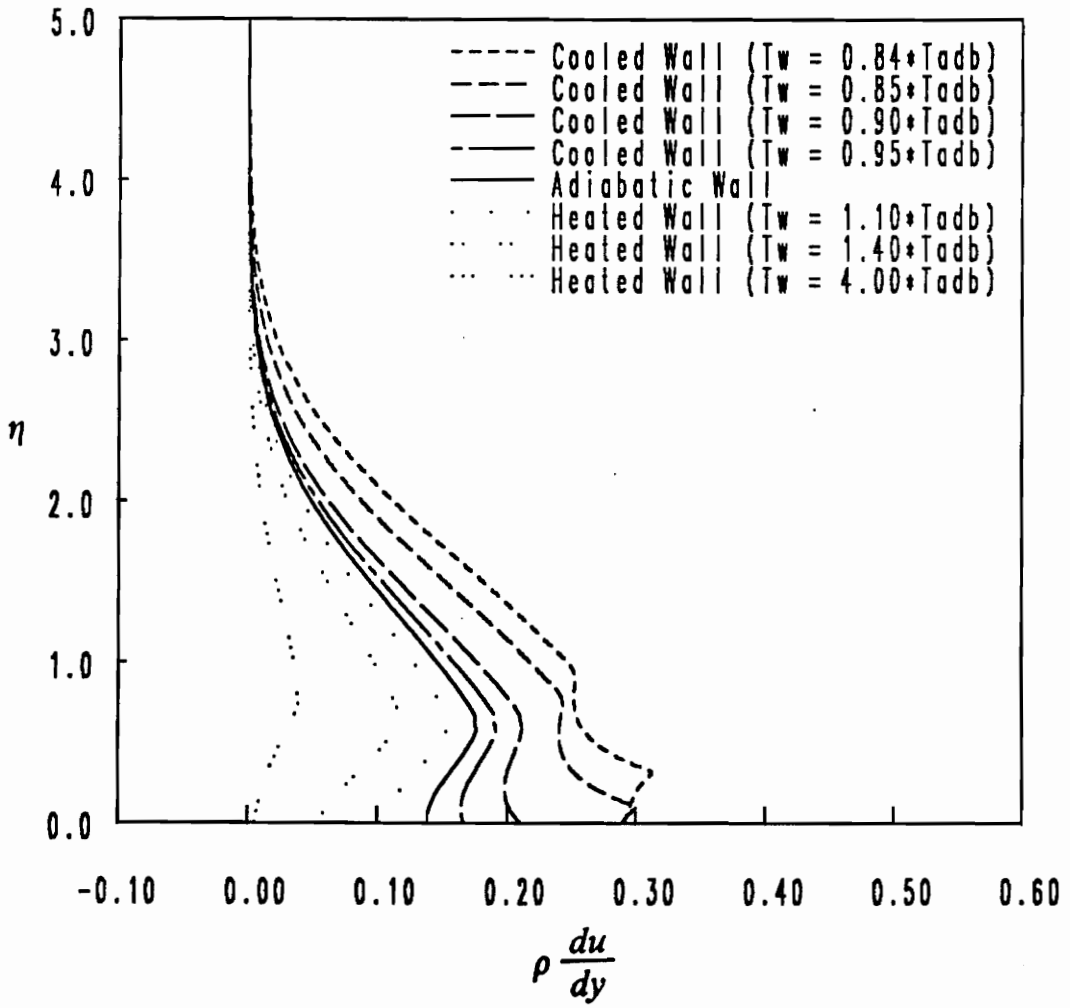

Figure 8.11. Plot of $\rho(du/dy)$ vs. η in a near-critical flow: Illustrated are the results for a freestream Mach number of 2.0 and a freestream temperature of $1.01*T_c$.

Chapter 9

Conclusions and Future Work

The equations and numerics necessary for the analysis of dense-gas boundary-layer flows over arbitrary two-dimensional bodies have been developed. Mean flows over adiabatic, heated, and cooled flat plates were calculated and the stability investigated using an inviscid temporal approach. The mean-flow calculations for an adiabatic wall were performed for nitrogen, sulfur hexafluoride, and toluene. The stability analysis and the calculations for flows over heated and cooled walls were performed for nitrogen only.

The mean-flow results included a number of significant deviations from standard ideal-gas predictions. First, the potential for appreciable variations of the specific heat and the Prandtl number, especially in the vicinity of the thermodynamic critical point, was observed. Second, the skin-friction coefficient was seen to dramatically decrease as the freestream density approached its critical value. As a result, the dense-gas flows are expected to have an increased susceptibility to separation as dense-gas effects become more pronounced. Third, the standard correlations for the skin-friction coefficient, the recovery factor, and the Nusselt number do not accurately predict the corresponding dense-gas parameters.

The effect of increasing specific heat on boundary-layer flows was observed through the substitution of heavier fluids for nitrogen. It was noticed that increased specific heat caused a decrease in the influence of the viscous dissipation and consequently a minimizing of the variation of flow parameters. As a result, flows were seen to approach a quasi-Blasius state. This approach caused an increase in the skin-friction coefficient, meaning that the susceptibility to separation observed in the near-critical and dense-gas nitrogen flows can be partially offset by the substitution of a fluid with a larger specific heat.

An inviscid temporal analysis of the stability characteristics of dense-gas boundary-layer flows revealed significant deviations from standard ideal-gas stability predictions. Among these is a breakdown in the commonly held belief that cooling generally stabilizes boundary-layer flows. In fact, the numerical evidence shown here supports the assertion that cooling may destabilize the boundary layer. In addition, the results indicate the existence of flows for which neither heating nor cooling has a stabilizing effect. Furthermore, the conventional view that the stability may be determined solely by an inspection of the viscosity gradients at the wall has been contradicted. Numerical studies performed here demonstrate that the stability characteristics are determined by a competition between the density and the viscosity, suggesting that the kinematic viscosity is a more reliable indicator of the stability of boundary-layer flows.

Several extensions of the current study are potentially valuable. A growth-rate study is recommended in order to quantify the degree of instability among the cases shown and also to assess the significance of the existence of multiple generalized inflection points as observed in the near-critical flows. Furthermore, the significant discrepancies between the dense-gas and ideal-gas inviscid stability analyses, due in part to the non-classical variation of the viscosity in the mean flow, indicate that an investigation of the viscous stability is warranted. Finally, a study of the effects of varying the specific heat on the stability of dense-gas boundary layers, accomplished by changing the fluid, would be useful.

References

Adamson, T. C., Jr., and Messiter, A. F., "Analysis of Two-Dimensional Interactions Between Shock Waves and Boundary Layers," *Ann. Rev. Fluid Mech.*, 12, 1980, pp. 103-138.

Anderson, W. K., "A Numerical Study on the Use of Sulfur Hexafluoride (SF_6) as a Test Gas for Wind Tunnels," 16th *Aerodynamic Ground Testing Conference*, June 1990.

Anderson, W. K., "Numerical Study of the Aerodynamic Effects of Using Sulfur Hexafluoride as a Test Gas in Wind Tunnels," *NASA TP-3086*, 1991a.

Anderson, W. K., "Numerical Study on Using Sulfur Hexafluoride as a Wind Tunnel Test Gas," *AIAA Journal*, Vol. 29, No. 12, 1991b, pp. 2179-2180.

Blottner, F. G., "Computational Techniques for Boundary Layers," Sandia Laboratories, Albuquerque, N. M., SAND-74-5821, 1974.

Chung, T. H., Lee, L. L., and Starling, K. E., "Applications of Kinetic Gas Theories and Multiparameter Correlation for Prediction of Dilute Gas Viscosity and Thermal Conductivity," *Ind. Eng. Chem. Fund.*, 23, 1984, pp. 8-13.

Chung, T. H., Ajlan, M., Lee, L. L., and Starling, K. E., "Generalized Multiparameter Correlation for Nonpolar and Polar Fluid Transport Properties," *Ind. Eng. Chem. Res.*, 27, 1988, pp.671-679.

Curran, H. M., "Use of Organic Working Fluids in Rankine Engines," *Journal of Energy*, Vol. 5, No. 4, 1981, pp. 218-223.

Delery, J., and Marvin, J. G., "Shock-Wave Boundary Layer Interactions," AGARDograph No. 280, 1986.

Eckert, E., and Drewitz, O., "Der Wärmeübergang an eine mit großer Geschwindigkeit längsangeströmte Platte," *Forschg. Ing.-Wes. 11*, 1940, pp. 116-124.

Emmons, H. W., and Brainerd, J. G., "Temperature Effects in a Laminar Compressible Fluid Boundary Layer Along a Flat Plate," *J. Appl. Mech. 8*, A 105, 1941 and *J. Appl. Mech. 9*, I, 1942.

Hall, W. B., "Heat Transfer near the Critical Point," **Advances in Heat Transfer**, eds. T. F. Irvine and J. P. Hartnett, Academic Press, Vol. 7, 1971.

Fletcher, C. A. J., **Computational Techniques for Fluid Dynamics Volume II**, 2nd ed., Springer-Verlag, New York, 1988.

Hendricks, R. C., Graham, R. W., Hsu, Y. Y., and Medeiros, A. A., "Correlation of Hydrogen Heat Transfer in Boiling and Supercritical Pressure States," *ARS J.*, 32, 1962, pp. 244-252.

Lee, B. I., and Kesler, M. G., "Generalized Thermodynamic Correlation Based On Three-Parameter Corresponding States," *AIChE J.*, Vol. 21, 1975, pp. 510-527.

Lees, L., "Laminar Heat Transfer Over Blunt-Nosed Bodies at Hypersonic Flight Speeds," *Jet Propulsion*, Vol. 26, No. 4, April 1956, pp. 259-269.

Lees, L., and Lin, C. C., "Investigation of the Stability of the Laminar Boundary Layer in a Compressible Fluid," *NACA Tech. Note No. 1115*, 1946.

Mack, L. M., "Boundary-Layer Stability Theory," Jet Propulsion Laboratory, Pasadena, CA, Document No. 900-277, 1969.

Manco, S., and Nervegna, N., "Working Fluid Selection Via Computer Assisted Analysis of ORC Waste Heat Recovery Systems," *Society of Automotive Engineers*, Paper P-85-164, 1985.

Martin, J. J., and Hou, Y. C., "Development of an Equation of State for Gases," *AIChE J.*, Vol. 1, No. 2, 1955, pp. 142-151.

Meksyn, D., "Plate Thermometer," ZAMP 11, 1960, pp. 63-68.

Miller, D. R., "Rankine Cycle Working Fluids for Solar-to-Electrical Energy Conversion," Sandia Laboratories, Albuquerque, N. M., Energy Report SLA-74-0132, 1974.

Owens, E. J., and Thodos, G., "Thermal-Conductivity-Reduced State. Correlation for the Inert Gases," *AIChE J.*, Vol. 3, 1957, pp. 454-461.

Prandtl, L., "Über Flüssigkeitsbewegung bei sehr kleiner Reibung," *Proc. Third Intern. Math. Congress*, Heidelberg, 1904, pp. 484-491.

Reid, R. C., Prausnitz, J. M., and Poling, B. E., **The Properties of Gases & Liquids**, 4th ed., McGraw-Hill, New York, 1987.

Schlichting, H., **Boundary-Layer Theory**, 7th ed., McGraw-Hill, New York, 1979.

Sengers, J. V., "Transport Properties of Fluids Near Critical Points," *National Bureau of Standards Tech. Report 71-074*, Dec. 1970.

Shen, S. F., "Stability of Laminar Flows," **Theory of Laminar Flows**, ed. F. K. Moore, Vol. IV, 1964.

Simoneau, R. J., and Williams, J. C., III, "Laminar Couette Flow with Heat Transfer Near the Thermodynamic Critical Point," *Int. J. Heat Mass Trans.*, Vol. 12, 1969, pp. 120-124.

Tanaka, H., Nishiwaki, N., Hirata, M., and Tsuge, A., "Forced Convection Heat Transfer to Fluid Near Critical Point Flowing in Circular Tube," *Int. J. Heat Mass Trans.*, Vol. 14, 1971, p.739.

Uyehara, O. A., and Watson, K. M., "A Universal Viscosity Correlation," *Nat'l. Pet. News.*, Vol. 36, No. 40, 1944, pp. R714-R722.

Van Wylen, G. J., and Sonntag, R. E., **Fundamentals of Classical Thermodynamics**, 3rd ed., John Wiley & Sons, New York, 1985.

White, F. M., **Viscous Fluid Flow**, McGraw-Hill, New York, 1974.

Vita

Sarah Turner Whitlock was born in Christiansburg, Virginia on March 2, 1967. She earned a Bachelor of Science and a Master of Science in Engineering Mechanics from Virginia Polytechnic Institute and State University in 1990 and 1992. Her future plans include matriculation at Stanford University where she will pursue a Doctor of Philosophy in Mechanical Engineering.